GRAPHENE BASED NANOSTRUCTURED MATERIALS FOR ELECTROCHEMICAL ENERGY STORAGE

by

Rohit Kanungo

A dissertation submitted to the Graduate Faculty of
Auburn University
in partial fulfillment of the
requirements for the Degree of
Doctor of Philosophy

Auburn, Alabama

August 3, 2019

Approved by

Dr. James Radich, Chair, Assistant Professor of Chemical Engineering
Dr. Bryan Beckingham, Co-Chair, Assistant Professor of Chemical Engineering
Dr. Virginia Davis, Alumni Professor of Chemical Engineering
Dr. Xinyu Zhang, Associate Professor of Chemical Engineering
Dr. Majid Beidaghi, Assistant Professor of Materials Engineering

Abstract

The objective of this work is to gain fundamental insights into the reduction of graphene oxide (GO), chemical reduction induced self-assembly of graphene and assembly of novel three-dimensional graphene morphologies. It is motivated by the prospect of achieving better electrochemical performance by circumventing a common issue of "restacking" and design novel-electrode assemblies. The dissertation first provides insights into the photo-reduction of GO to reduced graphene oxide (RGO), which gives way to the photolytic release of hydroxyl radicals. This has several implications in the stability of GO and unveils potential new applications that take advantage of the OH● photolysis products.

Next, relationships between processing conditions, material properties, and electrochemical response for self-assembled RGO electrode assemblies were studied. Electrode assemblies were prepared from GO dispersions, which are well suited to scaling up and economical production methods. L-ascorbic acid-assisted reduction of GO to RGO was utilized to self-assemble RGO sheets into 3D graphene frameworks, which were formed into electrode assemblies and fabricated into electrochemical double-layer capacitors. The aspect ratio of GO sheets and the solution processing conditions were varied to understand their impacts on the electrochemical response of the RGO capacitors. Ultra-large GO (UL-GO) sheets were synthesized using 50 mesh (297 μm) graphite flakes to fabricate graphene frameworks (GF). Their electrochemical performance was tested against GFs fabricated from small graphene oxide

sheets synthesized using 325 mesh (44 μm) graphite flakes. GFs fabricated from UL-GO demonstrated a 25% higher specific capacitance, six times faster ion-transport, and six times lower charge transfer resistance. These results are indicative of higher energy density, efficient ion transport and improved electrical percolation in the 3D matrix of GFs formed by UL-GO.

Next, the effect of concentration and pH for small GO and UL-GO was studied. 3D graphene frameworks were prepared using small GO with the concentrations from 2.0 mg/mL to 12 mg/mL and UL-GO with concentration from 0.5 mg/mL to 4 mg/mL. The superior electrochemical results such as high capacitance and low charge/discharge times were observed for optimum concentrations of 3.5 mg/mL and 1.5 mg/mL with a pH of 10 for GFs formed by small GO and UL-GO, respectively.

Modifying GO morphology can result in interesting properties of 3D graphene frameworks. Therefore, a novel solution-based technique was developed to produce holey graphene. It was demonstrated that hydroxyl radicals are formed by microwave irradiation of H_2O_2, which can facilitate the bulk synthesis of holey graphene. Hydroxyl radicals produced from H_2O_2 attack both defective sites and sp^2 hybridized carbon within RGO. Oxidative chemical etching removes RGO-carbons to locally produce holes.

The achievement of superior electrochemical properties in 3D graphene frameworks by varying the sheet size and processing condition suggests that there are many opportunities where a fundamental understanding of assembling nanomaterials as basic building blocks can lead to desirable properties of bulk 3D materials. The work presented here could enable further improvements based on the availability of high specific surface area and more diffusion pathways in the graphene-based electrode assemblies.

Acknowledgments

My PhD journey would not have been possible without immense support and patience from my beloved wife Aakanksha, who consistently made three hours trips every other weekend from Mobile to Auburn. She has always inspired and challenged me to be the best version of myself. I would like to thank my parents who kept sending their love in the form of Indian sweets, so that I do not feel homesick.

I give special thanks to my advisor Dr. James Radich for always motivating me. He has groomed me into an independent thinker by always allowing me to follow my ideas. I have and always will take inspiration from his life.

I thank Dr. Virginia Davis, Dr. Xinyu Zhang and Dr. Majid Beidaghi for being on my committee. I was fortunate to enroll in courses they offered during my graduate school. Their knowledge gave me a broader perspective and made me a better researcher. I am grateful to Dr. Bryan Beckingham, co-chair of my PhD committee who helped me a lot with his guidance and support.

I thank my undergraduate mentees Caleb Ryan and Michael Hooks for helping me conduct numerous experiments. I thank my lab mates Animesh Mondal, Rong Zhao and Fatima Hamade for their friendships. The research and philosophical discussions in the lab were among the best conversations I had in graduate school. I also thank Dr. Michael Miller for allowing me to use Auburn University Research Instrumentation Facility for material characterization and agreeing to be the University Reader for my dissertation.

Table of Contents

List of Tables

List of Figures

List of Abbreviations

3DGF	3-Dimensional Graphene Framework
AC	Activated Carbon
AuNP	Gold Nanoparticle
BET	Brunauer–Emmett–Teller
CNF	Carbon Nanofiber
CNT	Carbon Nanotube
CV	Cyclic Voltammetry
CVD	Chemical Vapor Deposition
DI	Deionized
DMA	Dynamic Mechanical Analysis
DOE	Department of Energy
EC	Electrochemical Capacitor
EDLC	Electric Double Layer Capacitor
EIS	Electrochemical Impedance Spectroscopy
ESR	Equivalent Series Resistance
FTIR	Fourier Transform Infrared
GO	Graphene Oxide
GF	Graphene Framework

HGF	Holey Graphene Framework
LGF	Large Graphene Framework
MB	Methylene Blue
MO	Metal Oxide
MW	Microwave
NBB	Naphthol Blue Black
ORGO	Oxidized Reduced Graphene Oxide
RC	Resistor Capacitor
RGO	Reduced Graphene Oxide
SEM	Scanning Electron Microscope
sMEGO	Microwave Expanded Graphene Oxide Sphere
SSA	Specific Surface Area
TA	Terephthalic Acid
TAOH	2-Hydroxy Terephthalic Acid
TEM	Transmission Electrode Microscope
UL-GO	Ultra Large Graphene Oxide
XPS	X-ray Photoelectron Spectroscopy

Chapter 1

Graphene to Electrochemical Capacitors

1.1 The Graphene Solution

1.1.1 Single-Layer Graphene

Graphene has the potential to solve many technological challenges in areas such as energy storage/production and flexible electronics owing to its high surface area, high electronic mobility, exceptional mechanical strength, and chemical stability. Graphene is a 2D material where carbon atoms are arranged in a hexagonal manner forming a conjugated sp^2 network of carbon-carbon bonding. It is also the basic building block of graphite, which is a stack of thousands of individual graphene sheets bound together by van der Waals attraction.

Graphene was first isolated from graphite by Geim and Novosolov, which resulted in them being awarded the 2010 Nobel Prize in Physics. Since then graphene has been highly studied allotrope of carbon. It has a large theoretical surface area of 2630 m^2/g and intrinsic electron mobility of 200,000 $cm^2/V/s$.[1-4] The 2D structure of graphene and low atomic weight of carbon gives it such a high surface area. The exceptional electronic mobility is due to the conjugated sp^2 network that gives rise to a conducting π band of $2p_z$ electrons, oriented perpendicular to the bonding plane.[5]

Single-layer graphene also known as pristine graphene can be prepared in a number of ways. It was first isolated from graphite using Scotch tape, which is not a suitable method of production for commercial applications. Over the years, scientists have developed methods such as chemical vapor deposition, surfactant-assisted exfoliation, thermal decomposition of SiC, and surfactant- and solvent-mediated sonolysis.[6-9] Chemical vapor deposition is one of the most common techniques for preparing single layer-graphene sheets. However, all these methods

require expensive infrastructure due to the extreme processing conditions and utilization of very strong acids and toxic chemicals.

1.1.2 Graphene Oxide and Reduced Graphene Oxide

Bulk production of pristine graphene through a cheap, safe and non-toxic process does not exist and poses a challenge for the applications of graphene to commercialize. However, reduced graphene oxide (RGO) can be produced in bulk and has a structure similar to graphene (with defects and oxygen functional groups on the basal plane). Graphene oxide (GO), the precursor of RGO is synthesized by a solution-based method in which graphite is oxidized and exfoliated to form single to few-layer GO sheets as shown in Figure 1.1 by a process known as Hummer's method.[10]

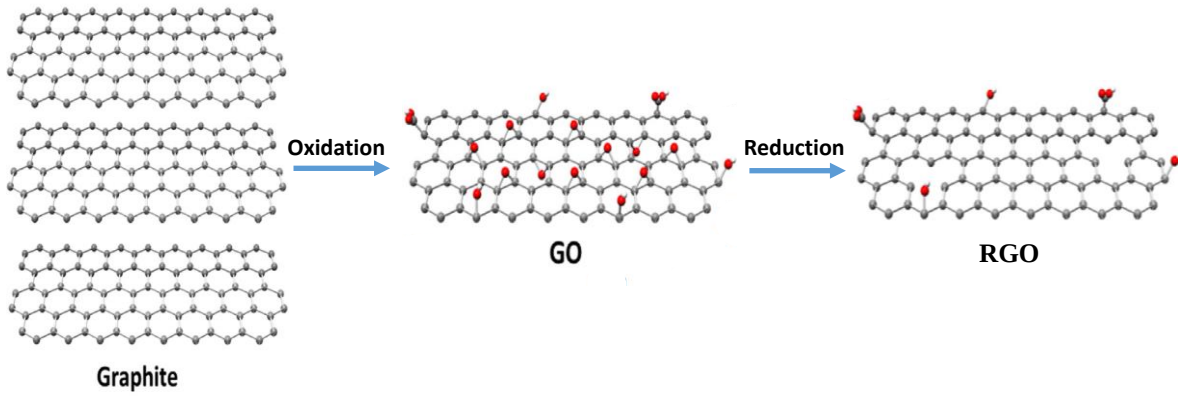

Figure 1.1: A schematic showing graphite oxidized to graphene oxide using Hummer's method and then reduced to reduced graphene oxide. Carbon atoms displayed as gray spheres, oxygen as red and hydrogen as white.

Due to the oxygen functional groups on GO, most of the carbon in the basal plane of GO is sp^3 hybridized, i.e. electrons are not delocalized but involved in forming covalent bonds with oxygen functional groups and hence GO is a poor conductor of electricity. The reduction of GO to reduced graphene oxide (RGO) leads to a partially restored sp^2 network and therefore the partial restoration of electrical conductivity.[5] Reduction can be achieved via various methods - thermal, chemical, electrochemical, and photochemical processes.[11-18] High-

resolution transmission electron microscope (TEM) images of graphene, GO, and RGO, shown in Figure 1.2, reveals the differences in their structure.[19] All carbon atoms in pristine graphene are sp^2-hybridized, also referred to graphitic carbon is represented in green color. In GO, most of the carbon atoms are oxidized (sp^3-hybridized) and are represented in red color. In RGO, a majority graphitic region is recovered with few oxidized carbon and holes. RGO is the closest structure to pristine graphene that can be achieved via solution-based methods.

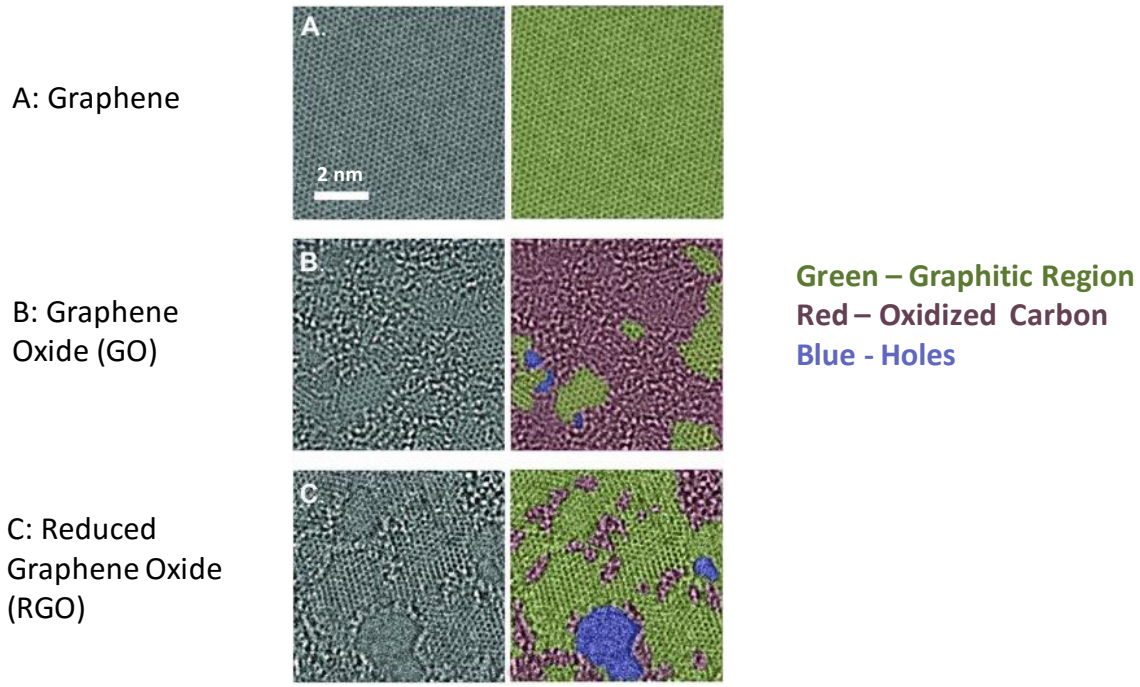

Figure 1.2: Aberration corrected TEM images of (A) single suspended sheet of graphene, (B) single suspended sheet of GO and (C) suspended monolayer of RGO.[19]

The Lerf-Klinowski Model, as shown in Figure 1.3 is a widely accepted structural model of GO sheets.[20] It suggests that the basal plane of GO contain hydroxyl and epoxy functional groups while carboxylic acid groups are on the edges and defects. The carboxylic groups ionize in a polar solvent such as water. This gives the GO sheets a net negative charge and repulsive forces among sheets keep them separated to form a stable dispersion.[21] The stability of GO

dispersion unveils a host of opportunities to perform solution-based chemistry using this material.

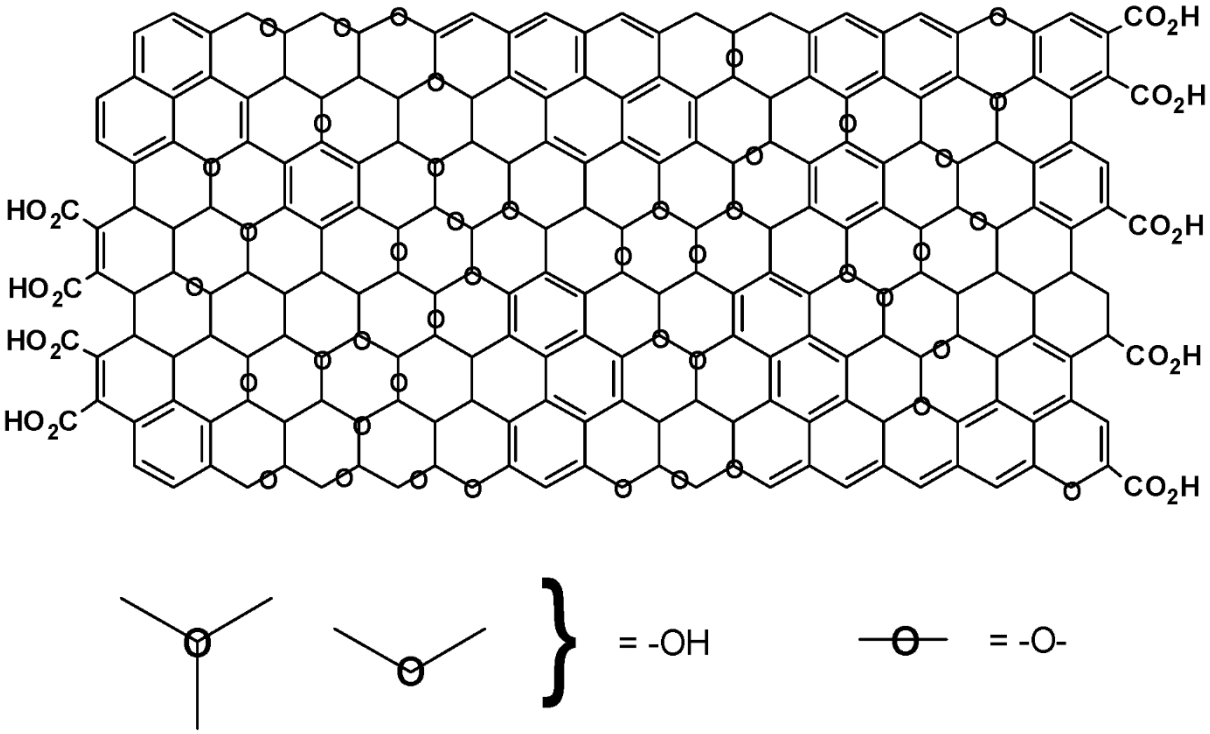

Figure 1.3: Lerf-Klinowski Model for the structure of GO.[21]

1.1.3 The Restacking Problem

In a reduction process, the oxygen functional groups mainly hydroxyl and epoxy are removed from the basal plane of graphene oxide sheets. This can be done by various methods mentioned in the previous section. The criteria for the selection of the reduction method is based on the following aspects: reduction degree and dispersibility. A higher degree of reduction will lead to higher conductivity. A good dispersibility of RGO sheets in a solvent will lead to a stable dispersion and better control over the final product.

Among various solution-based methods, reduction via L-ascorbic acid in basic pH range is known to be the best method.[22] The RGO made from this method shows the highest conductivity and remain stable in a dispersion if a basic pH is maintained. Another reason L-

ascorbic acid is widely accepted reducing agent for GO is because of its significantly lower toxicity as compared to other reducing agents such as hydrazine.

In recent years, RGO has become a popular material to study for energy storage applications especially electrochemical capacitors (ECs).[4, 23-27] However, the recovered sp^2 carbons on RGO sheets have a hydrophobic nature and attract similar sheets because of van der Waals forces and hydrophobic interactions. If reduction reaction is not controlled individual sheets coalesce together to form restacked graphene. This decreases the specific surface area (SSA), porosity and conductivity leading to a deteriorated performance of devices fabricated from RGO.[28-32] Therefore, considerable focus has been placed in developing unique morphologies from RGO. These include constructing 3D architectures, making mesoporous graphene, etc. These unique morphologies take advantage of high mechanical strength, electrical conductivity, and flexibility of graphene to deliver better performance while avoiding the problem of restacking.

Self-assembly is a relatively unexplored method of synthesizing 3D graphene frameworks that is achieved by controlled chemical reduction of graphene oxide (GO). GO sheets in an aqueous dispersion remain separated due to the dominance of repulsive forces among negatively charged ionized carboxylic groups at the edges of the GO sheets.[21] These repulsive forces can be neutralized by the controlled removal of hydroxyl and epoxy functional groups from the basal plane of GO sheets. This results in the coalescence of RGO sheets due to van der Waals attraction which leads to the formation of an interconnected network of 2D sheets possessing solid-like properties. The key issue with such architectures is the lack of fundamental understanding of the reduction process and the structure-processing-property relationships. Hence, the focus of this research is to understand the reduction of GO and

structure-processing-property relationships of self-assembled 3D graphene frameworks by investigating electrochemical properties.

1.2 Energy Storage

There is an urgent need to develop innovative energy storage systems to reduce the overall costs of producing and supplying electricity and to reduce carbon emissions. Currently, the energy infrastructure is set-up in a way that production of electricity is constantly ramped up or down based on the demand. To ensure uninterrupted supply of electricity, power plants keep a vast array of expensive equipment on standby. This results in the variation in cost of electricity throughout the day; lower rates are available during off-peak hours and higher rates are charged during peak hours of electricity usage. An efficient way of producing and distributing electricity would be to run power plants at a constant rate and store surplus energy that can be supplied during peak hours. Currently, the infrastructure for electrical energy storage is limited in the U.S. resulting in major financial and energy losses.

Today, 83% of electricity in the U.S. is generated from burning non-renewable sources such as natural gas, coal, and petroleum.[33] Due to ever-increasing energy demand and concerns about air pollution, renewable energy sources such as wind and solar energy are growing as shown in Figure 1.4. However, the intermittent availability of sunlight and wind poses a challenge to meet the fluctuating energy demand. If renewables are to become primary sources of energy in the future, the need of storing energy cannot be ignored.

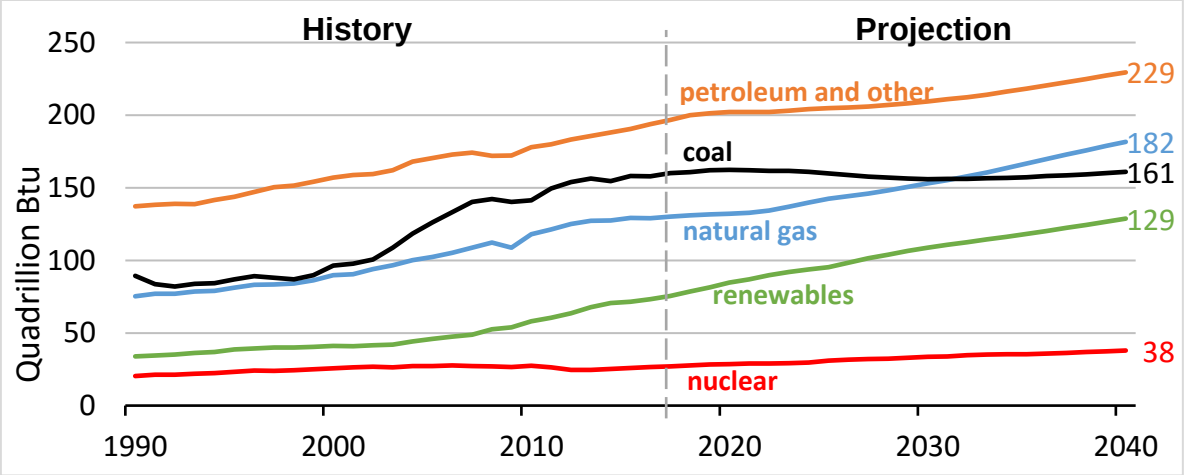

Figure 1.4: World energy consumption by energy source.[34]

Development of advanced energy storage systems will play a crucial role as society's energy needs evolve. These energy storage systems should have high energy and power density, low cost, good safety, the capability of fast charging/discharging and operable in large temperature windows. Batteries and electrochemical capacitors (ECs) are the two most widely used energy storage devices. Batteries have a high-energy density but low power density, unlike ECs that have low energy density but high-power density. Figure 1.5 shows the Ragone Plot[34], which is a plot of energy density versus power density of energy storage systems.[26]

Lithium-ion batteries, that power our phones and laptops, are the current market leader because of their ability to store a large amount of energy per unit mass. These energy storage systems have two major drawbacks – high production costs and high risk of the fire hazard. Overcoming these issues will result in lower electricity bills, explosion-proof phone batteries, and accessible electric-based transportation. A concerted effort from scientific and business communities are being focused to produce safe and cost-effective energy storage devices. It is important to note that research in batteries is significantly more matured as compared to ECs, which have gained more attention recently.

The energy storage systems of the future are most likely to be a combination of batteries and ECs. ECs are made of inexpensive carbon-based materials, have a long life and no fire hazard. However, they have very low energy density and hence a lot of effort is required to improve the energy density of ECs. The work presented here describes the synthesis of graphene-based nanostructured materials which have a large surface area and promote improved ion diffusion. Further, the structure-processing-property relationships of graphene nanostructures are developed by investigating fundamental electrochemical properties. The insights acquired from this work can be applied to other applications such as Li-ion batteries, fuel cells, and hydrogen storage.

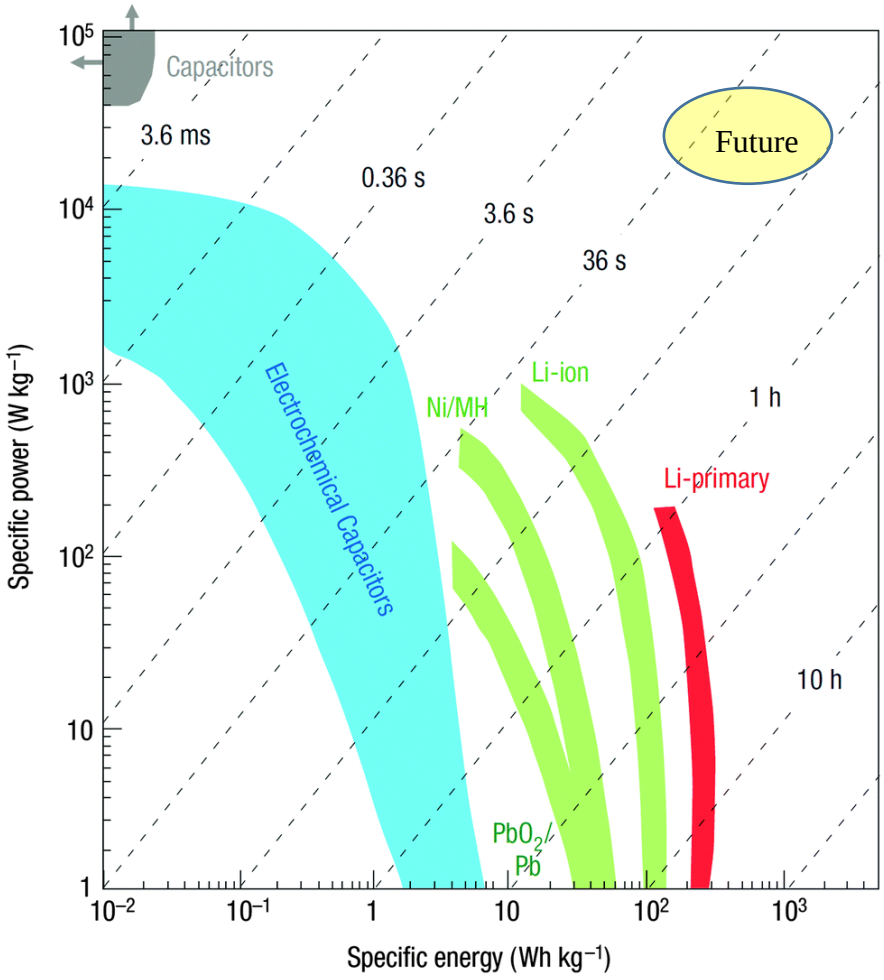

Figure 1.5: Ragone plot for important energy storage systems.[26]

1.3 Electrochemical Capacitors

Electrochemical Capacitors can be categorized into two types, electric double-layer capacitors (EDLCs) and pseudocapacitors. EDLCs store and release energy by electrostatic charge accumulation at the electrochemical interface between and electrode and electrolyte.[35] This is achieved by adsorption of anions and cations of electrolyte at the electrode/electrolyte surface as shown in Figure 1.6 (A). Pseudocapacitors store energy electrochemically by intercalation of electrolyte ions in the electrode and then by undergoing electron transfer reaction (Faradaic reaction) that occurs at the surface of the electrode as shown in Figure 1.6 (B). As compared to batteries, ECs have many essential characteristics, such as fast charging/discharging, large number of charge-discharge cycles, and wide operating temperatures.[36] Because of these characteristics, ECs can recover energy from many repetitive processes. For example, ECs find applications in electric vehicles, hybrid vehicles, elevators, cranes and forklifts.[36, 37] Large-scale ECs can regulate the power supplied by the electrical grid, which can avoid the costly shutdown of industrial operations because of intermittent outages and power fluctuations. Further, with the advancements of renewable energy like solar and wind, there will be a huge demand for complex energy storage systems that will necessitate the development of advanced ECs.

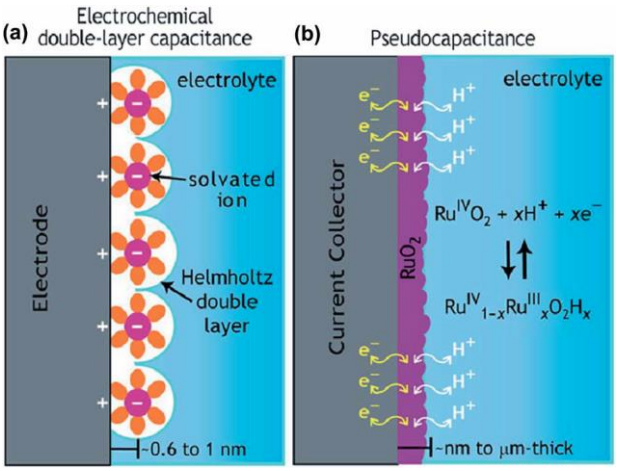

Figure 1.6: Schematic of two different charge storage mechanisms via (A) electrochemical double-layer capacitance (EDLC) and (B) redox reaction based pseudocapacitance.[38]

Critical parameters that gauge the performance of an EC are energy density, power density and charging/discharging time. These parameters can be correlated to the experimentally measured quantities such as capacitance, equivalent series resistance (ESR), and time constant of the RC (Resistor-Capacitor) circuit modeled for the EC system (τ_o). Energy density and charging/discharging times are proportional to capacitance and τ_o, respectively while power density is inversely proportional to ESR. Capacitance, ESR and τ_o are measured by electrochemical techniques such as cyclic voltammetry (CV) and electrochemical impedance spectroscopy (EIS) discussed in Chapter 3 in detail. Energy (E) and power (P) of an EC are calculated according to the following equations:

$$E = \frac{1}{2}CV^2 = \frac{1}{2}QV$$

$$P = \frac{V^2}{4R}$$

where C is the capacitance, V is the operating voltage window and Q is the charge stored on the electrode-electrolyte interface or charged transfer during redox reactions in case of pseudocapacitor, R is the equivalent series resistance (ESR). ESR is dependent on many factors

such as conductivity of the electrolyte, electrode material, and current collectors, charge transfer resistance, and the double-layer capacitance.[39]

1.3.1 Electric Double Layer Capacitance

Carbon-based materials such as activated carbons (ACs) exhibit the EDLC behavior where capacitance that arises from charge separation at the electrode-electrolyte interface can be described by the equation below:

$$C = \frac{\varepsilon_r \varepsilon_0 A}{d}$$

where ε_r is the relative permittivity of electrolyte, ε_0 is the permittivity of the vacuum, d is the effective thickness of the double layer, and A is the electrode surface area. The double-layer capacitance is between 10 - 50 μF/cm depending on the electrolyte used.[27] High specific surface area (SSA) is, therefore, a primary requirement for electrode material. Specific capacitance achieved with aqueous electrolyte is higher than organic electrolytes,[40] but organic electrolytes can sustain a higher operational voltage window (2.7 V as compared to 1 V in aqueous). As the energy and power of an EC vary with the square of voltage resulting in higher energy and power, organic electrolytes are widely used in the commercial ECs. Although there is a great need of innovation in developing both novel electrolytes as well as electrode materials, this research presented here focuses on the development of new nanostructured electrode materials. Another important aspect for electrode material is the efficient ion transport inside the bulk material, which improves the power delivery of an EC. Efficient ion transport can be achieved by constructing optimized pore structures. However, due to the lack of fundamental understanding of GO reduction and self-assembly of graphene, achieving a 3D architecture with high SSA and optimized pore structure for efficient ion diffusion is challenging.

1.3.2 Pseudocapacitance

Metal oxides (MOs) such as RuO_2, MnO_2, NiO, Fe_3O_4, and conductive polymers exhibit pseudocapacitive behavior via fast reversible redox reactions at the surface of electrode material.[26] The energy stored in pseudocapacitor is dependent on the number of molecules of active material undergoing reversible electron transfer. Therefore, a large specific surface area accessible to the electrolyte is also the primary requirement for pseudocapacitive materials. Pseudocapacitors have 3-4 times higher capacitance as compared to EDLC. However, they have a few drawbacks – (1) Charge storage takes place in the first few nanometers from the surface because of poor electron and proton transport in the bulk material, (2) materials tend to deteriorate over time because of rapid expansion and contraction during the redox reaction and (3) MOs have poor electronic conductivity.[26, 41] Hence, a lot of research is focused on making hybrid electrode materials with metal oxides nanoparticles on carbon-based frameworks to enhance the surface area, strength, and conductivity of the electrode.

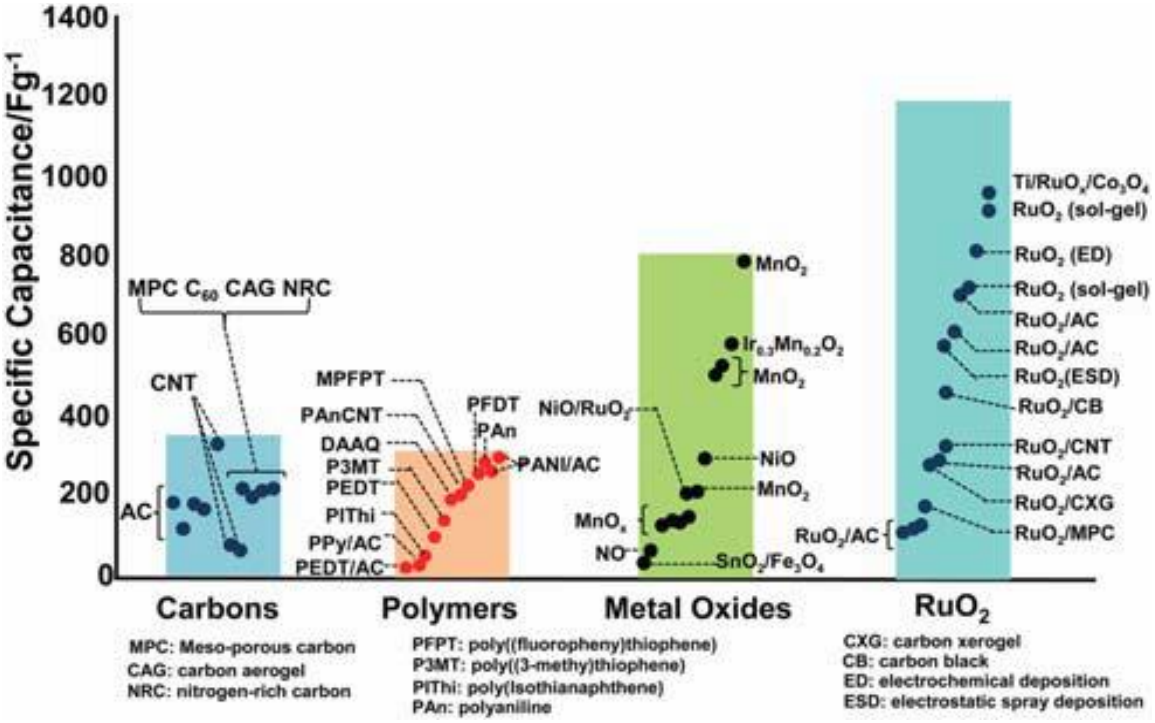

Figure 1.7: Various materials utilized for EC available in literature.[41]

1.3.3 Current Trends and Challenges

Today, state of the art commercially available ECs have activated carbon (AC) as an active electrode material. The high SSA and low cost make AC a very attractive material.[41, 42] However, it has an un-optimized pore structure which restricts the diffusion of electrolyte ion inside pores and results in insufficient utilization of surface area. This is the reason why ECs have very low energy density. A report by US Department of Energy (DOE) stresses upon the need to study the energy storage phenomena at atomic scale so that electrodes and electrolytes can be tailored with targeted properties.[36] DOE defines four broad areas of focus required for building exceptional energy storage devices:

1. Advances in Characterization
2. Nanostructured Materials
3. Innovations in Electrolytes
4. Theory, Modeling, and Simulation

Tremendous research efforts are being focused to improve the energy density of ECs by investigating pseudocapacitive materials like conducting polymers, metal oxides (MOs) and porous carbon materials with high SSA.[41] Some of the popular materials that are being investigated are shown in Figure 1.7. There are excellent review articles published recently on various electrode materials for EC.[26, 27, 41, 43] MO-based electrodes have demonstrated specific capacitance (which is directly proportional to specific energy) as high as 1300 F/g (for RuO_2) because of their pseudo-capacitive behavior.[27] However, the expensive cost of RuO_2 makes the commercialization very difficult. Although materials like MnO_2 and $Ni(OH)_2$ are cheap, they suffer capacity loss after long cycles. The intercalation/de-intercalation of ions over a period causes wear and tear in the electrode material. Similar issues are a concern in the conductive polymers based electrodes.[24] Although gravimetric capacitance is considered as a primary

metric to evaluate the performance of EC, the volumetric capacitance has recently become an important metric owing to the widespread use of portable devices and the advent of electric cars. High gravimetric capacitance requires a highly porous microstructure while high volumetric capacitance requires a high packing density of electrode material. Hence, there is a trade-off relationship between gravimetric and volumetric capacitances. Therefore, there is a requirement of innovative methods to synthesize electrode materials for EC that could boost gravimetric and volumetric capacitances simultaneously.

Researchers have recognized that to utilize graphene-based nanomaterials for energy storage applications, it is essential to understand the GO chemistry, morphology, reduction of GO and assembling behaviors of 2D graphene sheets into 3D frameworks. Due to this last decade has seen significant growth in graphene research. The remainder of this chapter is a literature survey of selected publications for understanding the research presented in this dissertation.

1.4 Literature Review

1.4.1 Holey Graphene

Graphene sheets with optimum size and distribution of holes can prevent the sheets from restacking. This is due to the presence of carboxylic groups at the edges of the holes which cause steric hindrance. Recently, Kim et al. demonstrated the fabrication of three-dimensional porous graphene with hierarchical pore structure using KOH activation.[44] The GO was crumpled into ball-like particles by aerosol spray drying. These GO particles were then treated in a microwave oven to yield exfoliated RGO powder composed of hollow spheres. This powder, named sMEGO, was then washed in KOH solution, followed by filtration and drying. The sMEGO/KOH mixture was put in a tube furnace under flowing argon at a pressure of about 1 atm and heated at 800 °C for 1 hour. A schematic of this process is shown in Figure 1.8.

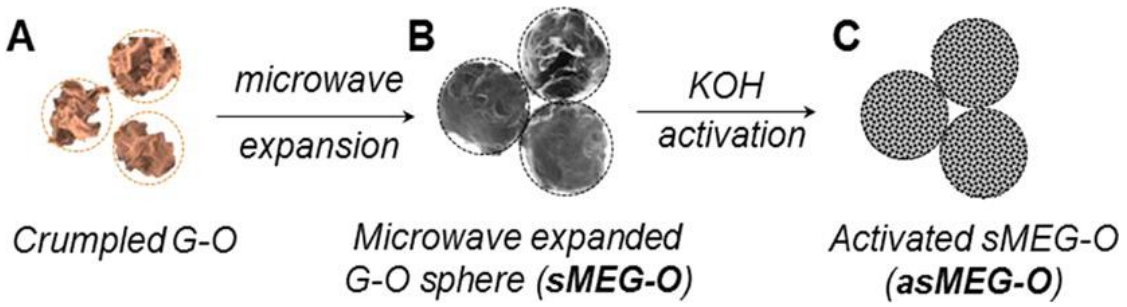

Figure 1.8: Schematic of fabrication of highly porous graphene-derived carbons with hierarchical pore structures: (A) GO sheets are transformed into crumpled ball-like GO particles by aerosol spray drying technique, (B) under microwave irradiation, crumpled GO particles form hollow graphene passed spheres, and (C) chemical activation with KOH.[44]

KOH activation yields a continuous 3D network of pores, ranging from 1 nm to 10 nm and a BET surface area of 3290 m^2/g. The electrodes fabricated with these carbons demonstrate a specific capacitance of 174 F/g at a current density of 2 A/g in an organic electrolyte. This hierarchical porous graphene structure was achieved due to the utilization of crumpled GO sheet and the instant microwave heating which exfoliated the RGO sheets.

Thermal exfoliation of graphene oxide to create porous graphene has been reported multiple times.[45-48] Holey graphene nanosheets prepared by heating powdered GO to 300 °C in presence of air at different temperature ramping rates is shown in Figure 1.9.[47] During the heating process, the carbon atoms at weak defect spots of GO are etched away by converting into CO_2 gas. The pressure buildup due to the released gas not only exfoliate the layers but also punch holes on graphene. The hole size ranges from 10 nm to 250 nm and the EC made of holey graphene exhibits a capacitance of 185 F/g for a current density of 2 A/g in 6 M KOH electrolyte.

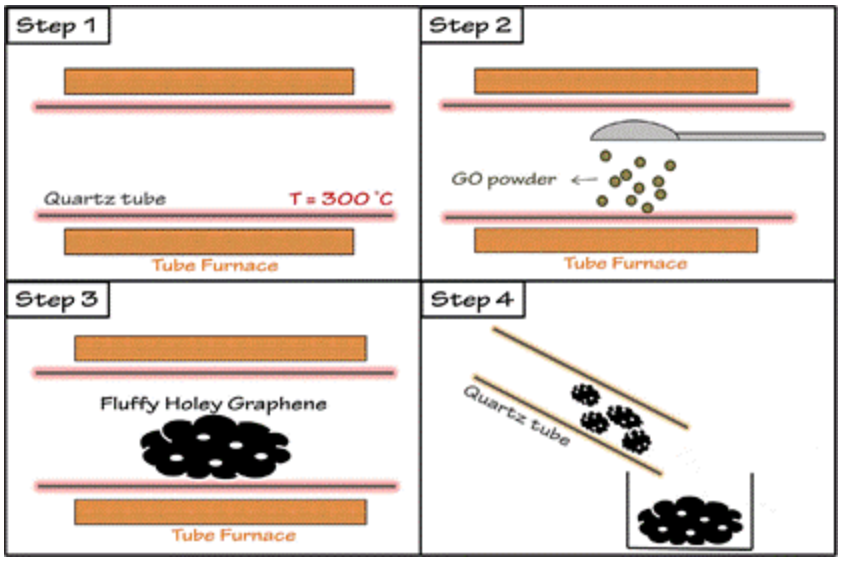

Figure 1.9: Schematic illustration for the ultra-rapid heating of GO powder to obtain and collect fluffy holey graphene nanosheets.[47]

Radich et al. in 2014 prepared holey graphene using UV photolysis of H_2O_2 to attack RGO with hydroxyl radicals (OH●) in presence of gold nanoparticles (AuNP).[5] This work demonstrated that AuNP catalyzed the UV photolysis of H_2O_2, mediated the OH● attack on RGO and prevented stacking of RGO sheets. For this study, GO was prepared by modified Hummer's method. GO was reduced photochemically by shining light on the sample. The RGO produced was mixed with AuNP and controlled amount of H_2O_2. This mixture was irradiated with white light that initiated the reaction to produce holey graphene as shown in Figure 1.10. Hydroxyl radicals, produce via photolysis of H_2O_2, initially attacks RGO to produces an OH adduct or undergoes electron transfer to produce cation radicals. Continued attack of hydroxyl radicals causes complete oxidation of the organic compounds to CO_2 and water, which creates nanopores. This oxidized RGO (ORGO) is the final product also referred as holey graphene.

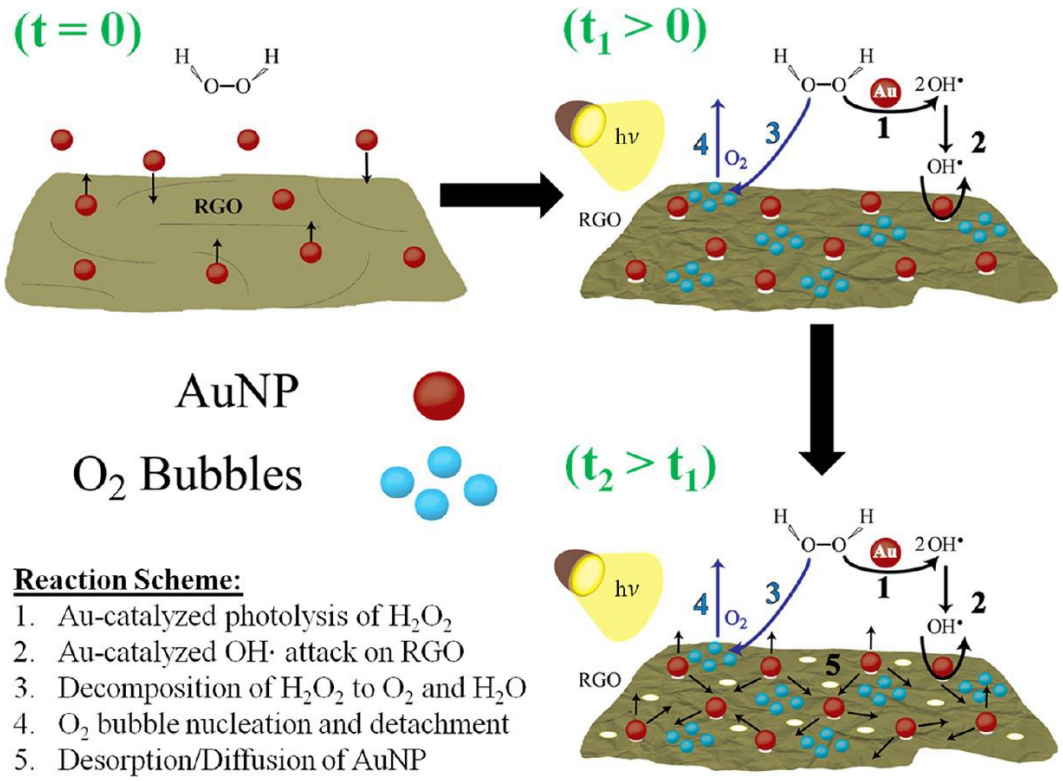

Figure 1.10: Proposed mechanism for photoinduced reaction between RGO, AuNPs and H_2O_2.[5]

The high-resolution TEM images shown in Figure 1.11 (D) demonstrate the presence of holes of size ranging from 5-100 nm. Radich et al. suggested that wrinkles are observed on the RGO sheets because O_2 bubble nucleation on the RGO surface during oxidation. The effects of the OH● radical reaction was studied by performing Fourier-transform infrared (FTIR) spectroscopy on the samples. The FTIR spectra shown in Figure 1.12 indicates C=C attack by OH● results in higher absorption in the regions of C=O and -OH modes and lower absorption in the regions of C=C–H and C–O modes. Clearly, ORGO shows a reduced absorption for hydroxyl, epoxy and carbonyl groups. This consolidates the fact that defective carbon sites were oxidized and etched away by OH●.

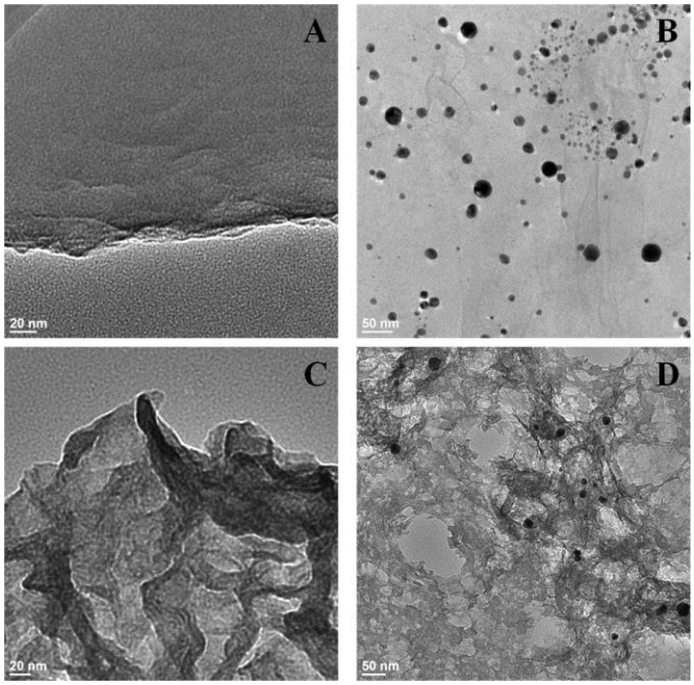

Figure 1.11: TEM images of samples irradiated for 2 hours (A) RGO, (B) Au+RGO, (C) H_2O_2+RGO and (D) Au+H_2O_2+RGO.[5]

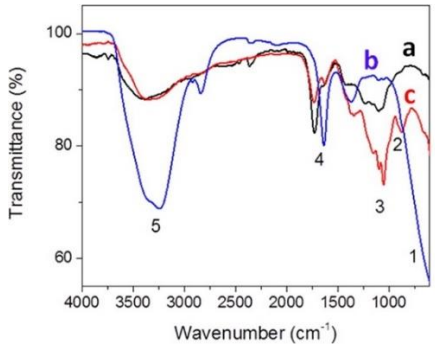

	cm^{-1}	Characteristic
1	500-900	-OH
2	800-1000	C=C-H
3	1000-1250	C-O
4	1700-1750	C=O
5	3000-3700	-OH

Figure 1.12: FTIR spectra of (a) 2 h irradiated AuNP–H2O2–RGO, (b) 2 hours irradiated H_2O_2–RGO, and (c) pre-irradiated RGO.[5]

Synthesis of holey graphene has been reported by many other groups as well. Zhao et al. manufactured flexible holey graphene paper electrodes sonicating GO solution with nitric acid to make pores and further thermally reducing it.[49] Fan et al. synthesized porous graphene sheets by mixing GO with $KMnO_4$ and irradiating with microwaves.[50] The resultant holey GO was reduced by hydrazine solution and then acid washed to remove MnO_2. Jhajharia et al. prepared holey graphene using a soft template method.[51] In alkaline conditions,

cetyltrimethylammonium bromide – GO interaction is favored and a stable colloid is formed. This colloid is treated with tetraethyl orthosilicate to functionalize GO with inorganic silicate. These Si functionalized GO sheets are mixed with 1 M NaOH and washed with warm ethanol to get holey graphene. Apart from solution-based methods, researchers have manufactured interesting graphene morphologies from lithographic techniques.[52-55]

Each of the research studies discussed above is a step forward in the quest to make exceptional electrode materials for energy storage. However, there are many areas where improvement in the synthesis techniques are required along with a better understanding of graphene morphologies effect on their electrochemical properties. Some of the methods described above utilize harmful acids or use high temperature and high-pressure processes which are unsafe and in turn become expensive methods. Lithographic methods have a very low yield and are extremely expensive because of their infrastructure requirement. Methods like gold mediated holey graphene production[5] has a very low yield and is a very slow process. Hence, there is an essential need to develop simple synthesis routes for holey graphene production that are inexpensive, environmentally benign and scalable methods.

1.4.2 Three-Dimensional Graphene Frameworks

Xu et al., prepared a 3D network of holey graphene frameworks (HGFs) with hierarchical porous structure through a simple one step process as shown in Figure 1.13 (A).[56] Hydrogen peroxide was mixed with a dispersed solution of GO. The mixture was heated at 180 °C for 6 hours in a hydrothermal reactor. During the reaction, GO sheets were reduced creating freestanding porous holey graphene. Hydrogen peroxide helps in partially oxidizing carbon atoms around active defective sites and form nanopores in the GO sheets. These nanopores are distributed throughout the GO sheets because of the abundant presence of defective carbon sites. The degree of etching can be controlled by the amount of H_2O_2.

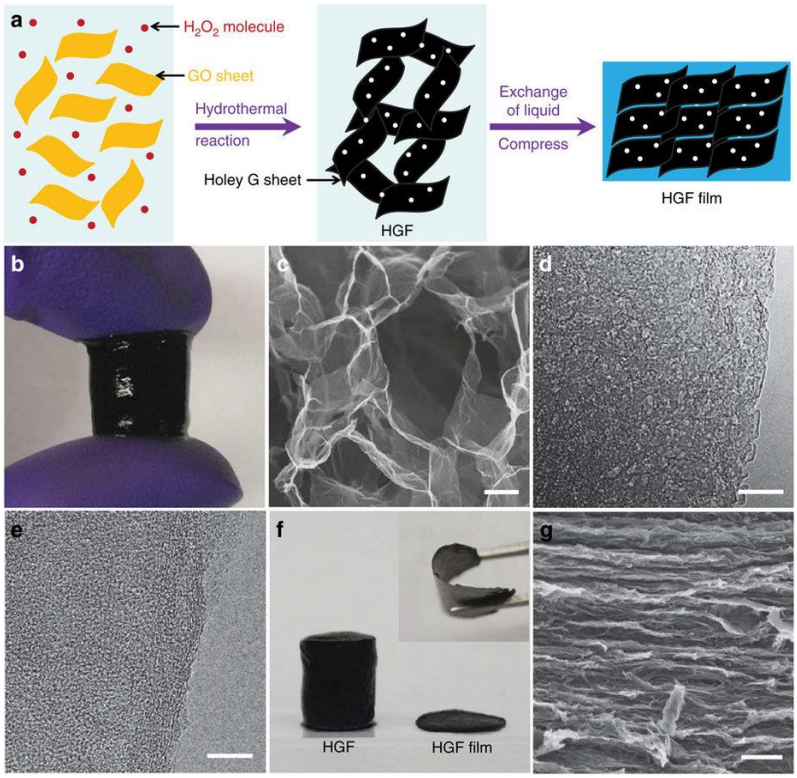

Figure 1.13: (A) Schematic illustration of the preparation process of HGFs. (B) photograph showing a free-standing HGF. (C) SEM image of interior microstructures of HGFs. Scale bar, 1 mm. TEM image of (D) holey graphene sheets in HGFs. Scale bar, 10 nm. (E) non-holey graphene sheets in GFs for comparison. Scale bar, 10 nm. (F) Digital image showing HGFs before and after mechanical compression with the flexibility of the compressed HGF film shown in the inset. (G) Cross-sectional SEM image of the compressed HGF film. Scale bar, 1 mm.[56]

The specific surface area of the HGF estimated from Brunauer–Emmett–Teller (BET) measurement was 1560 m^2/g. This holey graphene framework is actually a 3D structure with a hierarchical porous network. This material has a high packing density and efficient electron transfer. Due to these properties, they were able to achieve a gravimetric capacitance of 298 F/g and a volumetric capacitance of 212 F/cm in organic electrolyte.

Sheng et al. demonstrated a self-assembly reaction that does not require high temperature and high pressure.[57] This was done using sodium ascorbate as a reducing agent in the GO aqueous dispersion. A hydrogel is formed, and the resulting 3D network structure is

shown via optical image and a SEM image in Figure 1.14. This chemical reduction process can be completed heating the mixture of GO and sodium ascorbate at 90 °C for 1.5 hours. Moreover, this reaction requires less energy as compared to hydrothermal reduction process. The electrode made by the above-mentioned electrode achieved a high specific capacitance of 240 F/g in 1 M H_2SO_4.

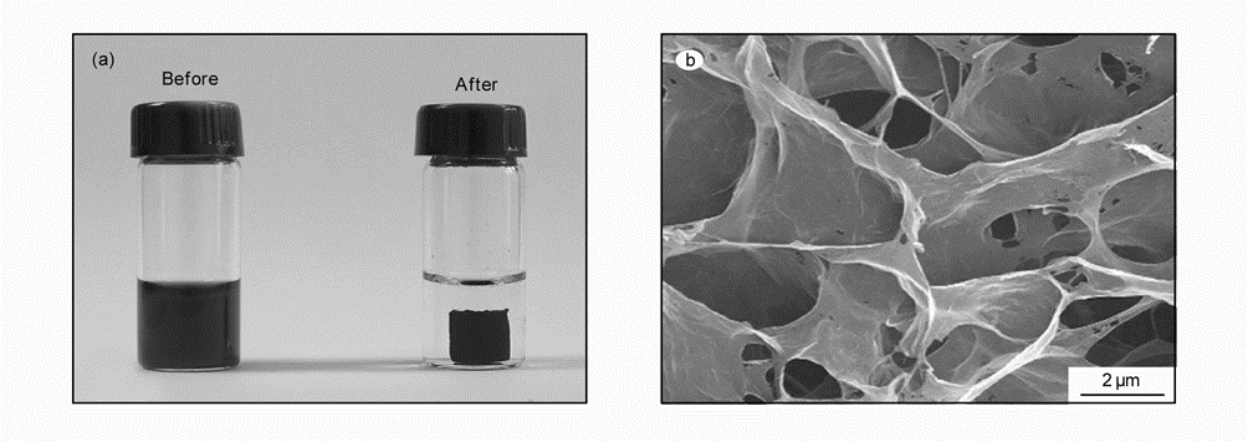

Figure 1.14: (A) Photograph of an aqueous mixture of GO (2.0 mg/mL) and sodium ascorbate before (left) and after (right) chemical reduction at 90 °C for 1.5 hours. (B) SEM image of graphene hydrogel.[57]

Various other types of macroscopic assembled graphene architectures have been proposed including graphene film or paper, graphene fiber by versatile routes for supercapacitors.[58-61] For example, Yang et al. reported a compact graphene film mediated by liquids using vacuum filtration and capillary compression, which showed a gravimetric capacitance of 167 F/g.[58] Hao et al. synthesized graphene based aerogel with a gravimetric capacitance of 197 F/g derived from chitosan.[62] All these novel 3D architectures have demonstrated to decrease transport impedances, increase electrical conductivity, SSA and mechanical strength. However, there is lack of understanding of structure-processing-property relationships which limits the use of these 3D graphene frameworks.

1.4.3 Functionalized Graphene Frameworks

A significant improvement in energy density can only be achieved by making use of materials that exhibit pseudocapacitance. Metal oxides and conductive polymers which have been investigated as a pseudocapacitors electrode materials are shown in Figure 1.7. Manganese dioxide (MnO_2) is an excellent candidate for inclusion in graphene frameworks because it is cheap, abundant, environment friendly and intensively researched in batteries. MnO_2 has a high theoretical capacitance of 1100 F/g. However, it usually delivers a specific capacitance of 200 F/g due to poor electrical conductivity and low accessible surface area for electrolyte ion. Hence, hybrid electrode architectures that incorporates nanoscopic MnO_2 films on high surface area conductive support such as graphene is an ideal way to optimize the electrochemical performance. The graphene not only increases the electrical conductivity of hybrid electrode but also provides large surface area and mechanical stability so that MnO_2 loading can be maximized.

Chen et al. synthesized an MnO_2 nanoneedle (diameter 10-50 nm and lengths 200-500 nm) - graphene oxide composite by simple soft chemical route in water-isopropyl alcohols system as shown in Figure 1.15.[63] The GO solution made by modified Hummer's method was mixed with $MnCl_2.4H_20$ in isopropyl alcohol. The mixture was well dispersed by ultrasonication for 30 minutes followed by heating it to approximately 83 °C. A $KMnO_4$ solution was added rapidly to the above boiling mixture to form MnO_2 nanoneedles according to the reaction:

$$2\ KMnO_4 + 3\ MnCl_2 + 2\ H_2O \rightarrow 5\ MnO_2 + 2\ KCl + 4\ HCl$$

Washed and dried materials with different MnO2 to graphene ratio were tested for electrochemical performance. This material achieved a specific capacitance of 210 F/g at current density of 200 mA/g in a 1 M Na_2SO_4 solution. Chen et al. demonstrated specific capacitance of nano-MnO_2 is much higher than that of its bulk counterpart.

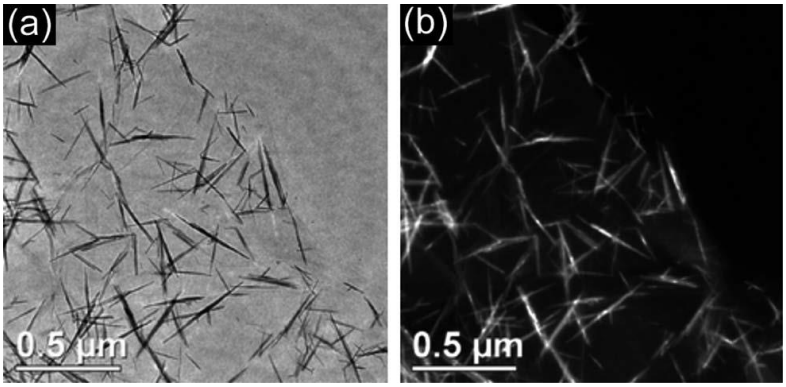

Figure 1.15: (a) Bright-field and (b) dark-field images of a MnO_2 nanoneedle–graphene oxide composite.[63]

Yan et al. proposed a simple method to synthesized nanostructured graphene-MnO_2 composites through a self-limiting deposition of nanoscale MnO_2 on the surface of graphene via microwave irradiation.[64] The GO solution made by modified Hummer's method was mixed with $KMnO_4$ powder. The suspension was stirred for 10 minutes and heated using a household microwave oven for 5 minutes. The reaction between carbon and $KMnO_4$ through MW irradiation is shown in Figure 1.16. The MnO_2 nanoparticles (5 nm -10 nm) are preferentially deposited near the edges of graphene layer because the carbon at the edges of graphene are more prone to oxidation due of high density of oxygen functional groups. The EC made with this material containing 78% MnO_2 and 20% graphene showed a specific capacitance of 300 F/g at a scan rate of 2 mV/s in a 1 M Na_2SO_4 electrolyte solution. The performance of graphene MnO_2 composite at high scan rates was better as compared to the individual materials and capacitance retention after 15000 cycles was found to be 95% at a scan rate of 2 mV/s and 75% at 500 mV/s outperforming other materials. Yan et al. concluded that the improved electrochemical

performance is due to the increased electrode conductivity in presence of graphene network, the increased effective interfacial area between MnO_2 and the electrolyte as well as better contact between the MnO_2 and graphene. Moreover, nanoscale MnO_2 particles can greatly reduce the diffusion lengths over which the electrolyte ion must transfer during the charge/discharge process.

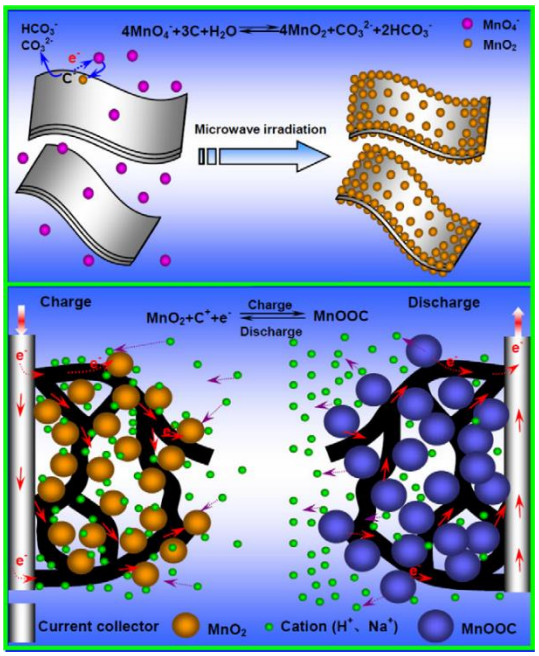

Figure 1.16: Schematic illustration for the synthesis and electrochemical performance of graphene MnO_2 composite.[66]

There have been few other groups who reported MnO_2-graphene based composite. For example, Lee et al. utilized electrodeposition of MnO_2 on graphene prepared by CVD to make the composite materials which showed a specific capacitance as high as 400 F/g.[65] Yu et al. utilized microfibers used in textile industry to form dip coated graphene nanosheets on microfibers.[66] These coated graphene microfibers were electrodeposited with MnO_2 to form a hybrid material which showed a specific capacitance of 315 F/g.[66] The common theme in all the work on graphene-MnO_2 hybrid is to develop a 3D nanostructured composite architecture that utilizes a thin layer of MnO_2 with short diffusion lengths. This is achieved by control

deposition of MnO_2 on graphene, which provides good conductivity, chemical stability and unique architecture.

1.5 Summary

The development of graphene-based electrodes for electrochemical energy storage requires a better understanding of the graphene oxide reduction and assembly of the individual 2D sheets in 3D frameworks that retain the unique properties of graphene. There are many advantages of such graphene-based nanostructures. First, the great mechanical strength of graphene allows synthesis of strong 3D frameworks. Second, because of its excellent chemical and thermal stability, graphene-based electrodes can withstand harsh conditions. Third, the electron mobility in graphene sheets improves the electronic conductivity of the electrode material and thereby improves electrochemical performance. Fourth, GO and RGO can serve as substrates for organic and inorganic species to synthesize complex functional 3D graphene frameworks such as MnO_2 decorated graphene sheets. These unique features enable graphene-based materials to serve as key components in high-performance electrochemical energy storage devices.

Chapter 2

Photolytic Release of OH• from Aqueous Graphene Oxide Dispersions

2.1 Introduction

Graphene is a highly studied carbon allotrope, owing to its large theoretical surface area and the variety of means for preparing single- or few-layer sheets.[67-70] The 2-D hexagonal nature of the conjugated sp^2 network gives rise to a number of these exquisite properties. The conducting π band of $2p_z$ electrons that are oriented perpendicular to the bonding plane provides an electronic shuttling effect that has opened up a multitude of applications for the conductive 2-D carbon. Current limitations in the processing capability of single-sheet graphene in bulk quantities renders this form of graphene useful in only a few relatively specific applications. Single sheet graphene dispersions can be prepared in a few solvents that are able to exfoliate the graphite layers,[71-74] but oxidation of graphite to graphene oxide (GO) through Hummers method[75] enables one to disperse single GO sheets in water and other polar solvents.[76, 77] The oxidation reaction exfoliates the single sheets of graphene while simultaneously driving the formation of oxygen functional groups on the surface to form GO. These functional groups primarily consist of –OH along the basal plane and –COOH along the edges with some –O– and =O groups dispersed throughout the surface.[78, 79]

GO is an insulator because of the sp^3 hybridized domains introduced during the oxidation of graphite. Reduction to reduced graphene oxide (RGO) is often desirable for the final application where electrical conductivity may be required. GO can be reduced in a variety of ways including thermal,[11, 12] chemical,[13, 14, 80, 81] electrochemical,[15, 16, 82-84] and photochemical processes.[17, 18, 85-88] Reduction of GO to RGO partially-restores the interconnected sp^2 domains to restore some degree of electrical conductivity, which depends on the reduction process

employed.[78] During the reduction process, oxygen functional groups are eliminated, and the mode of reduction is critical to the final products obtained from the released oxygen-containing groups. Photo-reduction has been studied in a number of cases to facilitate better understanding of the mechanisms involved,[5, 18, 89, 90] the origin of GO fluorescence,[91] the environmental fate of GO,[92] and the potential for GO to serve as a photocatalyst.[93-95] Much discussion has ensued on the mechanisms involved in both photochemical and chemical reduction of GO to RGO.[96-98] In this chapter, new findings that demonstrate the photochemical reduction of GO to RGO in aqueous dispersions gives way to the photolytic release of hydroxyl radicals (OH●) are presented. This new insight has a number of implications in the stability of GO and unveils potential new means to leverage OH● photolysis products. Prior work has shown the susceptibility of RGO to localized OH● attack to form nanoporous holey graphene dispersions with Au nanoparticle catalyst.[5] Interestingly, without Au catalyst the OH● attack leads to high density of –OH groups on the GO surface. Here, the reverse reaction has been considered, in which OH● are liberated in high yield with UV photons, and to a lesser extent, photons in the visible region. The results reported here provide new insights into the photostability of GO, mechanism of aqueous photoreduction, and offer new opportunities to employ GO for solar-driven applications.

2.2 Experimental

2.2.1 Material Synthesis and Characterization

GO was synthesized using a modified Hummers method. Two grams of graphite powder (Alfa Aesar, 325 mesh) was sonicated and stirred in an ice bath in 92 mL of concentrated H_2SO_4 (Amresco) with 2 g of $NaNO_3$ (Alfa Aesar, 99%) for 30 minutes, after which 12 g of $KMnO_4$ (Alfa Aesar, 99%) was very slowly added. Sonication continued for 30 minutes following addition of $KMnO_4$, after which the flask was removed and allowed to stir slowly overnight at

30 °C. Next, 100 mL of deionized (DI) H_2O was added dropwise followed by 1 hour of stirring. Finally, 600 mL of H_2O_2 (EMD Milipore, 30% w/w) diluted to 3% w/w was added into the flask, yielding a yellowish-brown GO suspension. The suspension was washed three times with concentrated 1 M HCl (BDH) via centrifuge, and finally five times with DI H_2O. The RGO was synthesized by irradiating 0.2 mg/mL suspension of GO in a quartz cuvette with a Xenon lamp (Newport 69907, 150 W) for 30 minutes. To oxidize RGO back to GO, 100 μL of 30% w/w H_2O_2 was added to 3 mL RGO (0.2 mg/mL) and irradiated with Xenon lamp for 120 minutes. UV spectra were taken at regular intervals with Agilent Cary 60 UV-Vis Spectrophotometer Agilent to monitor the progress of the reaction for GO→RGO and RGO→GO. GO and RGO were characterized using a Thermo Nicolet AVATAR 360 FTIR spectrometer.

2.2.2 Photoemission Experiments

2 mL mixture of 0.2 M terephthalic acid (TA) (Alfa Aesar, 98%) and 1 M NaOH (Amresco) was mixed with 1 mL of GO having varying concentration (2 mg/mL, 5 mg/mL and 10 mg/mL). These samples were irradiated with Newport Xenon lamp for two hours. Another set of same samples were prepared which were irradiated for 16 hours. Samples were excited at λ = 330 nm to obtain fluorescence spectra on SpectraMax i3 from Molecular Devices.

2.2.3 Ultrafast Detection and Quantum Yield Experiments

Transient absorption measurements were recorded using a Clark MXR CPA-2101 (fundamental wavelength 775 nm, pulse duration 130 fs, repetition rate 1 kHz) incorporating ShapeShifter software provided by Clark MXR. The fundamental laser output was split into a pump light and a probe light, which account for 95% and 5% of the output, respectively. The probe light beam passed through an optical delay stage and then was focused on a titanium: sapphire crystal to provide a white light continuum. The pump light beam was directed through a second harmonic frequency doubler to produce 387 nm pump beam. Pump energy was at ~10

μJ/pulse. Samples consisted of GO and GO+KSCN at concentration of 0.05 mg/mL GO and 0.1 M KSCN. A 1 cm path length (quartz cuvette) was required to enable sufficient buildup of thiocyanate radical for optical detection. Optically-flat cells were utilized for the spectroscopy measurements.

2.2.4 GO + Dye Experiment

10 mg/mL GO (15 μL) was added to a 3 mL of 20 μM Naphthol Blue Black dye (MP Biomedicals) solution and was irradiated with Xenon lamp (Newport 69907, 150 W). The solution was photographed at different times from 0 to 56 hours. In another experiment, a dried GO flake was added to 3 mL of 20 μM Naphthol Blue Black dye (MP Biomedicals) solution and was irradiated with Xenon lamp (Newport 69907, 150 W. UV spectra were taken at regular intervals for 120 minutes with Agilent Cary 60 UV-Vis Spectrophotometer.

2.3 Results and Discussion

The reduction of GO can be tracked using UV-visible spectroscopy since the absorption of GO is dependent on the degree of oxidation.[5] GO suspensions were irradiated for 30 minutes with 100 mW/cm^2 white light produced from Xenon lamp and tracked the absorption change during its conversion to RGO. A small aliquot of H_2O_2 was introduced to demonstrate the reverse photolysis-driven re-oxidation of the RGO to GO via OH●. The UV-visible absorption spectra show both conversion of GO to RGO and RGO to GO are presented in Figure 2.1 (A). The oxidation of RGO decreases the UV-visible absorption until it returns to the initial GO absorption profile. We suspect the oxidation required substantially longer irradiation time since H_2O_2 is non-selective towards the oxidation of GO and has high rates of reactivity with other aqueous species. Thus, the rate of reaction will depend significantly on proximity and diffusion of OH● to the RGO surface following photolysis of H_2O_2. FTIR spectroscopy results for the pristine GO and photochemically-reduced RGO show the loss of oxygen functional groups is

significantly directed toward the –OH stretching region as observed in Figure 2.1 (B). GO exhibits a strong –OH stretching band, which is consequently eliminated following the 30 minutes irradiation period. These results point to the liberation of –OH functional groups during photochemical reduction.

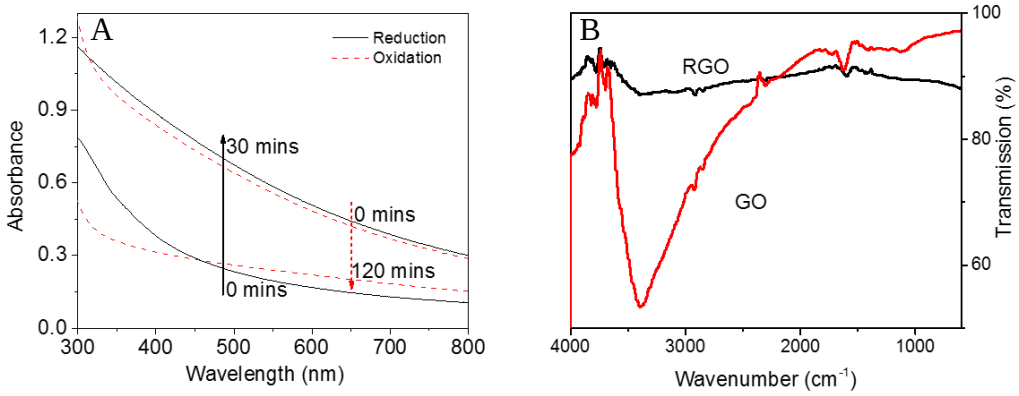

Figure 2.1 (A) UV visible absorption spectra for GO, RGO, and oxidized RGO (ORGO) showing the photochemical changes during irradiation lead to reversible changes in absorption. (B) FTIR analysis of GO and RGO demonstrates the –OH stretching is significantly impacted by photochemical reduction process.

The digital photographs provided in Figure 2.2 offer a visual guide to the reversibility of the photochemical reduction and oxidation process. Previous work focusing on the photochemical reduction process led to the researchers proposing an n to π* transition from the labile and charge-dense oxygen functional groups to the locally-bonded carbon moiety.[91] The hypothesis that was sought to probe was the following: if the n to π* transition drives the photochemical reduction of GO, what is the chemical nature of the released –OH functional group? Instinctually, following from the FTIR spectroscopy, OH● was suspected as the photon-induced reaction product (Reaction Scheme 1). Steady state irradiation experiments were also carried out by employing the OH● fluorescent probe molecule, terephthalic acid (TA), to determine whether OH● was released during the steady state irradiation of GO. TA reacts irreversibly with OH● to form 2-hydroxyterephthalic acid (TAOH) as shown in Reaction

Scheme 2.

Reaction Scheme 1

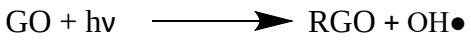

Reaction Scheme 2

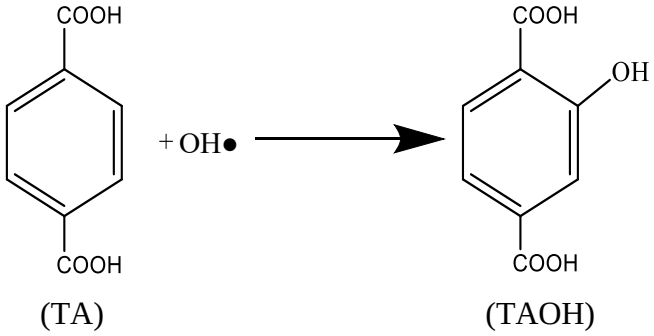

Figure 2.2: Digital photographs of GO, RGO, and ORGO.

The results of the irradiation experiments are presented in Figure 2.3. First, the concentration of GO is varied in presence of TA and monitored the peak fluorescence intensity for TAOH at ~435 nm with 330 nm excitation. Figures 2.3 (A) and 2.3 (B) show the fluorescence intensity after 2 hours and 16 hours irradiation of GO samples with varying concentration, respectively. The fluorescence intensity after 2 hours of irradiation follows nearly a linear increase with respect to GO concentration, suggesting that additional mass of GO, and by default the number of –OH functional groups present, leads to higher yield of TAOH *via* photolytic OH● release during irradiation. However, after 16 hours of irradiation,

we observe a shift in the relationship between GO concentration and OH● yield with 5 mg/mL giving way to higher TAOH fluorescence as shown in Figure 2.3 (B). This phenomenon can be attributed to the parasitic light absorption by the RGO at high concentrations that effectively blocks further GO absorption. This result suggests that to effectively design GO for photochemical applications, parasitic photon scavenging must be considered with regard to concentration. Then, the irradiation time was varied for a 2.0 mg/mL GO dispersion and TAOH fluorescence was recorded as shown in Figure 2.3 (C). As the irradiation time was increased from 0 to 16 hours, a corresponding increase in OH● yield is observed in the higher fluorescence peak intensity for TAOH. These results unequivocally point to photolytic release of OH● from GO during photochemical reduction in aqueous media; a finding with strong implications for GO in photochemical/photocatalytic applications.

It has been well established that a number of electronic transitions are possible in GO in the UV region. Hence, it is important to understand the usefulness of GO in solar-based photolytic applications such as remediation of aqueous contaminants. Since UV photons correspond to ~3% of the AM 1.5 solar spectrum, 400 nm filter was employed to determine whether photolytic release of OH• was driven solely by UV photons or by visible photons as well. Figure 2.3 (D) shows the evolution of the fluorescence peak at 435 nm following irradiation with 400 nm long pass filter and demonstrates visible light excitation can drive photolysis of GO to produce OH●, although to a significantly lower extent (~20%). While the mechanism for the visible light excitation is not clear at this point, we posit that the density of sp^3 domains and the chemical make-up of neighboring functional groups and other species can alter the local energy gap of the electronic transitions, much as edge functional groups and domain size are strongly correlated to photoemission characteristics of GO.[91, 99, 100]

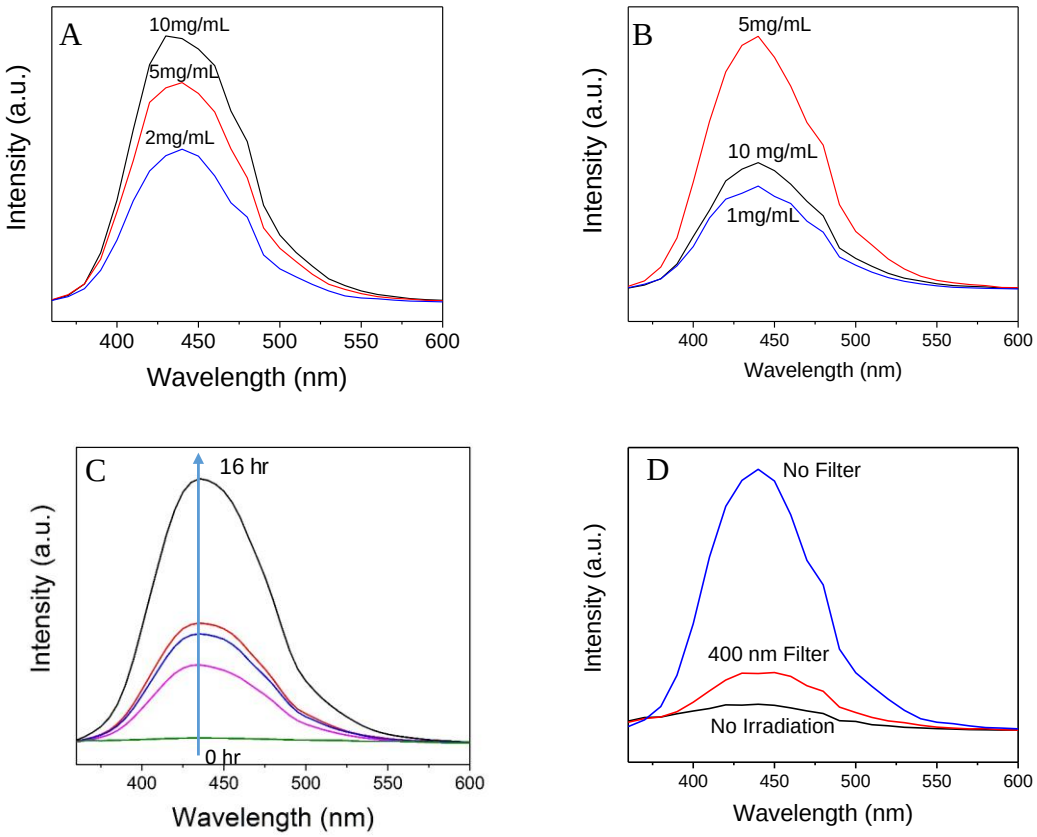

Figure 2.3: Photoluminescence measurements of GO dispersions at different concentrations with (A) 2 hours and (B) 16 hours of irradiation. (C) Photoluminescence measurements of GO dispersions with variable irradiation time at concentration of 2.0 mg/mL (D) Visible light (> 400 nm) induces photolytic release of OH●, albeit at a much lower yield than when UV photons are not filtered (concentration of 2.0 mg/mL). Data points represent an average of three measurements.

Quantum yield of the OH● evolution from GO was elucidated by employing ultrafast transient absorption spectroscopy with the OH● probe molecule SCN^{-}. We posited the surface association between GO and SCN^{-} would be sufficient to overcome diffusion limitations and enable rapid capture of the photolytic OH● evolved during photoexcitation with 130 fs pumping at 387 nm photon energy. Figures 2.4 (A) and 2.4 (B) show the transient spectra recorded for GO and GO+KSCN in aqueous solutions. In transient absorption spectroscopy, light absorption spectra of the sample is recorded before and after excitation with a pump light. The difference of the absorption spectra (ΔOD) is plotted against wavelength of light. In Figure 2.4 (A) one

can observe the rapid rise and fall of the transient absorption in the GO-only sample, which is in relative agreement with prior work on ultrafast dynamics of GO.[99, 101-103] However, with the introduction of the SCN^- the transient spectra show the rise of a peak centered at ~475 nm (Figure 2.4 (B)), which corresponds to λ_{max} for the thiocyanate dimer radical species, $(SCN)_2^{-\bullet}$.[104, 105] The time-resolved rise in transient absorption in the GO+KSCN sample at 475 nm is illustrated temporally in Figure 2.4 (C). This rise at 475 nm stands in stark contrast to the transient spectral behavior for GO-only sample, which shows no significant ΔOD at this wavelength at times longer than 2 ps. These results in conjunction with those presented in Figure 2.3 further supports our conclusion that photoexcitation of GO in aqueous suspensions leads to photolytic conversion of –OH functional groups to OH●. The bottom right quadrant in Figure 2.4 depicts the proposed reaction mechanism leading to the transient absorption at 475 nm. The primary quantum yield for the photochemical process was estimated to be at $\Phi \approx 0.85$ by employing the extinction of thiocyanate radical at 475 nm and pump energy of 9.8 μJ/pulse. This estimate suggests a highly efficient photolytic conversion process for –OH to OH● under 387 nm excitation.

The photolytic release of OH● from GO offers new strategies to design advanced carbon materials with high surface area for photochemical and photocatalytic applications. The stability of the GO against reduction to RGO must be improved for photocatalytic systems, but GO is suitable in its current state for environmental remediation of aqueous organic contaminants *via* OH●. The rich surface chemistry of GO and the segregated sp^2 and sp^3 domains provide electrostatic binding sites for both polar and non-polar molecules, and these binding sites localize organic contaminants at the GO surface where OH● are released, enabling close proximity between the short-lived OH● and contaminant molecules. Considering the high

reactivity and rapid kinetics associated with OH●, surface association between GO and contaminant molecules minimizes non-selective OH● utilization in the photolytic remediation process.

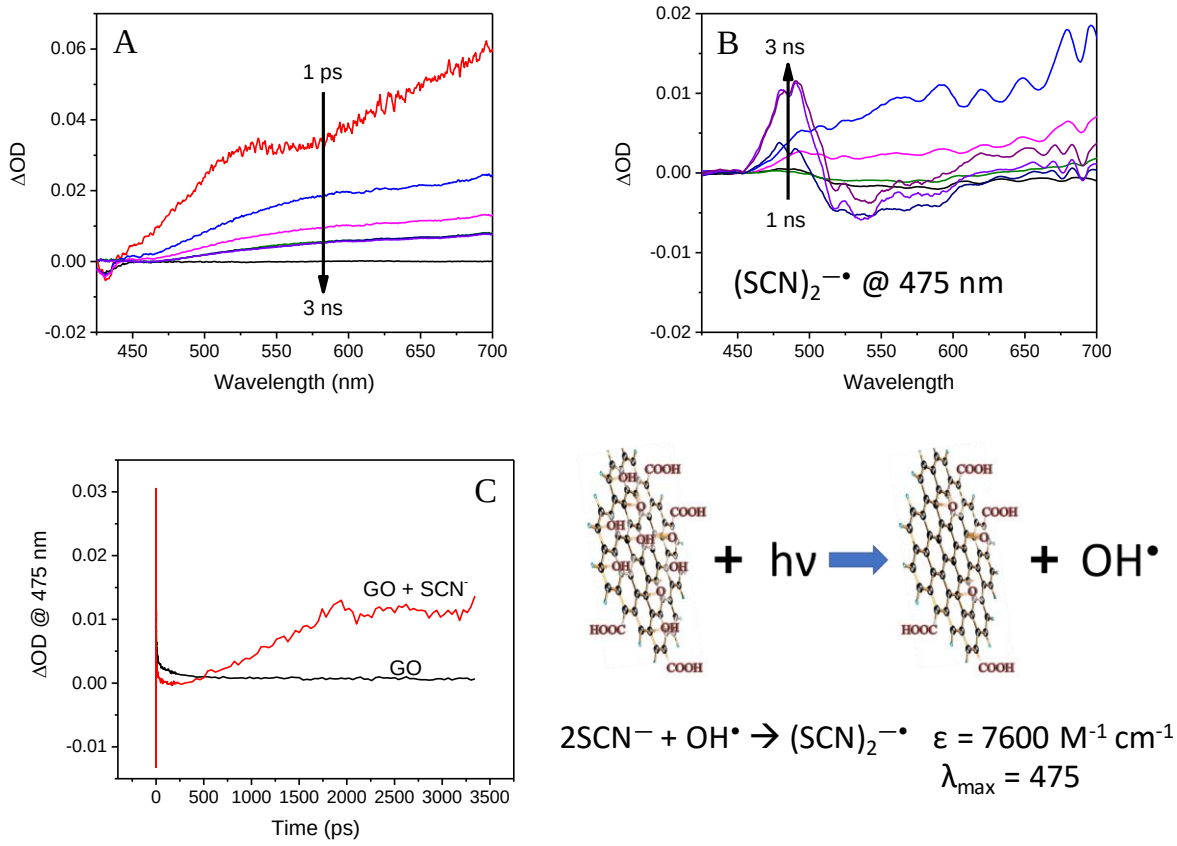

Figure 2.4: Transient absorption spectra without (A) and with (B) OH● capture probe SCN—. Evolution of transient thiocyanate radical species occurs within ~1 ns as indicated in the time-resolved transient features at 475 nm (C). The overall reaction scheme is provided in the bottom right quadrant.

In order to test the hypothesis that GO can serve as a remediation agent, a dried GO flake was introduced to a suspension of recalcitrant organic dye, Naphthol Blue Black (NBB), and subjected to AM 1.5 simulated solar flux at 100 mW/cm^2. The UV-visible absorption of the dye was monitored as a function of irradiation time. Figure 2.5 (A) shows the evolution of the spectra with 120 minutes of irradiation. One can observe the rapid increase in absorption in the region λ = 620 nm. This suggests the dye may form a complex with GO during irradiation,

which facilitates its interaction with OH● at the GO surface and subsequent degradation. Since the dye also absorbs photons during the irradiation experiment, an additional control experiment confirms the dye stability during irradiation without presence of GO. Continued irradiation of GO in aqueous solution leads to its eventual aggregation and collapse from the dispersion as a result of the elimination of the polar functional groups.[18, 98] These polar functional groups provide electrostatic repulsion forces between GO sheets and stabilize the GO suspension in polar solvents. Upon significant reduction of GO (regardless of the means of reduction) sp^2 domains increase in size to a critical threshold, after which π-π interactions begin to dominate and multilayer aggregates of RGO are formed.[18] This breaks the suspension and results in flocs settling out as a graphitic oxide material. It is posited that this unique characteristic of GO/RGO can be harnessed as part of a multifunctional remediation material by aggregating and settling naturally after the functional groups are photolytically eliminated. This inherent separation process circumvents the need for extraction of RGO from remediated water. As a proof of concept for the multifunctional remediation-separation capability of the GO dispersions, we irradiated a GO-dye mixture for 56 hours continuously and collected digital photos of the progress of the reaction and separation. Figure 2.5 (C) shows the evolution of the dark color resulting from GO to RGO conversion with disappearance of the blue dye coloration and small flocs at the bottom of the cuvette after 5 hours. Further exposure to the light led to continued accumulation of flocs with nearly complete reduction and settling after 56 hours.

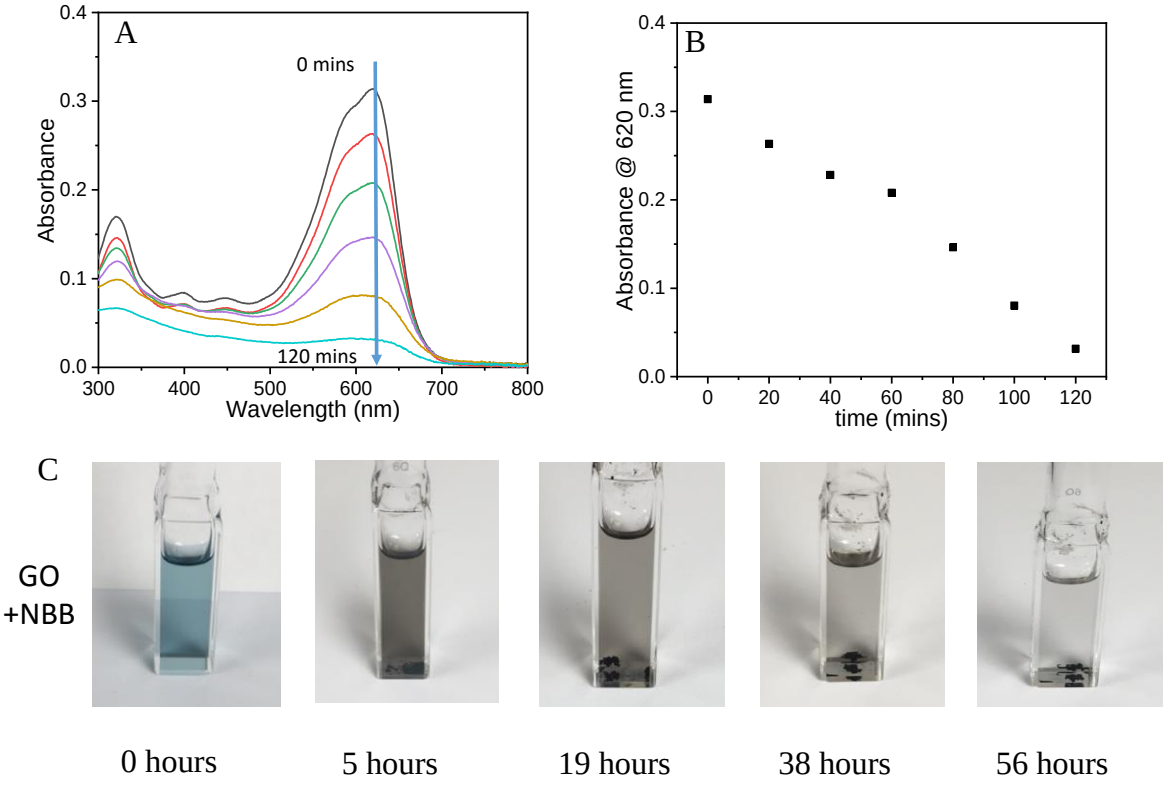

Figure 2.5: (A) Time evolution of the UV-visible absorption spectra with GO+H_2O taken as baseline during 30-minute irradiation. (B) Corrected absorbance values at the 620 nm naphthol blue-black dye peak after subtracting the absorption of the partially reduced GO at each time point. The decrease in absorption of the dye is indicative of the photolytic remediation process mediated via OH●. (C) Digital photographs of the coloration changes with continued irradiation of the dye-GO mixture. Flocs accumulate at the bottom of the cuvette after 56 hours of irradiation.

2.4 Conclusions

The photolytic evolution of OH● from GO dispersions with high quantum yield was successfully demonstrated. These findings imply some degree of reversibility between the OH● attack on RGO reported previously[33] and the OH● release from GO. Aqueous contaminant remediation is facile using GO as a source for OH●, and the conversion of GO to RGO during photolysis enables inherent separation from the aqueous dispersion following degradation of the organic contaminant. This inherent aggregation-induced separation process is driven by the growth of sp^2 domain size during photochemical reduction (sp^3 to sp^2), which when sufficient

size of these domains is attained, π-π bonding networks are reestablished. Further work is underway to identify the mechanisms and kinetics associated with the photolytic OH● release under various experimental conditions and photon excitation energy, which may prove insightful to realizing a form of GO that is stable under UV/visible irradiation. Further implications regarding the environmental fate of GO arise now, considering its role as both a *source* and *sink* for OH●.

Chapter 3

Structure - Processing - Property Relationships of Self-Assembled 3D Graphene Frameworks

3.1 Introduction

Recently, nanocarbons such as carbon nanofibers (CNFs), carbon nanotubes (CNTs) and graphene have been utilized as basic building blocks to build nanostructures for energy storage applications.[25] Graphene has shown the most promising results due to its exceptional electronic, thermal and mechanical properties.[1-3] However, strong van der Waals attraction and π-π interactions between graphene sheets results in restacking of individual sheets to form graphite-like structures, losing their unique properties such as high specific surface area (SSA) and electrical conductivity.[29-31] The true potential of utilizing graphene in electrochemical capacitors lies in the ability to assemble the individual 2D sheets into 3D frameworks that retain the unique properties of graphene and provide hierarchical porous networks for efficient ion diffusion.[4, 25, 47, 106-108] Such 3D graphene frameworks (3DGFs) have been developed using two well-known methods - chemical vapor deposition (CVD) and self-assembly.[25, 109-111]

CVD process uses metal substrates as templates to produced 3D structures. This has been demonstrated by the direct growth of graphene on 3D templates such as commercially available Ni foam,[112] anodic aluminum oxide,[113] MgO,[114] nickel-coated pyrolyzed photoresist films,[115] and metallic salts.[116] Although CVD is a technique that produces 3DGF with controlled morphologies and properties, it requires very expensive infrastructure.

Self-assembly of 2D materials is achieved by controlled destabilization of a dispersion that is stable due to a delicate balance between attractive and repulsive interactions.[117] A common method of synthesizing 3DGF is through controlled reduction of graphene oxide. GO sheets in an aqueous dispersion remain separated due to the dominance of repulsive forces

among negatively charged ionized carboxylic groups at the edges of the sheets.[21] After reduction, the repulsive forces are neutralized by π-π interactions and hydrophobic interactions arising due to the removal of hydroxyl and epoxy functional groups from the basal plane of graphene sheets and subsequent recovery of sp^2 network.[118] The functional groups that remain on the graphene sheets hold water as a spacer and prevent the restacking of the graphene sheets. This results in the formation of an interconnected network of 2D sheets possessing a 3D structure. There are many other ways to assemble graphene into 3DGFs such as the addition of cross-linkers,[119-123] freeze-drying,[124] controlled filtration.[125] Major advantages of the self-assembly process are - (1) ease of hybridization with other materials, (2) solution-based facile processing, (3) high throughput, and (4) inexpensive infrastructure requirement. The focus of this work is on chemically reduced self-assembled 3DGFs.

There is a dearth of studies that focus on understanding charge storage and ion transport ability of 3DGFs. A literature review of previous studies focusing on recent advances in the synthesis of 3D self-assembled graphene frameworks and their applications in electrochemical capacitors is shown in Table 3.1. This table includes only the studies in which 3DGFs were synthesized using the reduction of GO. Gaoquan Shi's group was the first to report the self-assembly of graphene via reduction of GO, which required hydrothermal reactor operating at 180 °C for 6 hours.[106] They showed that a typical 3DGF is a hydrogel having a highly interconnected 3D graphene network (~2 wt. %) which is filled with water (~98 wt. %). This self-assembled structure showed a high electrical conductivity of 0.5 S/m, a hierarchical porous structure with a large specific surface area. The 3DGF showed excellent mechanical strength, which was 1-3 orders of magnitude higher than those of conventional self-assembled hydrogels. The 3DGFs synthesized by Shi's group were directly used as electrochemical capacitor

electrodes without any other additives and exhibited a high specific capacitance of 160 F/g in 1 M H_2SO_4 electrolyte, about 33% higher than that of agglomerated RGO powders under the same test conditions.[106] This initial study provided a new fundamental understanding of the self-assembly mechanism of graphene as a basic building block and inspired subsequent studies on 3DGFs. The hydrothermal reduction method required high temperature and pressure conditions, which was improved by Shi et al.[57] and Liu et al.[126] They utilized a chemical reduction method in which the reaction was completed in less than 2 hours below 100 °C.[57, 126] Moreover, the chemical reduction reaction did not require autoclaves that were necessary for hydrothermal reduction. The 3DGFs prepared by chemical reduction displayed similar porous structure and mechanical properties. The electrical conductivity, however, was two times higher than that 3DGFs produced by hydrothermal reduction.[57, 126] This was because of a higher degree of reduction achieved during chemical reduction. The capacitance exhibited by the 3DGF was 240 F/g, an increment of 50% as compared to hydrothermally reduced 3DGF.[57] More recently, Duan et al. prepared a new 3DGF built from holey graphene sheets through a hydrothermal process.[56] The process involved simultaneous etching of nanopores within the graphene plane by H_2O_2 and self-assembly of graphene into a 3D network. Hydrogen peroxide was mixed with a dispersed solution of GO. The mixture was heated at 180 °C for 6 hours in a hydrothermal reactor. During the reaction, GO sheets were reduced creating freestanding porous holey graphene. Hydrogen peroxide helped in partially oxidizing carbon atoms around active defective sites and form nanopores in the GO sheets. These nanopores are distributed throughout the GO sheets because of the abundant presence of defective carbon sites. The degree of etching can be controlled by the amount of H_2O_2. The holey 3DGF exhibited a highly porous network with an ultrahigh accessible SSA of 1560 m^2/g. Most importantly, the 3DGFs

showed excellent rate capability and superior cycling stability, which was attributed to efficient ion diffusion and fast electron transport. Holey 3DGF was also prepared by chemical reduction of holey GO with L-Ascorbic acid and achieved similar capacitive performances.[127]

Table 3.1: Literature review of previous studies on graphene frameworks

Year	PI	Graphite flake size	Concentration (mg/mL)	Reduction method	Electrolyte	Capacitance (F/g)	ESR (Ω)	Tau (s)
2010	Gaoquan Shi	325 mesh	2	Hydrothermal	1M H_2SO_4	160	-	-
2011	Gaoquan Shi	325 mesh	2	Chemical	1M H_2SO_4	240	-	-
2011	Bin Liu	325 mesh	4	Chemical	6M KOH	128	-	-
2014	Xiangfeng Duan	-	2	Hydrothermal	6M KOH	208	1.3	0.49
2014	Xiangfeng Duan	-	2	Hydrothermal	6M KOH	310	0.6	0.17
2015	Xiangfeng Duan	-	2	Chemical	1M H_2SO_4	283	0.8	-

All these studies pointed out several advantages of the self-assembled 3DGFs over other 3D graphene and carbon structures. First, the self-assembled 3DGFs are highly porous materials with high SSA where graphene sheets are interlocked together to prevent them from restacking. Second, the 3DGFS are hydrogels that are fully hydrated and can allow a direct exchange of various electrolytes. This ensures that electrochemically active surface of the electrode is fully wetted by electrolyte and accessible to the electrolyte ions, which is difficult to achieve in conventional porous carbon material.[26, 128, 44] Third, the solvated 3DGFs can be mechanically compressed to form free-standing dense films without causing restacking to achieve improved volumetric capacitance. Lastly, the pores of 3DGF are sufficiently large and well-integrated into a hierarchical porous architecture for efficient ion transport, which is not possible in activated carbon due to the presence of isolated ultra-small micropores that are inaccessible to the electrolyte ions.[36]

In this chapter, the effect of GO sheets size (aspect ratio), GO dispersion concentration and GO dispersion pH on electrochemical properties of 3D graphene frameworks that are prepared by chemical reduction of GO has been discussed. The effects of GO sheet size on the

amphiphilicity of GO sheets,[129] buckling amplitude of individual sheets,[130] rheological properties of dispersions,[131-134] and conductivity of composite materials[135, 136] have already been demonstrated. Therefore, it is plausible to argue that self-assembly will result in sheet size-dependent architecture, whose electrochemical properties are yet to be explored. GO dispersions utilized in the abovementioned studies were synthesized from a graphite precursor of a single flake size of 325 mesh (~ 44 μm). Graphene frameworks were synthesized from a dispersion of GO of 2.0 mg/mL except for one study which utilized 4.0 mg/mL. The variation in electrochemical properties and microstructure of reduction induced self-assembled graphene frameworks with respect to the GO sheet size and concentration have not been reported until now. For this study, GO samples with two different sheet size were prepared - (a) small GO using graphite flake size of 325 mesh (~ 44 μm), and (b) ultra-large graphene oxide (UL-GO) using graphite flake size of 50 mesh (~ 297 μm).

3.2 Experiments

3.2.1 Small GO and UL-GO Synthesis

Small GO was synthesized using a modified Hummers' method.[5] 2 g of graphite powder (Alfa Aesar, 325 mesh) and 2 g of $NaNO_3$ (Alfa Aesar, 99%) in 92 mL of concentrated H_2SO_4 (Amresco) was sonicated in an ice bath for 30 minutes. After this, 12 g of $KMnO_4$ (Alfa Aesar, 99%) was slowly added while keeping the temperature below 20 °C. Sonication was continued for 30 minutes following the addition of $KMnO_4$, after which the mixture was allowed to stir slowly overnight at 30 °C. The next day, 100 mL of deionized (DI) H_2O was added dropwise followed by 1 hour of stirring. Then, 600 mL H_2O_2 (EMD Milipore, 30% w/w) diluted to 3% w/w was added into the flask, yielding a yellowish-brown GO suspension. The suspension was washed three times with concentrated 1 M HCl (BDH) via centrifuge, and finally five times with DI H_2O.

UL-GO was synthesized using a method described by Aboutalebi et al.[137] The synthesis utilizes intumescent flake graphite, also known as expandable graphite, a form of intercalated graphite (with sulfate). The intumescent flake graphite can be expanded 300 times in volume on the application of rapid heat which converts the intercalant into a gas phase.[138] Gas formation results in an increased pressure between the sheets that forces the adjacent graphene layers to separate. Rapid heating can be achieved in a furnace by introducing the sample at 1000 °C for 10 seconds. This method requires a furnace with a large enough volume to accommodate the expanded graphite. Additionally, a mechanism is required where the introduction of intumescent graphite and recovery of expanded graphite is quick and safe. Exposure to high temperature for more than 10 seconds will lead to the complete oxidation and loss of material unless this is done in an inert environment. Because of abovementioned complications, a simpler method using microwave (MW) irradiation was utilized to expand graphite.[139] The MW reaction can be performed at room temperature in a short time with less energy consumption.

For UL-GO synthesis, 1 g of intumescent flake graphite (Asbury, 50 mesh) was irradiated with microwaves in a 1200 W commercial microwave (Panasonic NE-12523) with full power for 20 seconds, which caused a sudden expansion of graphite. Expanded graphite in 230 mL H_2SO_4 (Amresco) was stirred for 72 hours to allow the acid to diffuse inside the graphene layers. 10 g of $KMnO_4$ (Alfa Aesar, 99%) was added slowly to the mixture to start the oxidation reaction, which was completed under stirring for 48 hours. Next, 200 mL of H_2O was added dropwise while maintaining temperature below 20 °C using an ice-bath. Then, 50 mL of 30% H_2O_2 was added to get a yellowish golden suspension of UL-GO. The suspension was washed three times with 1 M HCl and five times with DI water using a centrifuge.

GO and UL-GO dispersion synthesized from these methods exhibited a pH ~ 3 after washing. The pH was adjusted to ~10 by adding NH_4OH to increase the stability of dispersions.[21] For the size and concertation study GO and UL-GO dispersions with pH ~ 10 were utilized. For pH study, the UL-GO dispersions with pH ~ 3 and pH ~ 10 were utilized.

Scanning electron microscope (SEM) imaging of small GO and UL-GO sheets was carried out by depositing the sheets from a dispersion of 50 µg/mL on a silanized silicon wafer. Silane solution was prepared by mixing 3-aminopropyltriethoxysilane (Aldrich) with water in a ratio 1:9 by volume. Precut silicon wafers were silanized by immersing in silane solution for 30 minutes followed by washing with DI water. GO sheets were deposited by immersing the substrate in the dispersion for 5 seconds followed by immersing in DI water for 30 seconds. The substrate was air-dried and then used for SEM imaging.

Figure 3.1 (A) and (B) show the SEM images of small GO and UL-GO sheets taken on a JEOL JSM-7000 field emission microscope. Multiple images of the small GO and UL-GO samples were taken. More than 100 particles were analyzed using image processing software ImageJ to develop area distributions for small GO and UL-GO particles as shown in Figure 3.1 (B) and (D), respectively. The average area of the GO sheets was 0.27 μm^2 with a standard deviation of 0.23 μm^2. The average area and standard deviation for UL-GO was 11 μm^2 and 21 μm^2, respectively, which is two orders of magnitude larger as compared to small GO. The area distribution of small GO and UL-GO sheets presented here is qualitatively similar to the results reported before by Lin et al.[136] The SEM images of GO and UL-GO show the presence of very tiny sheets for which accurate area measurements are not possible because of poor image resolution at higher magnification. However, the mass fraction of such tiny sheets is negligible. It is important to note that both GO and UL-GO samples have a broad particle size distribution.

Hence, results presented here could be refined in future by employing techniques to synthesize GO sheets with narrow particle size distribution.[140]

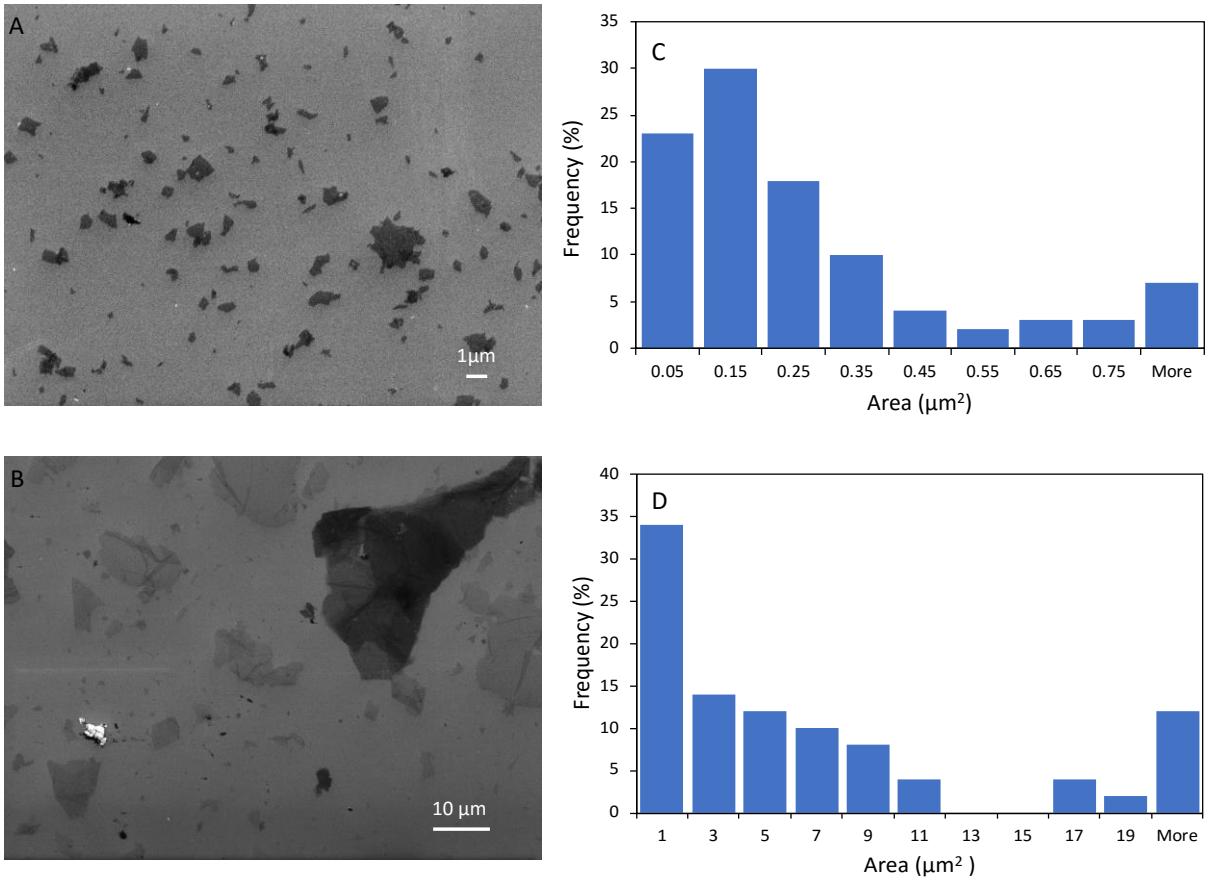

Figure 3.1: SEM micrographs of (A) Small GO and (C) UL-GO; size distribution of (B) small GO and (D) UL-GO after analyzing the SEM micrographs with an image processing software ImageJ.

3.2.2 Synthesis of 3D Graphene Frameworks

Sodium borohydride and hydrazine are known to be most common reducing agents for GO;[141] however evolution of gaseous products during reduction leads to non-uniform 3D graphene frameworks.[126] Therefore, L-ascorbic, an environmentally friendly reducing agent is utilized to prepare 3D graphene frameworks. The reaction of GO with L-Ascorbic acid does not produce gaseous products and hence uniform 3D graphene frameworks are formed. Various groups have demonstrated that RGO produced from L-ascorbic acid has high electronic

conductivity due to a high degree of reduction.[22, 98] For this study, 3D graphene frameworks were synthesized using a method similar to described in the literature.[57, 126]

For the GO sheet size study, three different samples were synthesized using - (1) a dispersion of small GO to make graphene frameworks (GF), (2) a dispersion of UL-GO to make large graphene frameworks (LGF), and (3) a dispersion of 1:1 GO and UL-GO to make GF+LGF. 2 mL of 2.5 mg/mL dispersion containing 0.1 M of L-Ascorbic acid were transferred to a 10 mL vial, which was kept inside an oil-bath maintained at a temperature of 90 °C for 90 minutes. The resulting GF was cooled for a few hours and then soaked in DI water overnight to remove the impurities. The water-washing step was repeated two more times. For concentration study GF was synthesized from small GO of varied concentration from 2.0 mg/mL to 12 mg/mL and LGF was synthesized from UL-GO of varied concentration from 0.5 mg/mL to 4.0 mg/mL.

At concentrations higher than 12 mg/mL for GO and 4.0 mg/mL for UL-GO, the graphene frameworks formed displayed a distorted shape. At high concentrations, the GO and UL-GO dispersions exhibited gel-like phases on visual observation. Hence the distorted shape of graphene frameworks can be attributed to the inhomogeneous reduction reaction caused by improper mixing of reducing agent with the gel-like GO phase. The reaction scheme with digital photographs of GO dispersion and fully formed graphene framework is shown in Figure 3.2.

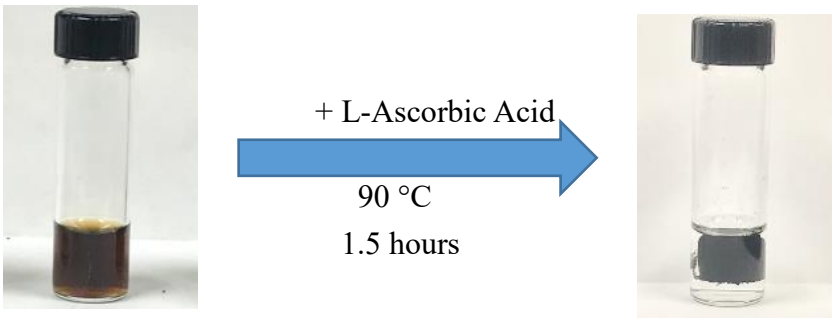

Figure 3.2: Digital images of 2.5 mg/mL graphene oxide dispersion and self-assembled graphene frameworks.

3.2.3 Electrode Fabrications and Electrochemical Characterization

The water washed GF was soaked in 6 M KOH electrolyte solution for 12 hours replacing the KOH solution every 4 hours to get rid of trace impurities. GF was then cut into thin slices and pressed onto nickel foam with a hydraulic press under a pressure of 20 MPa for 20 seconds (Figure 3.3 (A)). Nickel foam is often utilized as a current collector for electrodes because of the strong mechanical adhesion achieved between nickel foam and the active material.[28] Nickel is also non-reactive towards KOH as compared to another widely used current collector material, aluminum, which reacts violently with KOH. The fabricated electrode, known as the working electrode (WE) was soaked in an electrolyte solution for six hours before performing electrochemical tests. All the tests were performed using a Gamry Interface 1000 potentiostat in a 3-electrode setup as shown in Figure 3.3 (B) with Ag/AgCl as a reference electrode (RE), Pt wire as a counter electrode (CE) and 6 M KOH as an electrolyte.

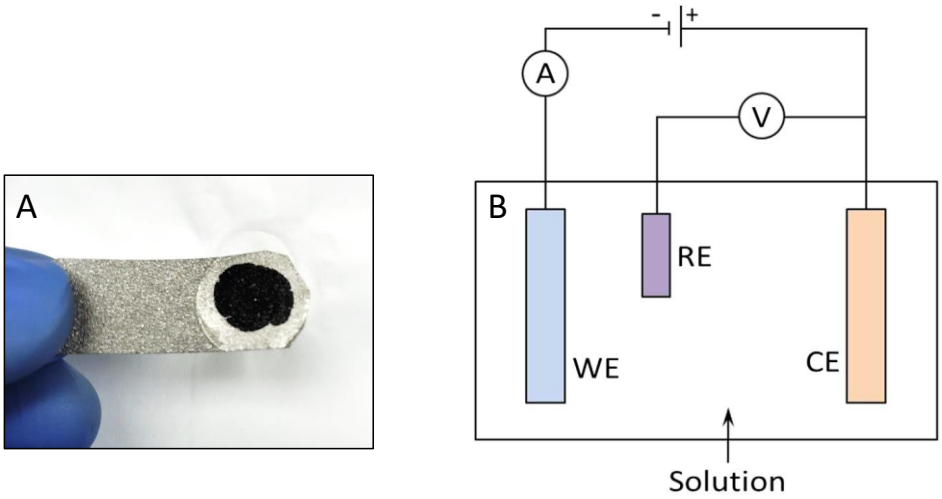

Figure 3.3: (A) Self-assembled graphene framework after pressing it on nickel foam, (B) schematic of the 3-electrode setup to perform electrochemical tests.

A potentiostat is an electronic instrument that varies the potential or current of the working electrode with respect to a reference electrode of known potential. The function of the counter electrode is to enable the passage of charge to maintain charge neutrality potential by adjusting its potential. In other words, a counter electrode is used to balance the current response

of the working electrode. Many different types of electrochemical tests can be carried out using a potentiostat. Cyclic voltammetry (CV) and electrochemical impedance spectroscopy (EIS) are of most significance to electrode characterization.

In a CV experiment, the current through the working electrode is measured as the voltage is swept over a range in a cyclic manner. A set of CV experiments were performed with scan rates varying from 1 mV/s to 1000 mV/s for the voltage window of -1 V to 0 V with respect to Ag/AgCl reference electrode. The average specific capacitance C (F/g) of the working electrode can be evaluated by using the following equation:

$$C = \frac{I}{m.\nu}$$

where I is the current in amperes, m is active mass of electrode in grams and ν is scan rate in V/s.

EIS is a technique where a small alternating potential is applied for a range of frequency values and the corresponding current is measured. An expression analogous to Ohm's law allow calculation of impedance values-

$$Z(\omega) = \frac{E}{I} = Z_0(\cos\phi + j\sin\phi)$$

where E is the AC voltage of an amplitude of 5 mV, I is the measured AC current, ω is the frequency ranging from 100 kHz to 10 mHz. The impedance is expressed in terms of a magnitude, Z_0 and a phase shift, ϕ.

Two types of impedance that arise from applied potential are resistive impedance and capacitive impedance. If voltage and current are in phase, it signifies a resistive impedance while if they are out of phase by 90° it signifies a capacitive impedance. In EIS measurements, the electrode normally shows a phase difference some angle between 0° and 90°, which

indicates a mixture of resistive-capacitive elements. As the frequency of voltage oscillation is varied, a spectrum evolves from plotting the imaginary impedance with respect to the real impedance, referred as Nyquist plot as shown in Figure 3.4. From a Nyquist plot, one can measure ohmic resistance R_O and charge-transfer resistance $R_{CT.}$ Ohmic resistance is a combined resistance due to electrode, electrolyte, and electrical contacts in the electrochemical cell. Charge transfer resistance for graphene based electrodes represents the intersheet resistance.[142] Another important parameter is RC time constant, indicative of the charging/discharging time of a capacitor. One can calculate the value of RC time constant using the expression –

$$\tau_o = \frac{2\pi}{\omega(\phi = 45°)}$$

where τ_o is RC time constant and ω is frequency when phase shift is 45°.

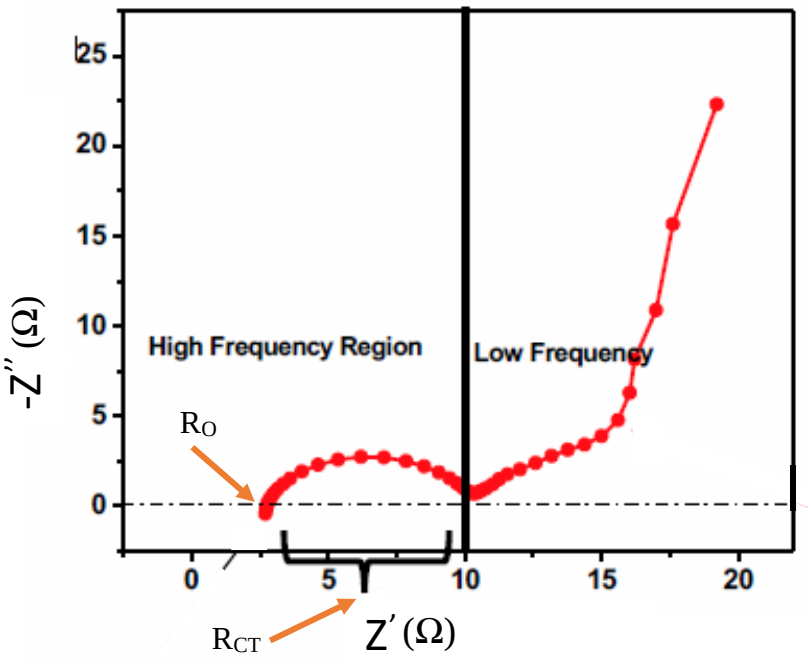

Figure 3.4: Example of a Nyquist plot from EIS data.

3.2.4 Structural Characterization

For SEM imaging and BET measurements of graphene frameworks, the samples were dried using CO_2 critical point dryer. SEM images were taken on a JEOL JSM-7000 field emission microscope. BET measurements were performed on Quantachrome Nova 2200e surface area and pore size analyzer.

3.3 Results and Discussion

3.3.1 Effect of Graphene Oxide Aspect Ratio

Three different graphene frameworks GF, GF+LGF, and LGF were synthesized using 2.5 mg/mL dispersions of (1) small GO, (2) 1:1 small GO and UL-GO, and (3) UL-GO, respectively. Cyclic voltammetry (CV) was performed at various scan rates to measure the capacitance. The rectangular shape of the CV scan in Figure 3.5 (A) confirms the capacitive behavior of all the graphene frameworks with LGF exhibiting the highest capacitance in the group. It should be noted that there is a sharp decline of 85% in capacitance of GF and 74% in GF+LGF as the scan rate is increased from 1 mV/s to 1000 mV/s as shown in Figure 3.5 (B). However, the capacitance decline for LGF is only 66%. This is indicative of a higher degree of diffusion limitation in GF and GF+LGF as compared to LGF. The diffusion limitation can be quantified by measuring the slope (b-value) of a plot between the logarithm of peak current and the logarithm of scan rate from cyclic voltammetry data. It can be considered that peak current (i_p) in CV obeys a power-law relationship with the scan rate (ν) as $i_p = a\nu^b$.[143] For a purely diffusion-limited case, the b-value is 0.5 and for a purely capacitance limited case. it is 1.0. Figure 3.5 (C) clearly shows that b-value for LGF is closest to one, which means the diffusion of electrolyte ions is faster in LGF. This conclusion is further corroborated by ion transport properties, which were probed using electrochemical impedance spectroscopy (EIS) measurements. The frequency response analysis over the frequency range of 0.01 Hz to 100

kHz is shown via Nyquist plots in Figure 3.5 (D). EIS measurements can yield the value of RC time constant (τ_o), which is reciprocal of a characteristic frequency (f_o) where the resistive and capacitive impedances are equal.[144] RC time constant value for LGF is 0.5 seconds, which is three times smaller than GF and two times smaller than GF+LGF as presented in Table 3.2.

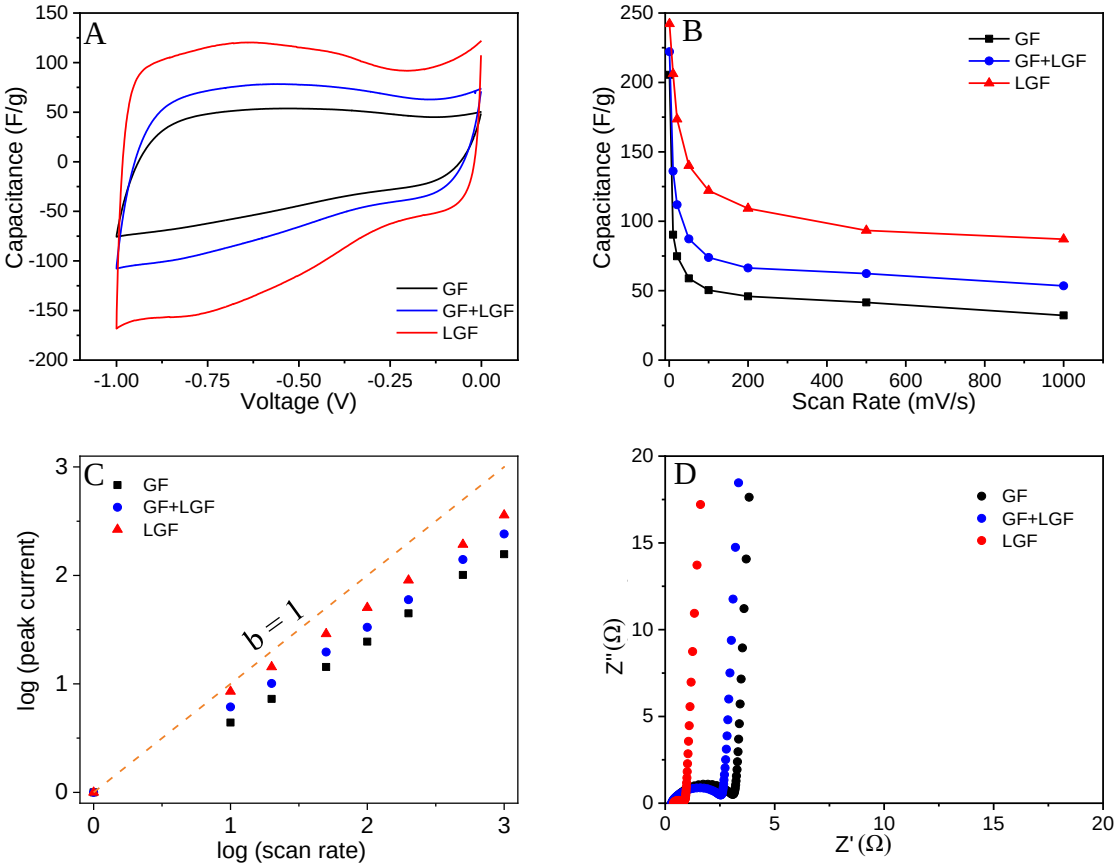

Figure 3.5: Electrochemical characterization of GF, GF+LGF and LGF in three-electrode setup with 6 M KOH electrolyte. (A) CV curves at 100 mV/s, (B) comparison of specific capacitance at various scan rates, (C) b-value determination from CV data, (D) Data points represent an average of three measurements (one measurement each on three samples synthesized from same GO batch).

Table 3.2: Parameters measured from EIS. Parameter values represent an average of three measurements (one measurement each on three samples synthesized from same GO batch) and error represents the maximum and minimum measured values.

Parameters	GF	GF+LGF	LGF
R_O (Ω)	0.33 ± 0.03	0.31 ± 0.03	0.38 ± 0.03
R_{CT} (Ω)	2.8 ± 0.3	2.1 ± 0.2	0.5 ± 0.1
τ_o (s)	1.8 ± 0.2	1.2 ± 0.2	0.5 ± 0.1

The low RC time is indicative of fast charging and discharging time, and therefore signifies faster electrolyte diffusion in LGF electrodes. This means there are more ion transport paths available in LGF as compared to GF and GF+LGF. In the low-frequency regime of the Nyquist plot, the vertical curve suggests ideal capacitive behavior. In the high-frequency regime, a semicircle is featured whose diameter represents the charge transfer resistance R_{CT}. For graphene-based materials, it represents intersheet resistance i.e. activation energy required for electron "interfacial hopping" from one sheet to another. The measured values of charge transfer resistance for GF, GF+LGF, and LGF are 2.8 Ω, 2.1 Ω and 0.5 Ω, respectively. This shows LGF has better electrical percolation than GF and GF+LGF. These R_{CT} values are expected because nanomaterials with high aspect ratios have shown improved electrical percolation previously.[135, 145, 146] R_O, the ohmic resistance due to the material and electrolyte, does not vary significantly for the three samples. LGF not only exhibits better capacitance but also faster ion diffusion and lower charge-transfer resistance, which make it a superior material to be used for electrochemical energy storage applications. Higher capacitance and faster ion diffusion results of LGF are counter-intuitive because the large surface area of UL-GO sheets should lead to higher degree of restacking after reduction resulting from stronger van der Waals attraction.[118] However, if the sheets are so large that they exhibit more corrugations stacking may be retarded.

The higher capacitance can be correlated to Brunauer-Emmerr-Teller (BET) specific surface area measured by nitrogen adsorption-desorption isotherms for CO_2 critical point dried samples of GF, GF+LGF, and LGF. In Figure 3.6 (A), all samples show a typical type IV isotherm as defined by IUPAC, which is characteristic of mesoporous materials.[147] BET SSA measured for GF, GF+LGF and LGF are 698 m^2/g, 773 m^2/g, and 929 m^2/g, respectively. Since the electrode is always soaked in an electrolyte, solvated surface area of GF, GF+LGF and LGF was also measured using a Methylene Blue (MB) adsorption method, which resulted in an area of 414 m^2/g, 440 m^2/g, and 476 m^2/g, respectively. These results demonstrate that LGF exhibits higher capacitance because of its higher available SSA. Efficient ion transport in LGF can be attributed to the higher pore volume of 2.41 cm^3/g that was calculated using the method proposed by Barrett, Joyner, and Halenda (BJH). The GF+LGF and GF pore volume were 2.14 cm^3/g, and 2.03 cm^3/g, respectively. The pore volume results are also supported by low packing density of LGF as evident in Figure 3.6 (B). Further, the optical image of graphene frameworks in Figure 3.6 shows that LGF has the largest volume for the same mass graphene oxide used in synthesis of all three samples. The highly porous structure of GF and LGF can be observed from SEM micrographs in Figure 3.9. LGF shows higher degree of corrugations which seems to prevent the restacking between graphene interlayers and thus contributes to the much higher specific surface area and pore volume. It is known from previous studies that there are corrugations on graphene sheets to maintain thermodynamic stability, which impart interesting properties to the final bulk material.[148-151] In order to have a better understanding of the microstructure of 3D graphene frameworks, a detailed discussion on corrugations of graphene sheets and various interactions among them is presented in the next sub-sections.

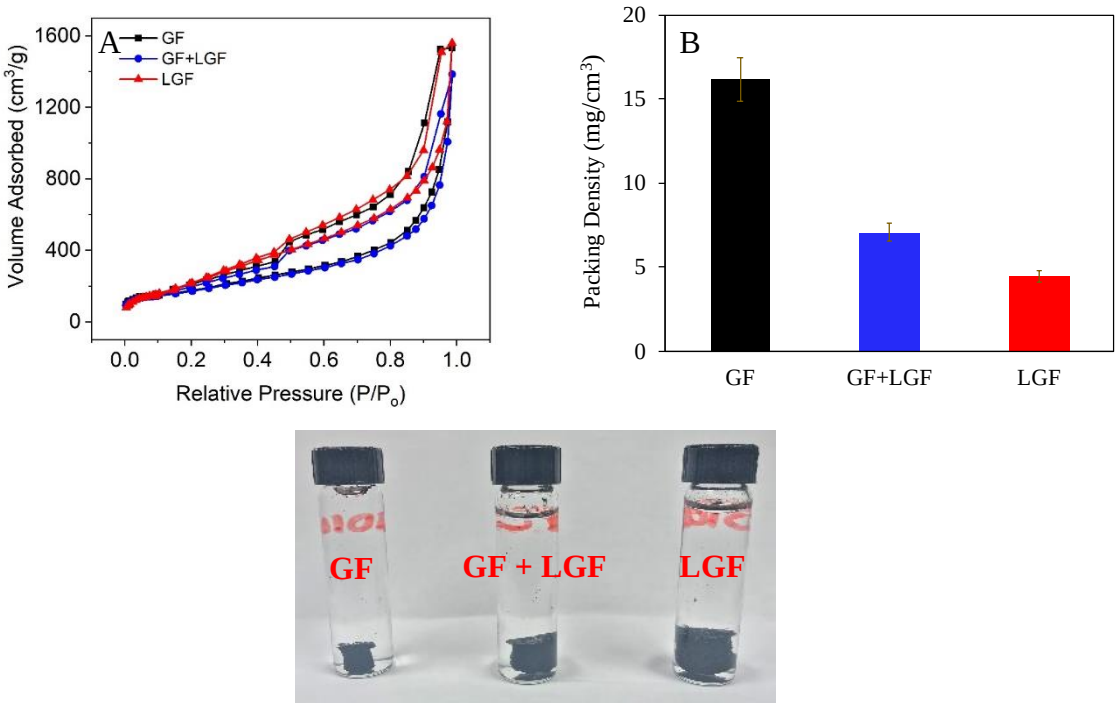

Figure 3.6: (A) N_2 adsorption–desorption isotherms and (B) packing density of GF, GF+LGF and LGF. Image at the bottom is the digital photographs for the visual comparison of the size of different graphene frameworks Data points represent an average of three measurements (one measurement each on three samples synthesized from same GO batch) and error bars represents the maximum and minimum measured values.

3.3.1.1 Ripples, Wrinkles and Crumples in Graphene Sheets

The literature is full of conflicting nomenclature for various corrugations exhibited by graphene sheets. Deng et al. simplified the different corrugations by categorizing them into ripples, wrinkles and crumples based on their aspect ratio, wavelength and topology.[151] The aspect ratio defined here is the ratio of length to the width of corrugation. Ripples are a type of corrugations that are isotropic in nature with valley and peaks having feature size below 10 nm and an aspect ratio close to one. Wrinkles have an aspect ratio of greater than 10 and a height less than 15 nm. Crumples, on the other hand, are dense deformations (folds and wrinkles) occurring isotropically similar to a crumpled paper, where wavelength of corrugations is greater than 100 nm. Table 3.3 provides a description of various corrugations observed on graphene.

Table 3.3: Description of various corrugations on graphene.

Corrugations	Wavelength / Width	Aspect Ratio	Height	Reasons
Ripples	< 10 nm	≈ 1	< 1 nm	Thermal fluctuations
Wrinkles	1 - 100 nm	> 10	< 15 nm	Unidirectional forces arising from interaction with anchoring surface
Crumples	> 100 nm	≈ 1	-	Multidirectional forces

Peierls and Landau, around 90 years ago, demonstrated theoretically that thermal fluctuations destroy long-range order in 2D materials resulting in melting of 2D lattice at finite temperature.[152, 153] In the year 1966, Mermin-Wagner proved that magnetic long range-order cannot exist in 1D and 2D materials.[154] Later, they extended their work to show that crystalline long-range order cannot exist in 2D materials.[155] However, experimental work on thin films and membranes demonstrated that perfect 2D crystal can exist in 3D space.[156-158] The isolation of graphene from graphite,[159, 160] proved the existence of the first truly 2D crystal, and the experimental observation of ripples in suspended graphene by Meyer et al. showed that 2D graphene sheets display long-range order with out-of-plane deformations reaching a height of 1 nm.[161] Experiments described by Meyer et al. demonstrated that freely suspended graphene crystals can exist without a substrate, and exhibit random elastic deformations involving all three dimensions. They reported free-standing graphene sheets with ripples of height 1 nm and wavelength of 5 nm. Fasolino et al. provided strong theoretical support for the experimental observations of ripples in graphene due to thermal fluctuations.[162] To understand the origin of ripples, it is important to note that unlike 2D membranes there exists an interaction between bending and stretching phonons in graphene sheets which cause the temporal and spatial modulations of the C-C bond lengths.[149, 158] In graphene sheets there are no neighboring carbon atoms above or below the sheets which indicate the absence of restoring forces from the adjacent

layers. Hence, bending modes of C-C bonds cause the restoring forces which have an out-of-plane component between neighboring atoms. These perpendicular restoring forces are much weaker than those along the bonds (stretching), and therefore thermal energy at finite temperatures can move the carbon atoms out of the plane creating so-called "ripples".[130] The spatial distribution of the ripples on graphene can be estimated by the equation:[162]

$$L = 4\,\pi\kappa\sqrt{\frac{2\pi}{3TB}}$$

where L is a typical sample size of ripple distribution or distance between two ripples, κ is the bending rigidity, T is the temperature and B is the two-dimensional bulk modulus. This equation shows that number of ripples increases with the temperature and there are no ripples at 0 K. In addition, ripples were shown to significantly reduce the magnitude of in-plane stresses generated by defects.[163] At edges and near defects, the asymmetry of the bond lengths in graphene is amplified causing the increased density of ripples in these regions.

Wrinkles are formed due to the sheets under strain and topology of wrinkles appears similar to the hanging curtains. The strain mainly arises from the interaction with the anchoring surface. These interactions can be amplified because of large temperature changes. Graphene has a negative thermal expansion coefficient i.e. graphene sheet shrinks on heating and expands on cooling. Because metals have a positive thermal coefficient of expansion, graphene grown on metallic catalysts exhibits high densities of wrinkles.[164] An example of graphene wrinkling is shown in Figure 3.7 (B).

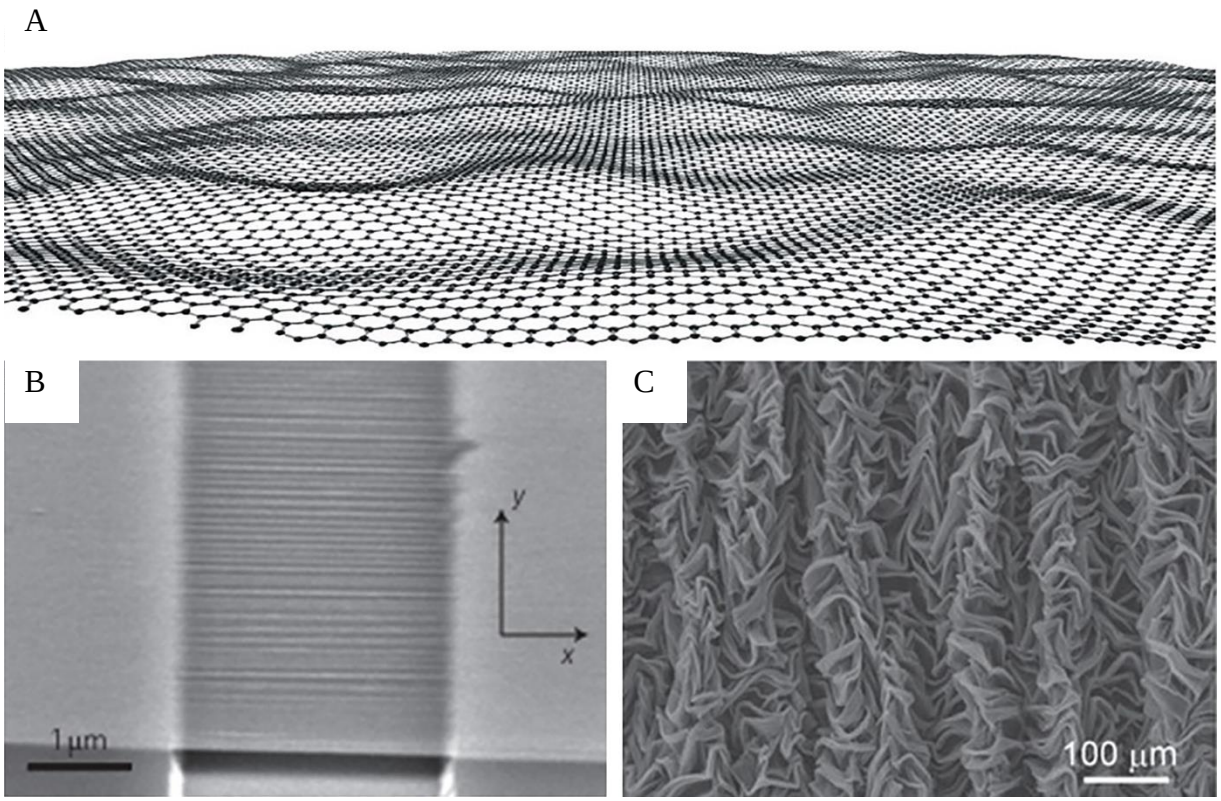

Figure 3.7: Wrinkled, rippled and crumpled graphene. (A) Rippled graphene, (B) wrinkled graphene and (C) crumpled graphene.[150]

Crumple formation is a result of multidirectional forces applied to graphene. Rapid evaporation of GO aerosol droplets has been demonstrated as an efficient way to produced crumpled graphene.[44, 165] This crumpled graphene remains stable by plastically deformed ridges and does not unfold during various types of solution processing or chemical treatments.[166, 167] Luo et al. observed strong graphitic diffraction at the folded ridges during an electron diffraction study and suggested that the folded ridges are held together π–π stacking.[168] In the same study, crumpled graphene was also showed to possess higher free volume and higher accessible surface area as compared to flat graphene sheets.

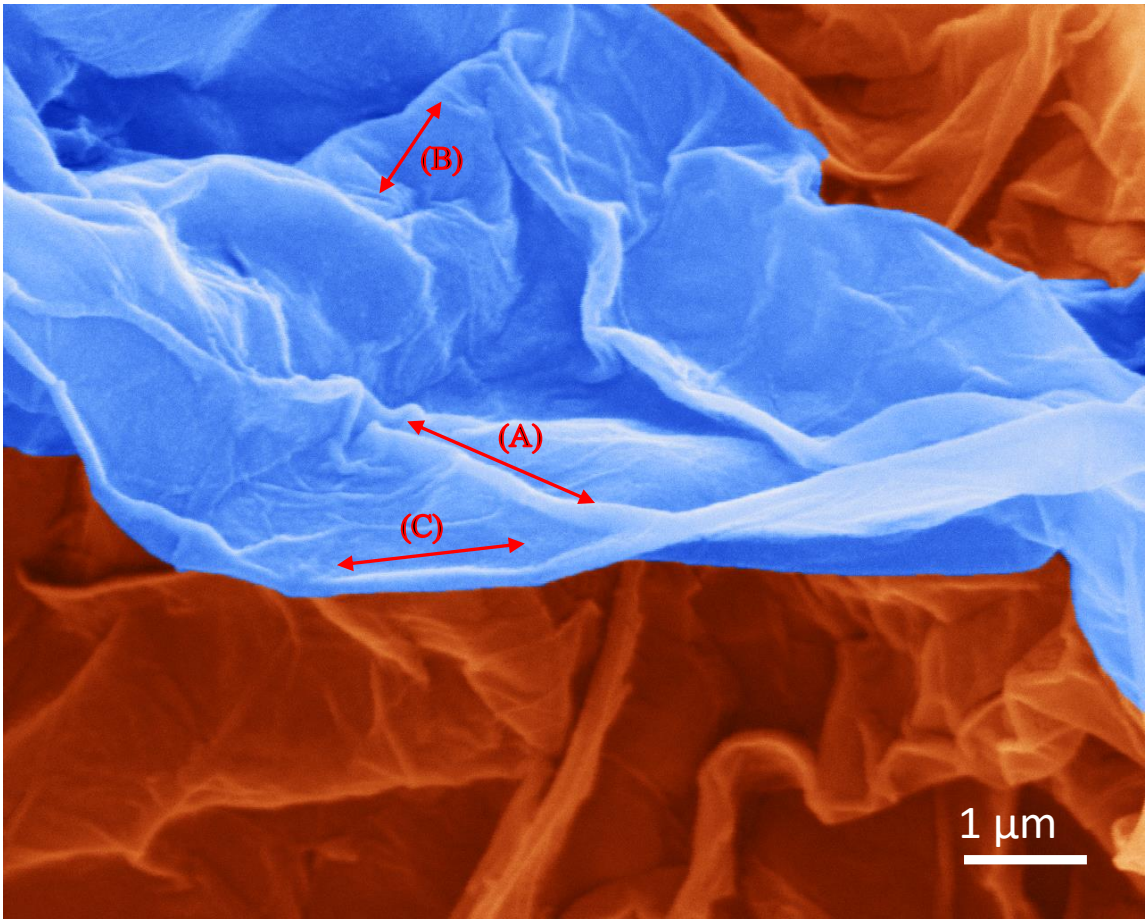

Figure 3.8: SEM image of LGF. Colors were added using Adobe Photoshop to enhance the corrugation features of the sheet in-focus.

Figure 3.8 shows various corrugation features in SEM image of LGF. The corrugation (A) is an example of one of the many wrinkles present in the blue colored individual sheet. One end of the wrinkle (A) meets the folded edge (C) and the other end meets another wrinkle which appears to be present on a crumpled feature. The feature (B) represents one of the crumpled regions of the sheet. It is clear from Figure 3.8 that graphene sheet in LGF has abundant wrinkles and crumples. Figure 3.9 shows the comparison of SEM images of GF and LGF. The microstructure of GF and LGF appears very different from each other. The large sheets are visible in LGF, with abundant wrinkle and crumple features. The wavelength of crumples in LGF is as high as 1 µm as indicated by the red colored arrow shown in Figure 3.9 (D), whereas the size of GO sheets used in GF were less 1 µm. The small graphene sheets observed in GF

have a lesser degree of wrinkling and crumping as compared to LGF. Hence, the findings here support the argument that graphene sheets in LGF have wrinkles and crumples of larger amplitude as compared to graphene sheets in GF and that this could contribute to the improved electrochemical performance.

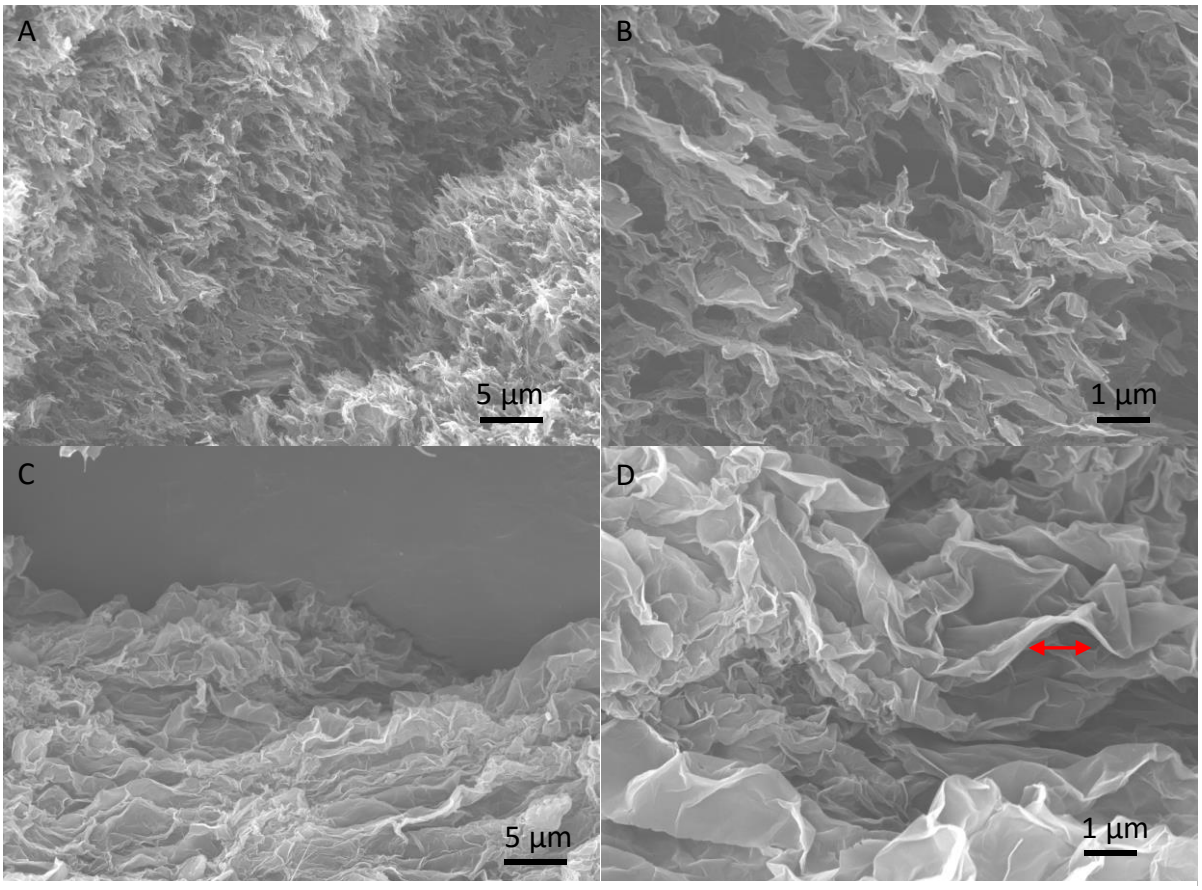

Figure 3.9: SEM images of (A, B) GF and (C, D) LGF.

3.3.1.2 Intermolecular and Surface Forces

It can now be postulated that the larger wrinkles and crumples in the sheets allow the 3D structure to be more porous and avoid complete restacking of the sheets. Superior electrochemical performance of LGF due to high SSA and porosity also support the previous study done by Luo et al., which demonstrated that crumpled graphene has more SSA and pore volume as compared to flat sheets.[168] The previous studies on crumpled graphene referenced here are based on rapid evaporation which causes multidirectional compression forces to

crumple the sheet. The reactions system presented here, however, is much more complex. The conversion of GO dispersion to 3D graphene framework takes place at a moderate pace during a reduction reaction in a hydrothermal reactor at 90 °C. The various multidirectional forces which are in action during the formation of 3DGF are[118] –

(a) π–π interactions – These are attractive non-covalent interactions between aromatic rings containing π bonds. As the reduction reaction progresses, more sp^2 sites on graphene sheets become available which causes the sheets to coalesce.

(b) Hydrophobic interactions – These are strong attractive interactions between hydrophobic molecules in water, often stronger than their attraction in free space. The sp^2 sites on graphene sheets are hydrophobic and tend to coalesce to minimize the surface area exposed to water.

(c) van der Waals attraction – These are long-range dispersion forces where interaction energy becomes stronger with the increase in surface area of nanomaterials. However, these forces are reduced significantly in a solvent medium.

(d) Electrostatic repulsive forces – These are due to negatively charged ionized carboxylic groups at the edges of graphene sheets.

(e) Hydrogen bonding – Oxygen functional groups on graphene sheets form hydrogen bonds with water and other functional groups present on adjacent sheets.

(f) Steric hindrance – The high concentration of GO in the dispersion imparts steric hindrance to the free movement, especially the rotation of individual sheets. Additionally, the oxygen functional groups will also impart steric hindrance and retards the ability of the sheets to come in close enough contact to completely restack due to π–π interactions.

(g) Thermal expansion/compression stresses – The reaction temperature is at 90 °C and the final 3DGF is cooled down to room temperature for further processing, which should cause stresses due to thermal expansion and compression.

These multiple forces during the reaction result in the unique morphology of graphene frameworks as shown in Figure 3.9. Due to the complexity of the self-assembly process, the effect of these forces on the formation of corrugation has been only discussed here qualitatively. Building upon this research, simulation studies could give deeper insight into mechanism of self-assembly and microstructure of graphene frameworks in future.

Another factor that influences the microstructure of 3DGF is the number of GO sheets in the dispersions. For GO dispersions of the same concentration but different GO sheet size, the relationship below must be true, assuming similar intersheet spacing:

$$n_1 A_1 \approx n_2 A_2$$

where A is the average sheet area and *n* is the total number of sheets in a dispersion. Since UL-GO has higher average sheet area, the number of sheets in the UL-GO dispersion will be fewer. From previous studies, it is known that the number of contacts per sheet are limited by the energy required for intersheet deformation.[150] Also, the higher amplitude of wrinkles and crumples in the UL-GO sheets require higher energy for their deformations. This results in fewer intersheet contacts in LGF resulting in higher SSA and porosity leading to higher capacitance and efficient ion transport. LGF has fewer sheets and fewer intersheet contacts which minimizes the "electron hopping" resulting in better electronic percolation and low values of charge transfer resistance of LGF. It is also important to note that LGF was relatively firm and strong as compared to the GF and GF+LGF. This was observed while cutting the graphene frameworks using a blade into thin pieces to be pressed upon the Ni foam. Further

mechanical experiments such as dynamic mechanical analysis (DMA) should be performed to compare the strength of these materials quantitatively.

The results of the GO sheet aspect ratio study suggest that overall LGF is a superior material given its superior electrochemical properties. The results of GF+LGF indicates that addition of small GO to UL-GO will deteriorate the properties of the graphene framework. These results agree with other studies where UL-GO has shown to be a better precursor for RGO based materials having better mechanical properties and higher conductivities.[135, 137, 148]

3.3.2 Effect of Concentration

3D self-assembled graphene frameworks were prepared using small GO with the concentrations from 2.0 mg/mL to 12 mg/mL and UL-GO with concentration from 0.5 mg/mL to 4.0 mg/mL. The electrochemical characterization results for GF and LGF are shown in Figure 3.10 and Figure 3.11, respectively.

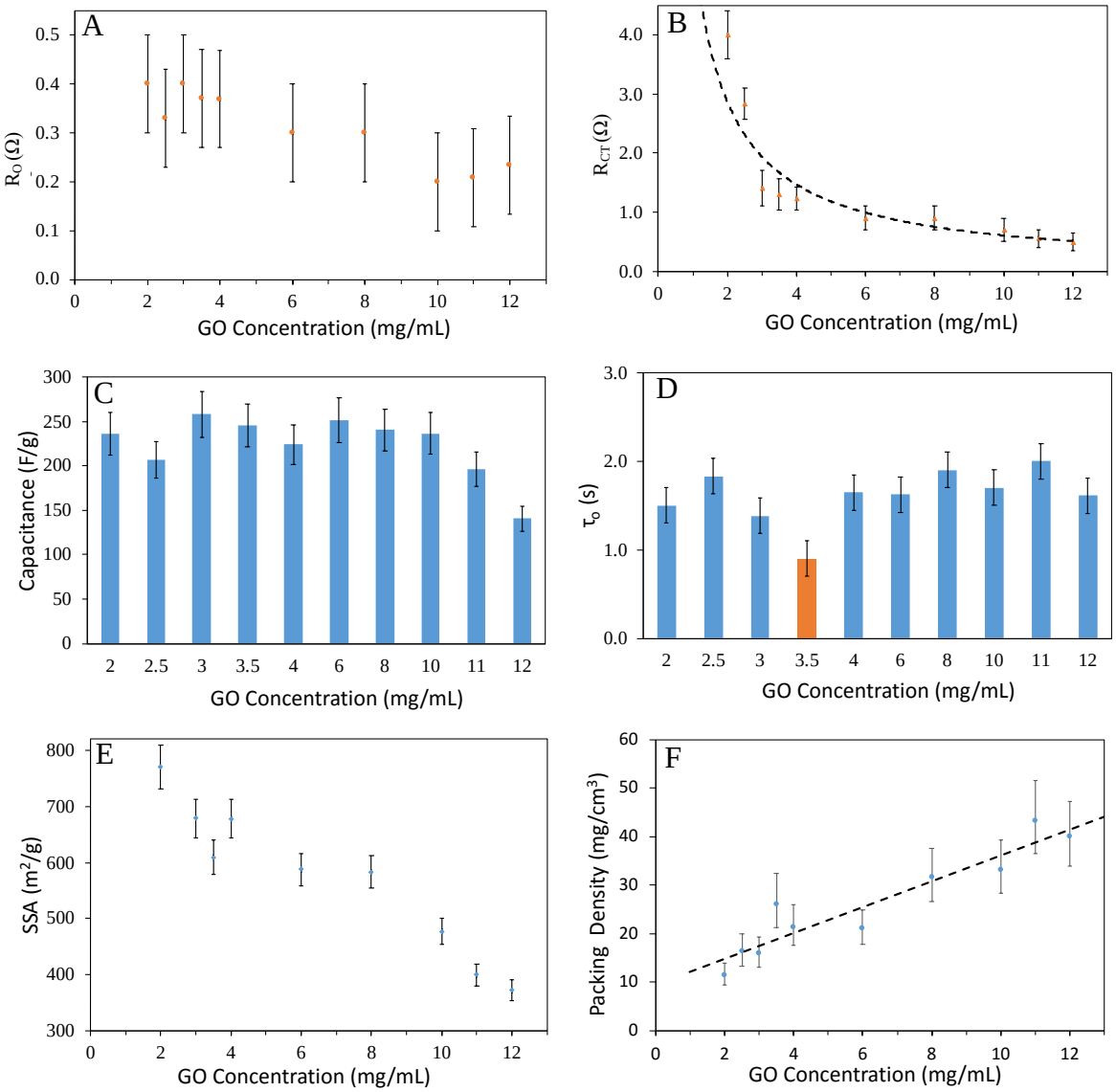

Figure 3.10: Characterization results of GFs formed using GO dispersion of concentrations 2.0 mg/mL to 12 mg/mL. Electrochemical properties measured from EIS (A) Charge-transfer resistance, (B) Equivalent Series Resistance, and (C) RC time constant. (D) Capacitance measured from cyclic voltammetry at a scan rate of 1 mV/s. (E) Packing density calculated by manually measuring the dimensions of graphene frameworks. (F) BET SSA of GFs. Data points represent an average of three measurements (one measurement each on three samples synthesized from same GO batch) and error bars represents the maximum and minimum measured values.

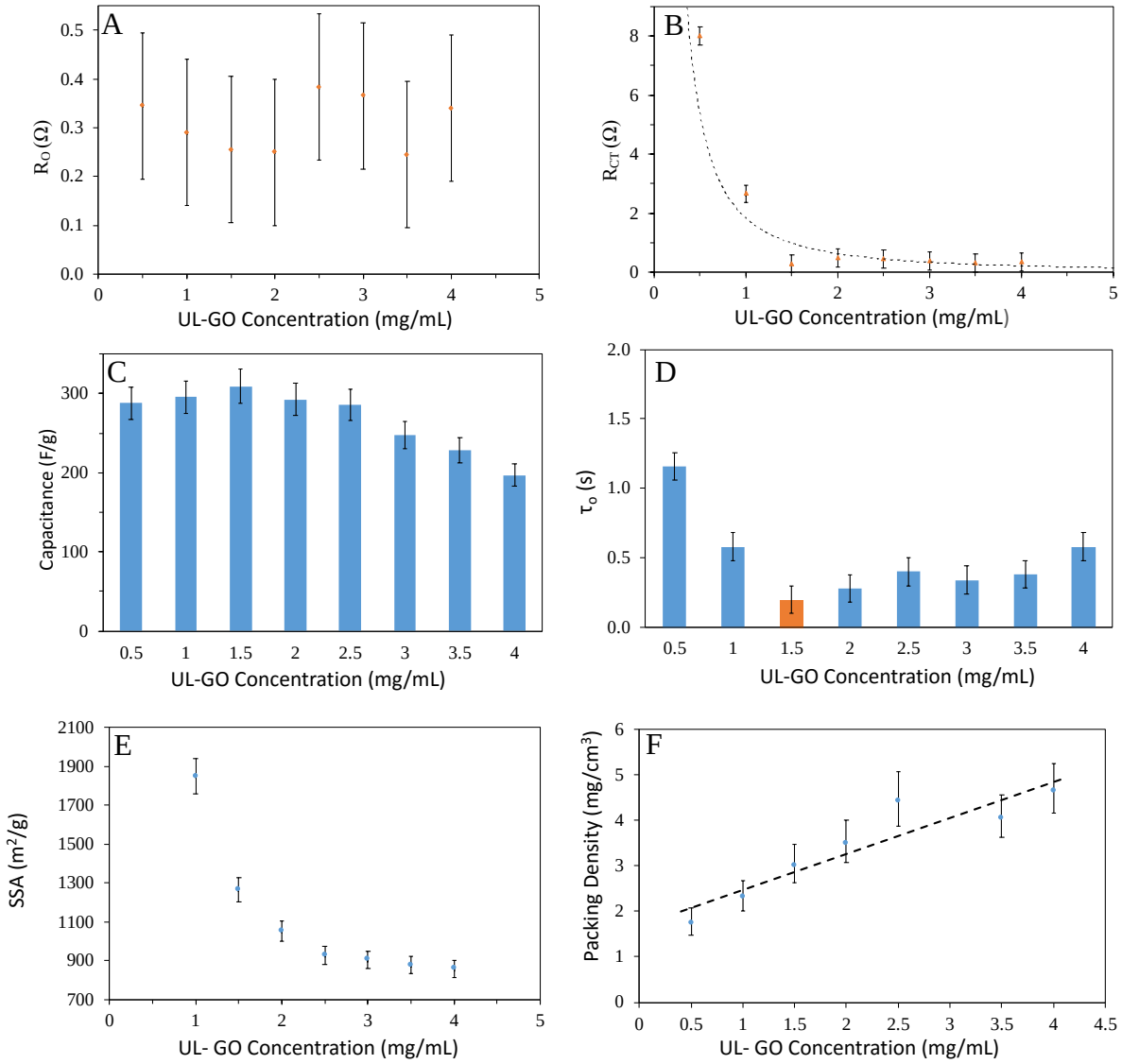

Figure 3.11: Characterization results of LGF formed using UL-GO dispersion of concentrations 0.5 mg/mL to 4.0 mg/mL. Electrochemical properties measured from EIS (A) Charge-transfer resistance, (B) Equivalent Series Resistance, and (C) RC time constant. (D) Capacitance measured from cyclic voltammetry at a scan rate of 1 mV/s. (E) Packing density calculated by manually measuring the dimensions of graphene frameworks. (F) BET SSA for LGF. Data points represent an average of three measurements (one measurement each on three samples synthesized from same GO batch) and error bars represents the maximum and minimum measured values.

For GF, the variation in ohmic resistance R_O is very insignificant and its values lie between 0.2 Ω to 0.4 Ω as shown in Figure 3.10 (A). However, R_{CT}, charge-transfer resistance decreases sharply in Figure 3.10 (B) as the concentration is increased from 2.0 mg/mL to 3.5 mg/mL beyond which it decreases very gradually. This means GF formed with high concentration GO has a highly interconnected structure with abundant percolating pathways between sp^2 clusters. These results agree with the electrical percolation theory which suggests that beyond a certain threshold concentration, electrical conductivity is increased sharply followed by saturation and below the percolation threshold the electrical conductivity is zero.[169]. The lowest initial dispersion concentration used in this study was 2.0 mg/mL because GF was not formed below this concentration. This threshold concentration of GO for the formation of 3D graphene framework was also found in previous work by Xu et al.[106] Hence, 2.0 mg/mL is the critical concentration of small GO to form a stable GF and also represents the critical percolation concentration above which conductivity increases sharply and then becomes relatively constant.

For the dispersion concentrations studied, the RC time constant was lowest for the GF synthesized from the GO dispersion of concentration 3.5 mg/mL as shown in Figure 3.10 (D). The RC time constant value increases with concentration after 3.5 mg/mL. This indicates that ion transport becomes inefficient as the concentration is increased. This can be correlated to the increase in packing density of the graphene frameworks with concentration as shown in Figure 3.10 (E). Increase in the packing density will reduce the porosity of the graphene framework and hence the ion transport will become inefficient. At concentration lower than 3.5 mg/mL, the charge transfer resistance is high. This will cause a large potential drop and subsequently a

weak electric field. Hence, sluggish transport of ions takes place leading to the low RC constant below 3.5 mg/mL.

The capacitance values remain between 200 F/g to 250 F/g for GF synthesized from 2.0 mg/mL to 10 mg/mL beyond which it decreases substantially below 200 F/g as shown in Figure 3.10 (C). The low capacitance at higher concentration can be attributed to the low SSA as shown in Figure 3.7 (F). However, the capacitance does not follow the SSA trend for the majority range of concentration. Especially at low concentration, even though the SSA was higher, the capacitance was not high. The surface area of GF at lower concentrations might not have been available to the ions because of the weak electric field caused by high charge-transfer resistance. At higher concentrations, the charge-transfer resistance is low and saturated but the drop in SSA is drastic which results in low capacitance values.

For LGF, the variation in R_O shown in Figure 3.11 (A) is very insignificant and follows no particular trend. The charge-transfer resistance decreases sharply in Figure 3.11 (B) as the concentration is increased from 0.5 mg/mL to 1.5 mg/mL beyond which it saturates. These results are similar to the ones for smaller sheets discussed in previous paragraphs and can also be related to electrical percolation theory.[169] UL-GO concentration of 0.5 mg/mL can be considered as the critical concentration for the formation of graphene frameworks and also the percolation threshold, below which GO reduction induced self-assembly is not possible. The minimum charge-transfer resistance exhibited by 1.5 mg/mL LGF (0.28 Ω) is four times lower than charge transfer resistance shown by 3.5 mg/mL GF (1.2 Ω) indicating again that UL-GO imparts superior properties to the graphene frameworks.

The RC time constant trend of LGF is also similar to GF. The minimum value of RC time constant is for the LGF synthesized from the UL-GO dispersion of concentration 1.5

mg/mL as shown in Figure 3.8 (C). The RC time constant value increases at concentration below and above 1.5 mg/mL. This indicates that ion transport becomes inefficient as the concentration is increased which is thought to result from the increase in packing density of the LGF with concentration of UL-GO as shown in Figure 3.8 (E). However, the high value of RC constant at concentration lower than 1.5 mg/mL can be attributed to sluggish transport because of high charge transfer resistance as explained in the discussion of the GF results. The minimum RC time constant displayed by LGF is 0.2 seconds as compared to 0.9 seconds for GF which indicates that ion transport is more efficient in LGF.

The capacitance values are consistently close to 300 F/g for LGF synthesized from 0.5 mg/mL to 2.5 mg/mL beyond which it decreases substantially. Similar to GF, the lower values of capacitance at higher concentrations can be attributed to the low SSA as shown in Figure 3.8 (F). However, the capacitance does not follow the SSA trend for the majority range of concentration. This means even though the SSA was higher at smaller concentration, all the area might not have been available to the ions because of blocked pores and high charge-transfer resistance. The optimum concentration at which the LGF exhibits superior electrochemical properties is 1.5 mg/mL.

3.3.3 pH effect on Graphene Frameworks

Graphene frameworks were synthesized with 1.35 mg/mL UL-GO dispersions of pH 3 and pH 10. During the reaction, it was observed that pH 10 dispersion self-assembled faster in comparison to the pH 3. Both the samples were also tested for electrochemical performance as shown in Figure 3.12. Cyclic voltammogram shows that pH 10 LGF shows slightly improved capacitance as shown in Figure 3.12 (A). The results from EIS in Figure 3.12 (B) shows that pH 10 LGF has lower charge transfer resistance and lower RC time constant. These are interesting results given that at higher pH the dispersion is more stable. The carboxylic groups of GO ionize to a higher degree at pH 10 as compared to pH 3. The electrochemical results in this pH study are not significantly different as compared to the concentration and sized study. At this point, the variation in electrochemical performance due to change in pH is not understood. Nevertheless, these are interesting results which give the direction of future research.

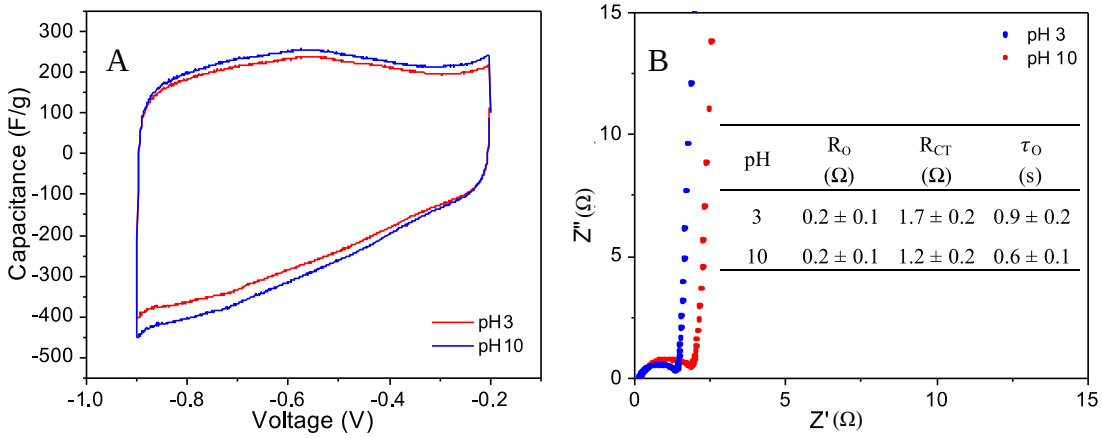

Figure 3.12: (A) Cyclic voltammogram at scan rate of 10 mV/s and (B) Nyquist plot of LGF formed by UL-GO of pH 3 and pH 10. Data points represent an average of three measurements (one measurement each on three samples synthesized from same GO batch) and error bars represents the maximum and minimum measured values.

3.4 Conclusions

Self-assembled 3D graphene frameworks were constructed using a dispersion of small GO and UL-GO. LGF, graphene frameworks synthesized from UL-GO, exhibited the highest SSA and porosity leading to the highest capacitance and most efficient ion transport evidence by small RC constant value. LGF also showed the lowest charge-transfer resistance due to improved electrical percolation because of high aspect ratio as also evidenced other studies. The concentration dependence was also explored, and it was found that the optimum concentration of GF and LGF are 3.5 mg/mL and 1.5 mg/mL, respectively. At these concentrations, these graphene frameworks exhibited the lowest RC time constant, lowest charge transfer resistance and highest capacitance. It can also be concluded that the optimum concentration value decreases as the aspect ratio of GO sheets is increased. The achievement of superior electrochemical properties in 3D graphene frameworks with ultra-large graphene sheets suggests that there are many opportunities where a fundamental understanding of assembling 2D nanomaterials can lead to desirable properties in bulk 3D materials. Studies like this which explore structure-processing-property relationships will be the key to unlock the real potential of the graphene-based nanomaterials.

Chapter 4

Microwave-Assisted Production of Holey Graphene

4.1 Introduction

Among various materials studied for energy storage applications, carbons are very attractive to scientists because of their low cost, high SSA, high strength-to-weight ratio and their capability to bond with various atoms via different hybrid orbitals.[40, 109] These characteristics make carbon very versatile for making porous structures with diverse morphology and interesting properties. Graphene has recently gained popularity as a basic building block to manufacture porous structures for energy storage.[29, 50, 56, 62, 113, 170, 171] Such structures retain the remarkable physical properties of the graphene by avoiding the restacking of sheets. The 2D sheet-like structure of graphene imparts a very high SSA and a high gravimetric capacitance while the conjugated sp^2 network of carbon-carbon bonding gives rise to a conducting π band of $2p_z$ electrons which are responsible for phenomenal electron mobility.[56, 172-174]

Bulk production of graphene through a cheap, safe and non-toxic process is challenging. Therefore, researchers commonly utilize reduced graphene oxide (RGO) as a substitute for graphene for various energy storage applications.[23-27] Due to the van der Waals attraction between the individual RGO sheets, they tend to stack together while fabricating electrodes, which decreases the SSA resulting in poor performance of energy storage devices.[28-32] Hence, considerable focus is placed in developing unique morphologies from RGO to avoid stacking of sheets. One of the interesting morphologies is holey graphene.[47, 106, 107] Holes in graphene sheets not only provide additional channels for fast electrolyte ion diffusion in electrode material but also solve the problem of restacking of graphene sheets. As discussed

previously, carboxylic functional groups are populated in large density at the edges for graphene oxide sheets.[20, 175] This results in aqueous GO dispersions having a negative zeta potential due to carboxylic acid ionization.[21] Holes in graphene sheets increase the number of edge-plane carbons, which in turn increases the carboxylic groups. Carboxylic groups are difficult to remove during the reduction process as previously described their presence impedes sheet restacking via electrostatic repulsion and steric hindrance.[98]

Various methods are reported in the literature to synthesize porous graphene. Thermal exfoliation is a common method to create porous graphene from GO that has been demonstrated multiple times.[45, 46, 48] Recently, Kim et al. demonstrated fabrication of three dimensional porous graphene with hierarchical pore structure using KOH activation.[44] Radich et al. in 2014 prepared holey graphene using UV photolysis of H_2O_2 to attack RGO with OH●.[5] Zhao et al. manufactured flexible holey graphene paper electrodes sonicating GO solution with nitric acid to make pores.[49] Fan et al. synthesized porous graphene sheets by mixing GO with $KMnO_4$ and irradiating with microwaves.[50] Apart from solution-based methods, researchers have manufactured interesting graphene morphologies from lithographic techniques as well.[52-55]

Most of the methods described above utilize harmful acids or use high temperature and high-pressure processes, which are unsafe and in turn become expensive methods. Remaining methods such as lithographic techniques have a very low yield and require expensive infrastructure. The synthesis method proposed by Radich et al. is a simple method which requires inexpensive infrastructure.[5] They employed gold nanoparticles (AuNPs) as a catalyst to generate OH● with UV light and oxidized RGO via hydroxyl radical attack. The oxidation of RGO was marked by pores and wrinkles within the graphene sheets. Their results highlighted the use of the AuNP-mediated oxidation reaction to tune the properties of RGO through the

degree of oxidation. However, utilizing UV light for the production of holey graphene is a slow process and requires very dilute solutions of GO. In this chapter, a solution-based method where microwave photolysis of H_2O_2 to produce OH● and attack RGO to produce holey graphene is demonstrated.

Hydrogen peroxide is one of the most powerful oxidizers. For the same reason, its use has been studied for years in wastewater treatment.[176-178] Chapter 1 discussed examples from the literature where H_2O_2 is utilized for oxidative etching of carbon atoms from graphene oxide basal plane to make holey graphene. The by-products from this reaction are water and carbon dioxide, which does not contaminate the graphene oxide solution. Other common oxidants like chlorine (Cl_2), chlorine dioxide (ClO_2) or permanganate (MnO_4) results in unwanted species in the solution and hence are avoided. Moreover, the standard redox potential of H_2O_2 is greater than above-mentioned oxidants which makes H_2O_2 stronger oxidant as shown in Table 4.1. By using UV photolysis, H_2O_2 can be converted into OH● radicals (with an oxidation potential of 2.8 V) that are much more reactive than H_2O_2 and O_3.

Table 4.1: Oxidation potential of common species.[178]

Species	Oxidation Potential (V)
Fluorine	3.03
Hydroxyl radical	2.80
Atomic oxygen	2.42
Ozone	2.07
Hydrogen Peroxide	1.78
Perhydroxyl radical	1.70
Permanganate	1.68
Hypobromous Acid	1.59
Chlorine dioxide	1.57
Hypochlorous acid	1.49
Chlorine	1.36

The application of microwaves (MWs) to hydrogen peroxide has been studied as an advanced oxidation process for sewage sludge treatment.[179, 180] This method has been demonstrated to be very energy efficient and effective. The kinetics and degree of oxidation reaction are dependent on the H_2O_2 concentration, MW time and MW power. Studies also suggest that MWs catalyze the production of OH● radicals from H_2O_2.[177] However, there are no direct measurements available to prove the production of OH● radicals from H_2O_2 on the application of MWs. In this chapter, the production of OH● radical via MW irradiation of H_2O_2 is demonstrated. Additionally, a new method to produce holey graphene by irradiating a solution of RGO and H_2O_2 with microwave (MW) is proposed.

4.2 Experimental

4.2.1 GO and RGO Synthesis

GO was synthesized using a modified Hummers method.[5] 2 g of graphite powder (Alfa Aesar, 325 mesh) and 2 g of $NaNO_3$ (Alfa Aesar, 99%) in 92 mL of concentrated H_2SO_4 (Amresco) was sonicated and stirred in an ice bath with for 30 minutes. After this, 12 g of $KMnO_4$ (Alfa Aesar, 99%) was very slowly added while carefully monitoring the temperature, not allowing it to go above 20 °C. Sonication was continued for 30 minutes following the addition of $KMnO_4$, after which the mixture was allowed to stir slowly overnight at 30 °C. Next, 100 mL of deionized (DI) H_2O was added dropwise followed by 1 hour of stirring. Finally, 600 mL of H_2O_2 (EMD Milipore, 30% w/w) diluted to 3% w/w was added into the flask, yielding a yellowish-brown GO suspension. The suspension was washed three times with concentrated 1 M HCl (BDH) via centrifuge, and finally five times with DI H_2O. To synthesize RGO, GO was diluted to 0.066 mg/mL 10 mM $NaBH_4$ (J.T. Baker, 98%) was added to the dispersion and heated overnight at 90 °C while stirring.

4.2.2 ORGO Synthesis

15 mL of RGO (0.066 mg/mL) RGO was mixed with 3 mL H_2O_2 (EMD Milipore, 30% w/w) diluted to 3% w/w and irradiated in a 1200 W commercial microwave (Panasonic NE-12523) with full power for 30 minutes. During the reaction, the microwave was turned off every 2.5 minutes to add water in the reactants mixture to compensate for the water lost due to evaporation. To demonstrate the scalability of this process, the same experiment was done successfully with 10 times the concentration of RGO and of H_2O_2. UV spectra were taken at regular intervals with an Agilent Cary 60 UV-Vis Spectrophotometer.

4.2.3 Fluorescence Spectroscopy

3 mL of a mixture of 0.2 M TA (Alfa Aesar, 98%) and 1 M NaOH (Amresco) solution was mixed with varying amount of H_2O_2 (EMD Milipore, 30% w/w) – 0, 50 and 100 µL. These three samples were irradiated in 1200 W commercial microwave (Panasonic NE-12523) for 60 seconds. Samples were excited at $\lambda = 330$ nm to obtain fluorescence spectra on SpectraMax i3, Molecular Devices. Another set of three samples were created with 3 mL of a mixture of 0.2 M TA (Alfa Aesar, 98%), 1 M NaOH (Amresco) solution and 100 µL of H_2O_2 (EMD Milipore, 30% w/w). These three samples were irradiated for different times in the MW – 0, 30 and 60 seconds. Samples were excited at $\lambda = 330$ nm to obtain fluorescence spectra on SpectraMax i3, Molecular Devices.

4.2.4 Characterization

XPS data was obtained on a Kratos Ultra DLD instrument using a monochromatic Al Kα X-ray source (1486.6 eV). FTIR spectroscopy was performed with attenuated total reflection (ATR) method using Thermo Scientific Nicolet 6700 FT-IR spectrophotometer. TEM images were taken on Zeiss EM10 Transmission EM. Raman Spectroscopy was performed on inVia Qontor Renishaw Microscope using a 532 nm laser light.

4.3 Results and Discussion

4.3.1 Microwave-Assisted Production of Hydroxyl Radical

Production of OH● on MW irradiation of H_2O_2 (Reaction Scheme 1) was validated by monitoring the conversion of terephthalic acid (TA) into 2-hydroxyterphthalic acid (TAOH) during MW irradiation of TA + H_2O_2 solution. TA in aqueous solution can react irreversibly with OH● to form fluorescent TAOH (Reaction Scheme 2) which exhibits strong fluorescence at 426 nm under UV excitation. This method has been used in the past to monitor hydroxyl radical detection in photochemical and photocatalytic experiments.[181-183]

Reaction Scheme 1

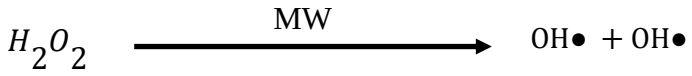

Reaction Scheme 2

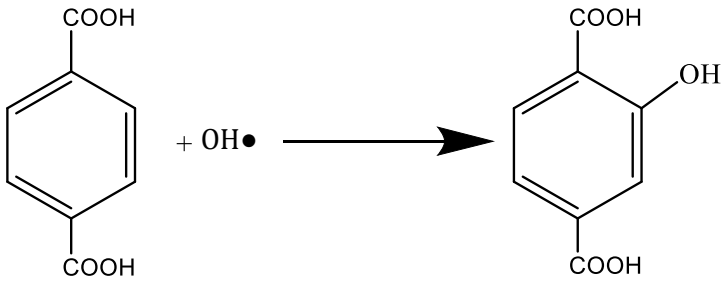

Figure 4.1 shows the fluorescence spectroscopy results. Figure 4.1 (A) shows that fluorescence intensity increases as the concentration of H_2O_2 increases. Figure 4.1 (B) shows that fluorescence intensity increases as the time of MW irradiation increases. This demonstrates that OH● radical is produced during MW irradiation of H_2O_2 and OH● yield can be improved by increasing the time of MW irradiation. These experiments were repeated three times and they showed the similar trends. The OH● radicals produced using MW irradiation of H_2O_2 were utilized to synthesize holey graphene.

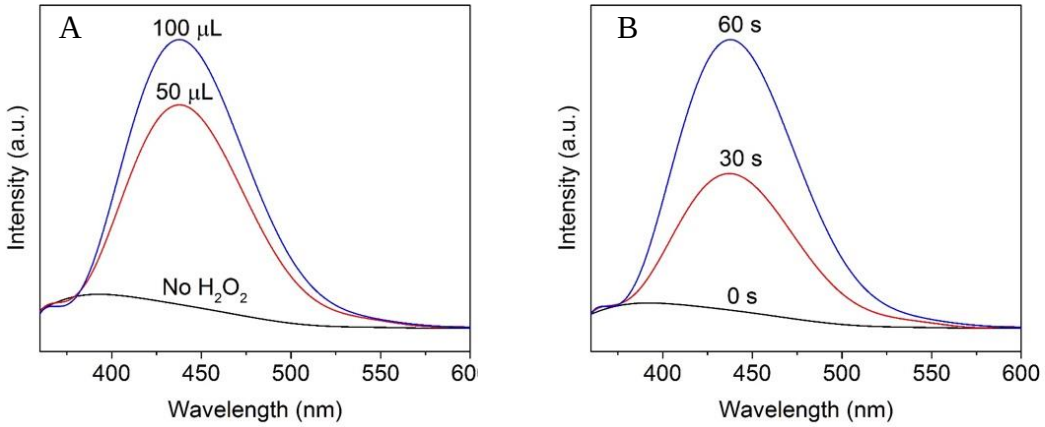

Figure 4.1: (A) Fluorescence intensity of TA with increasing H_2O_2 concentration irradiated with microwaves for 60 seconds, (B) Fluorescence intensity of mixture of TA and 100 µL of H_2O_2 irradiated with microwaves for different durations.

4.3.2 Oxidative Etching of Carbon Atoms

First, a graphene oxide dispersion is reduced to RGO using sodium borohydride ($NaBH_4$), which is a mild reducing agent. In the reduction step, (1) oxygen functional groups are removed, (2) carbon hybridization changes from sp^3 to sp^2 and (3) the color of the dispersion changes from light brown to dark brownish/black as shown in Figure 4.2, which means that the absorption of light increases for RGO as compared to GO. Figure 4.3 (D) shows the UV-Visible spectrum of a GO dispersion at different times during its chemical reduction. The absorption of light increases as the reduction time increases signifying the formation of RGO.

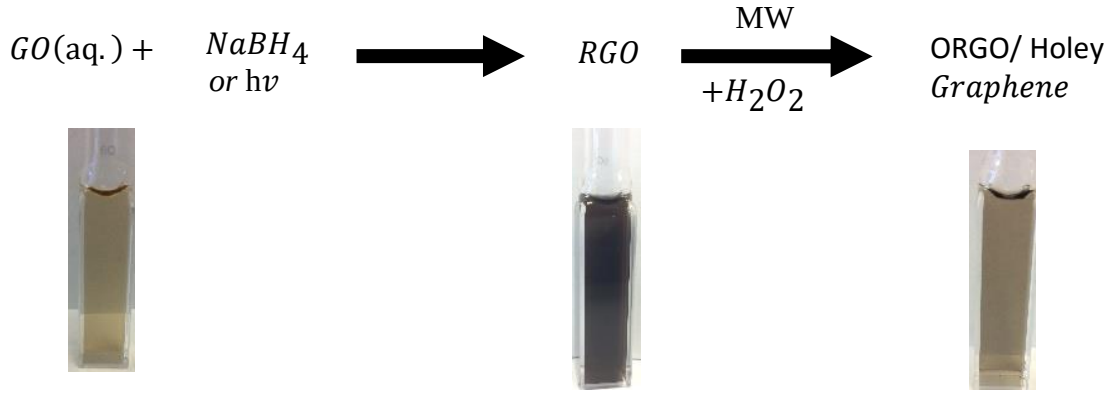

Figure 4.2: Schematic showing the conversion of GO to ORGO. Digital pictures of samples of GO, RGO and ORGO.

Then, RGO was mixed with H_2O_2 and irradiated with MW for 30 minutes. To demonstrate the scalability of this process, the same experiment was done successfully with 10 times higher concentration of RGO and of H_2O_2. The UV visible spectra were taken after every 5 minutes of MW irradiation as shown in Figure 4.3 (A) for RGO concentration of 0.066 mg/mL and Figure 4.3 (B) for RGO concentration of 0.66 mg/mL. The absorption spectra decrease in both cases. It is also evident from the bottom right picture in Figure 4.2, where the color of dispersion becomes light brown. It takes 80 minutes of MW irradiation for higher concentration RGO to accomplish the same degree of reaction accomplished by dilute RGO in 30 minutes. This implies that the significant fraction of MW is absorbed by concentrated RGO. This parasitic absorption of MW radiations by RGO decreases the rate of OH● production from H_2O_2 from and in turn, reduce the rate of reaction for higher concentration RGO.

The light brown color of the final dispersion after H_2O_2 reaction indicates that the new product formed is chemically similar to GO where carbon hybridization has been changed to sp^3. Radich et al. in 2014 proposed a similar method where they utilized H_2O_2 for oxidative etching of carbon atoms from RGO basal plane to make holey graphene.[5] They demonstrated that AuNP catalyzed the UV photolysis of H_2O_2 and mediated the OH● attack on RGO which resulted in holey graphene also referred to oxidized RGO (ORGO).[5]

In a control experiment, H_2O_2 was not added to the RGO and the solution was irradiated with MW for 30 minutes. Figure 4.3 (C) shows the UV-Visible absorption spectra of RGO solution at different times of MW irradiation. The absorption increases with the MW irradiation time indicating that the RGO is further getting reduced to a higher degree. Hence, it can be concluded that MW treatment of RGO and H_2O_2 results in two competing reactions – (1) the thermal reduction of oxygen functional groups on RGO sheets, and (2) oxidation of RGO due

to OH● attack. The decreases in the UV-Vis absorption spectra in Figure 4.3 (A) and Figure 4.3 (B) suggests that oxidation reactions supersede the reduction reaction. These experiments were repeated five times and they showed the similar trends.

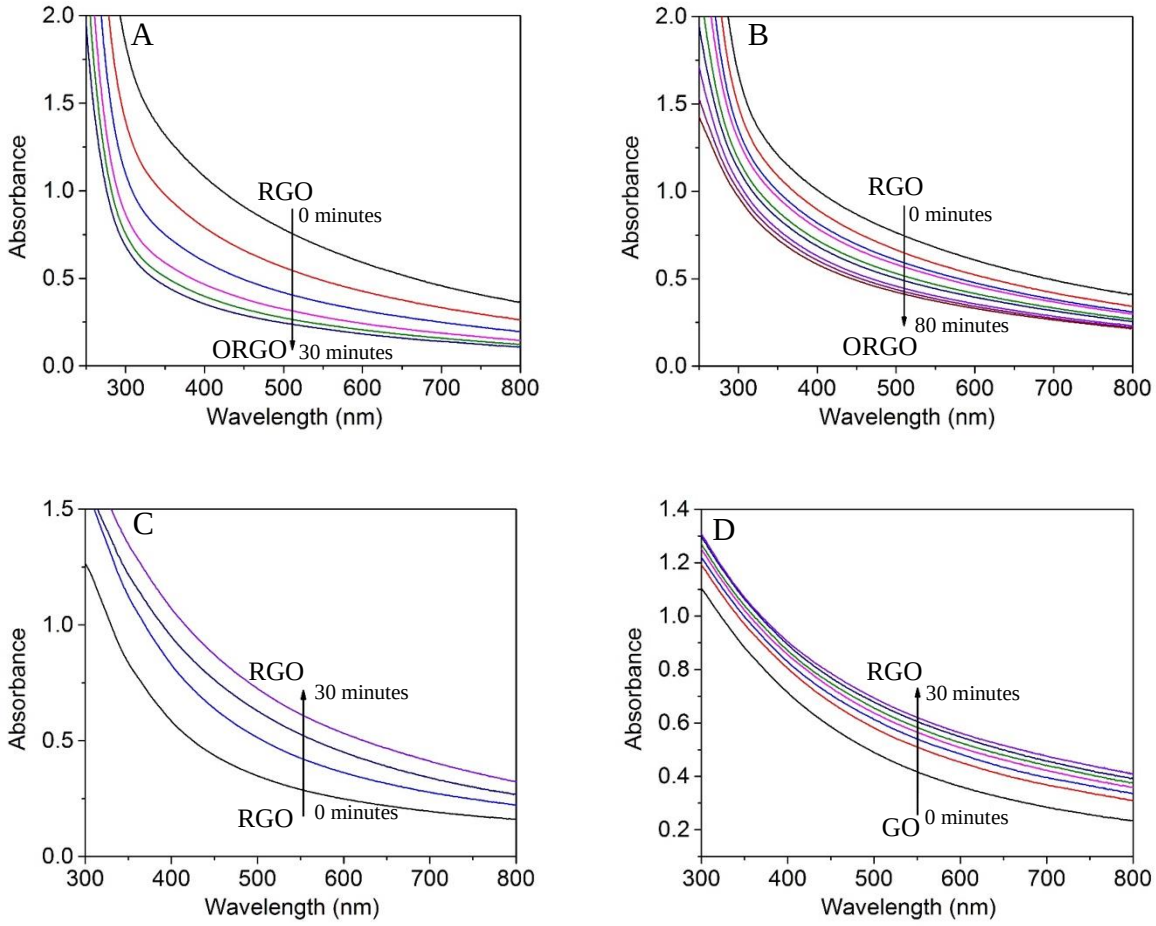

Figure 4.3: UV-Visible spectra of (A) RGO + H_2O_2 irradiated with MW for 30 minutes, (B) RGO + H_2O_2 (scaled up 10 times) irradiated with MW for 80 minutes, (C) RGO irradiated with MW for 30 minutes and (D) GO irradiated with UV for 30 minutes.

X-ray photoelectron microscopy (XPS) and FTIR spectroscopy were performed to understand the effect of GO reduction and subsequent oxidation on the functional groups and to further provide evidence for the proposed mechanism of OH● radical attack. Figure 4.4 (A), (B), and (C) show the C_{1S} peak for GO, RGO, and ORGO, respectively. These peaks were de-convoluted into three peaks arising from C-OH (hydroxyl, 286.5 eV) and C=O (carbonyl, 288.5eV) and C-C/C=C (sp^2 and sp^3 carbon, 284.8 eV). The relative peak areas can give

information about the ratio of one species to another. The C-OH peak is highest for GO representing abundant hydroxyl functional groups on the basal plane. The ratio of area under C-C, C=C peaks to that of C=O and C-OH is 0.58 for GO and it increases to 2.42 for RGO. The ratio increases for RGO because the C-OH peak height drops drastically, which indicates the removal of hydroxyl functional groups and recovery of sp^2 hybridized carbon. Finally, C-OH peak recovers slightly for ORGO suggesting that a fraction of carbon atoms acquired an OH adduct which means that RGO was partially oxidized on MW irradiation with H_2O_2. This observation is quantified by measuring the ratio of areas of C-C, C=C peaks to that of C=O and C-OH for ORGO, which is 1.02.

In Figure 4.4 (D), the FTIR spectroscopy stretching peaks corresponding to the oxygen functionalities such as O-H at 3400 cm^{-1}, C=O at 1720 cm^{-1}, C-O (carboxy) at 1380 cm^{-1}, C-O (epoxy) at 1220 cm^{-1} and C-O (alkoxy) at 1100 cm^{-1} can be observed. The oxygen functional groups especially OH stretching vibrational peak has the highest absorption for GO. The infra-red absorption goes down for RGO indicating the elimination of the oxygen functional groups. The absorption peaks evolve again for ORGO due to the C=C attack by OH●. The evolution of C=0 suggests the increase in carboxylic and carbonyl groups, which are found on the edge plane, indicating that defects in the form of holes are created in ORGO.

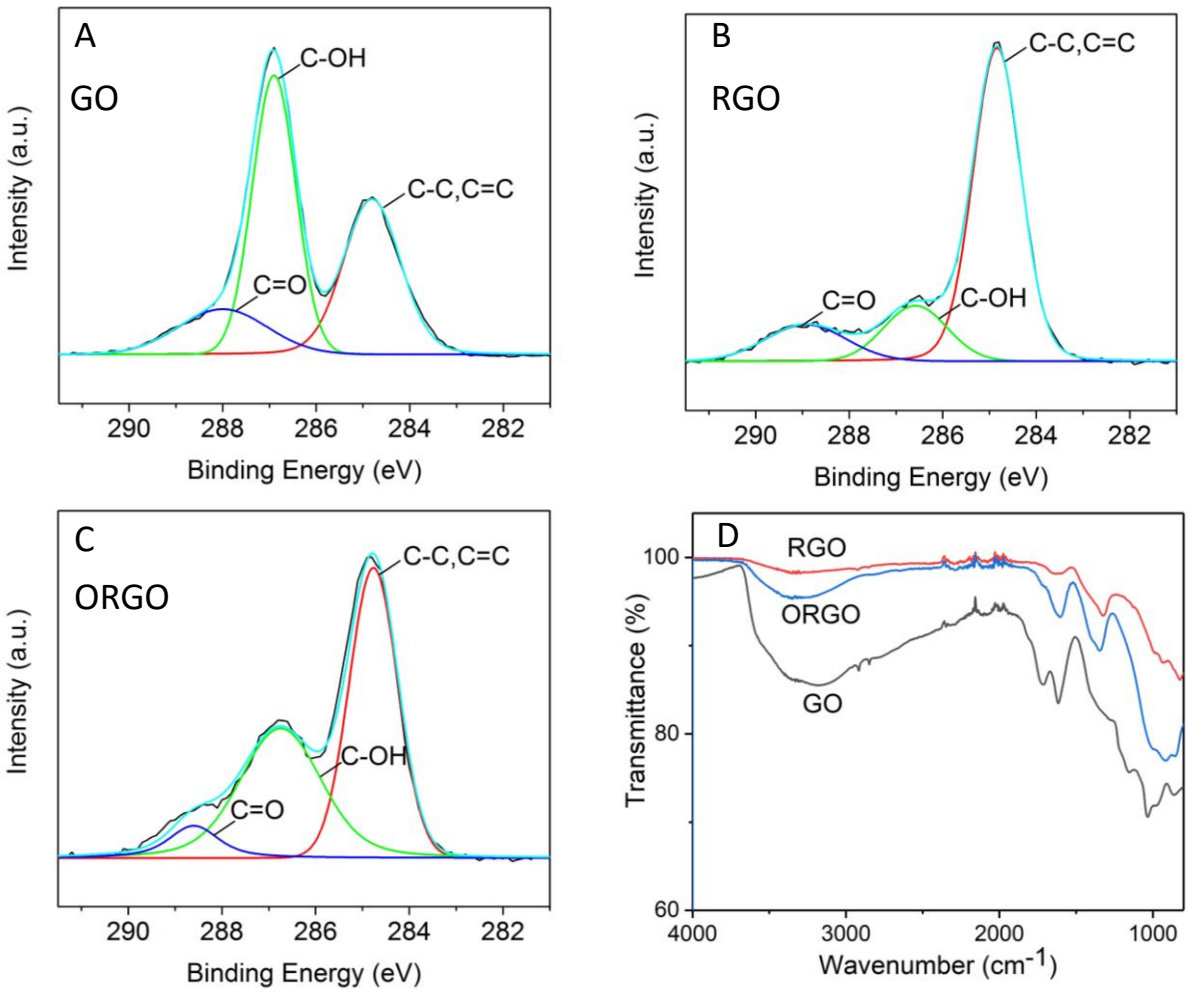

Figure 4.4: XPS Spectra of (A) GO, (B) RGO and (C) ORGO. (D) FTIR spectra of GO, RGO and ORGO.

Raman spectroscopy was performed to compare the degree of disorder in GO, RGO, and ORGO. It is a non-destructive tool that has been used widely to understand various characteristics such as electrical mobility, thermal conductivity, chemical functionalization of graphene and graphene-based materials.[82, 184] This technique uses a monochromatic laser to interact with molecular vibrational modes and phonons in a sample, shifting the photons energy down through inelastic scattering (Stokes-scattering).[185] Raman spectrum of graphene includes two main peaks: G peak located at ~ 1580 cm^{-1} and 2D peak located at ~ 2690 cm^{-1} caused by in-plane optical mode phonon and second-order zone boundary phonon, respectively.[161] The

presence of G and 2D peak are characteristic of sp^2 hybridized carbon-carbon bonds in graphene.[161] The D peak, located at ~1350 cm^{-1} arises due to the breathing modes of six-atom rings and requires an sp^3 hybridized carbon defect for its activation.[161] Hence, D peak is absent from defect-free graphene but exists in defected graphene. The intensity, peak position, and line-width of the Raman modes of graphene can significantly change with the increased number of defects.[186] Lucchese et al. studied the evolution of Raman spectrum of monolayer graphene with respect to the increasing the number of defects created by consecutive Ar^+ ion bombardment on the sample.[187] The results from this study are presented here to better understand Raman spectra of GO, RGO, and ORGO in the subsequent paragraphs. The I_D/I_G ratio, which is the ratio of intensity of the D peak to the G peak was shown to be a function of average distance between defects (L_D) by Lucchese et al.[187] Figure 4.5 shows results from their study; Figure 4.5 (A) shows the evolution of various Raman modes as the defects increase and Figure 4.5 (B) shows a trend of I_D/I_G with respect to L_D. This trend of I_D/I_G was divided into 2 different stages. In stage 1, there is a regime of "low" defect density, where I_D/I_G increases with defects. In stage 2, there is a "high" defect density regime, where I_D/I_G decreases with the defect density.[187] Lucchese et al. showed that $I_D/I_G \propto 1/(L_D)^2$ for "low" defect density regime and $I_D/I_G \propto (L_D)^2$ for "high" defect density. This was due to the existence of two disorder-induced competing contribution to the D band explained in detail in these references.[187-189]

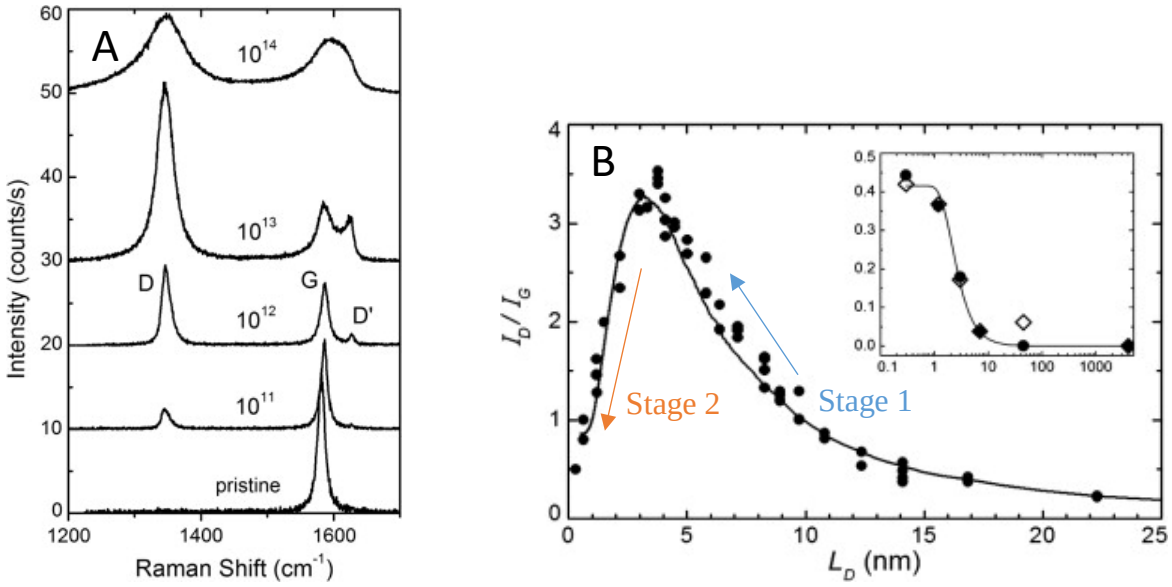

Figure 4.5: (A) Evolution of the Raman spectra of a mono-layer graphene sample deposited on an SiO_2 substrate using 514 nm laser. The ion doses are indicated next to the respective spectrum in units of Ar^+/cm^2. A second disorder-induced peak around ~ 1620 cm^{-1}(named the D' band) also appears but is not the focus feature in this work. (B) The I_D/I_G data points as a function of the average distance L_D between defects. The inset shows the I_D/I_G versus L_D on a log scale for two graphite samples.[181]

Raman spectra for synthesized GO, RGO, and ORGO are shown in Figure 4.6. The strong D band confirms lattice distortion and a large number of defects in all the samples. The G peak of GO displays a shift to higher frequencies (blue-shift) as compared to graphene (1598 cm^{-1} for GO versus 1580 cm^{-1} for graphene). In RGO, a red-shift is observed with G peak at ~ 1590 cm^{-1}, suggesting the formation of graphene-like structure. These observations are in agreement with the literature.[186, 190] Further, in ORGO the G peak blue shifts to a peak at ~ 1594 cm^{-1}, suggesting the addition of oxygen functional groups to the graphene basal plane. The I_D/I_G ratio of GO is 0.96, which is increased to 1.06 upon reduction to form RGO. This is a common trend which has been observed by various other studies.[13, 191-194] Hence, it has been suggested that I_D/I_G ratio should not be directly correlated to the degree of oxidation/reduction of graphene or to the ratio of sp^3/sp^2 carbons.[195, 196] This increase in I_D/I_G is understood to be caused by the formation of small size graphitic domains which decrease the average size of sp^2 domains

initially present in GO.[13, 191, 197] It should be noted that GO has a large amount of sp^3 carbons leading to large disorder which suggests that defect status of GO should be at stage 2.[186] Reduction of GO should decrease the defect density thereby increasing the I_D/I_G ratio due to relationship discussed in the previous paragraph. During the conversion of RGO to ORGO, defects are created, and I_D/I_G ratio is increased. This means that the defect status of RGO should be at stage 1 where I_D/I_G ratio increases with the defect density. The conclusions drawn from Raman spectroscopy agree well with the XPS and FTIR spectroscopy.

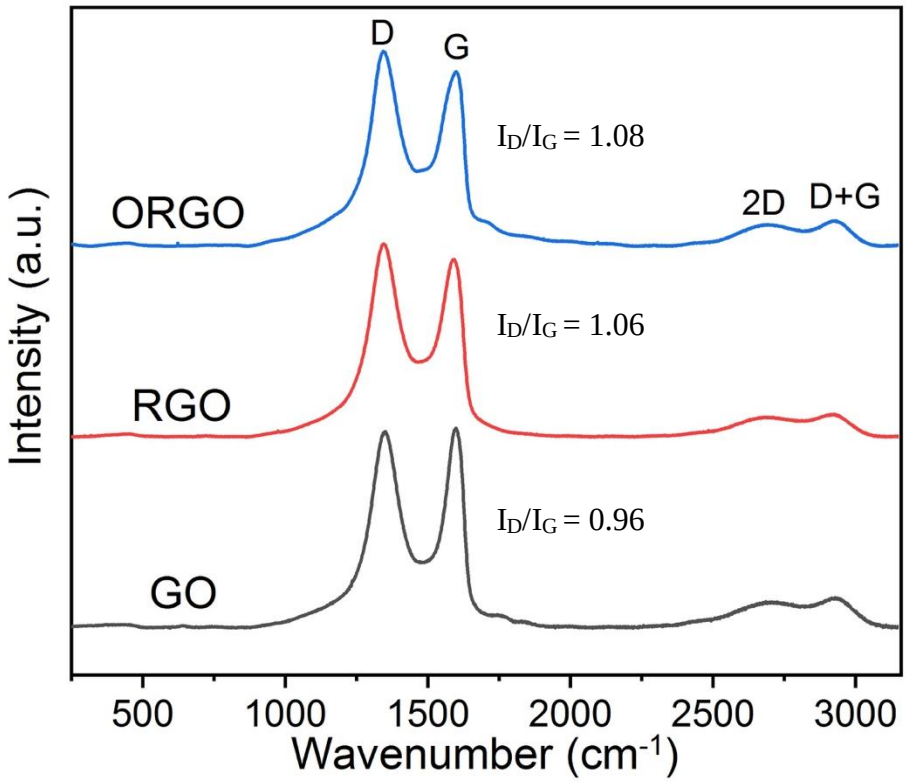

Figure 4.6: Raman spectra of GO, RGO and ORGO films made by evaporating the water from respective dispersions using 532 nm laser.

The morphology of the GO and ORGO samples were investigated using transmission electron microscopy (TEM). The TEM images in Figure 4.7 compare the resulting ORGO with the GO. The TEM image of GO shows the existence of wrinkles and folded edges on the single-layer GO sheet. These are common features observed in TEM of GO sheets.[5, 151, 198] The

morphology of ORGO sheets appear very different from the GO sheets. Firstly, the holes in the ORGO sheets are shown in red circles. Secondly, the region enclosed with white boundary is very dark as compared to the outside regions and hence represents multilayer sheets which are a result of the individual sheets restacking during the reduction process. Lastly, the degree of wrinkling exhibited by ORGO is also much higher in as compared to GO. Radich et al. observed the similar wrinkling in their ORGO samples, which they attributed to the O_2 bubble nucleation caused by the decomposition of H_2O_2 during irradiation to H_2O and O_2 along with the competing reaction of hydroxyl radical production.[5]

This microwave-assisted oxidation of RGO results in the formation of holey graphene morphology. However, the hole diameter is very large (~400 nm) and sheets appear to be highly damaged due to aggressive etching. Hence, H_2O_2 concentration, MW irradiation time, MW power and reaction temperature needs to be controlled to get the desired pore size. These parameters could be controlled efficiently in industry-grade microwave reactors.

In summary, MW photolysis of H_2O_2 initiates the morphological and chemical functionality changes in RGO sheets where wrinkles are formed because of O_2 nucleation. The OH● radical attacks the sp^2-hybridized carbons of RGO to produce an OH adduct. The continuous attack of hydroxyl radicals causes complete oxidation of the carbons to CO_2 and water which creates the holes in the sheet. In case of incomplete oxidation, the carbon hybridization changes from sp^2 to sp^3 i.e. increase in the oxygen functionalities as observed by XPS and FTIR spectra. This is a novel solution-based technique to produce holey graphene.

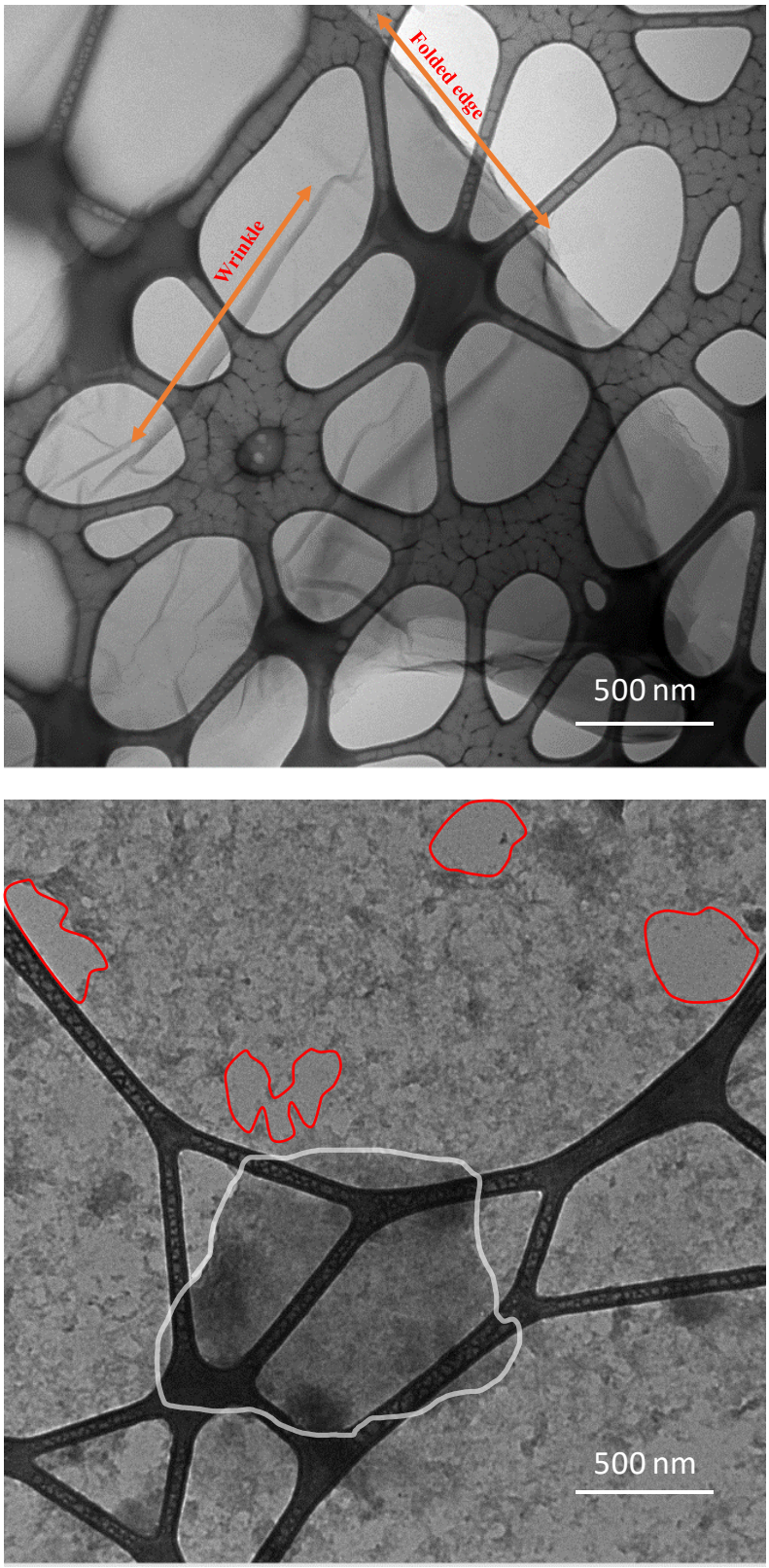

Figure 4.7: TEM images of GO (top) and ORGO (bottom).

4.3.3 Holey Graphene Frameworks

In this section, the synthesis results of self-assembled holey graphene frameworks (HGFs) are reported. HGFs were synthesized from 2.0 mg/mL ORGO using the method described in section 3.2.2. The resulting 3D structure formed is shown in Figure 4.8 (B). However, this resulting material was not strong and collapsed as it was being taken out of the vial as shown in Figure 4.8 (C). There are two possible reasons of this failure - 1) The holey graphene sheets were too damaged (excessively etched) and were mechanically weak for self-assembly and 2) There were not enough oxygen functional groups present in ORGO to undergo a reduction reaction which will cause the self-assembly. Future research could focus on resolving these issues by controlling the reaction conditions as mentioned in the previous section.

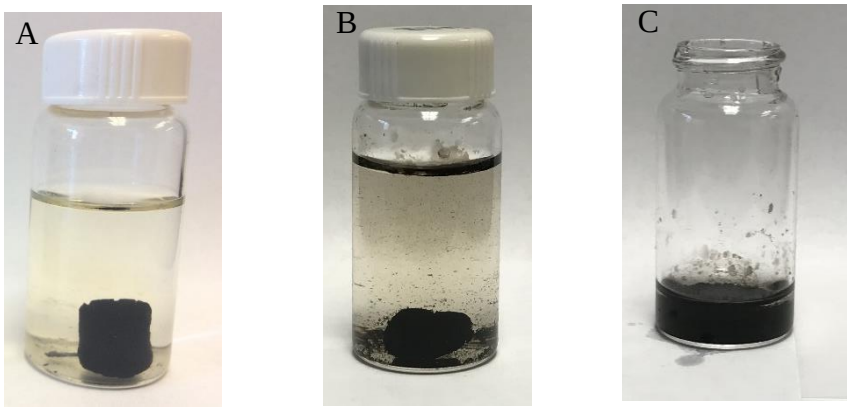

Figure 4.8: (A) Fully formed graphene hydrogel or graphene framework from GO dispersion, (B) weak and poorly formed graphene framework from ORGO dispersion, (C) collapsed graphene framework.

4.4 Conclusion

Through MW assisted OH● radical attack on RGO, a new graphene-based material, holey-graphene/ORGO, with pores and wrinkles can be produced. A significant number of oxygen functionalities are observed after the OH● radicals attack RGO as shown in FTIR spectra. By controlling the reaction conditions, hydroxyl radical driven reaction can facilitate production materials whose properties such as degree of oxidation and nanoporous structure can be tuned toward specific applications. For example, ORGO can be utilized in synthesizing self-assembled holey graphene framework, which might exhibit a strong physical structure and improved electrochemical performance because of increased ion diffusion pathways. This work also complements recent advances in the theoretical understanding of various functionalities and surface chemistry of GO and RGO.[199] These results enhance the understanding of RGO stability when used in applications where free radical formation can occur such as photocatalysis and electrocatalysis. In addition, holey graphene may be a better support to design 3D architectures for electrochemical capacitors, Li-ion batteries or other electrochemical devices where ion transport of electroactive species strongly influences the device performance.

Chapter 5

Conclusions and Directions for Future Research

5.1 Conclusions

Graphene-based nanostructures have the potential to significantly improve the performance of energy storage electrodes. The superior properties such as high surface area and electronic conductivity along with solution-based chemistry of GO/RGO, open a wide range possibility in advanced electrode designs. Energy storage applications require the fundamental process of electron transport to an active material and diffusion of electroactive or chemical species to the surface of active material. By understanding the surface chemistry, stability and assembly of GO and RGO on a fundamental level, highly advanced electrode design with tunable properties can become a possibility.

In Chapter 2, the evolution of hydroxyl radicals through photoexcitation of graphene oxide was demonstrated, a critically-important molecule in a number of chemistry-relevant areas of research. Fluorescence spectroscopy with a terephthalic acid probe molecule and femtosecond ultrafast spectroscopy with thiocyanate probe was employed to show photon-flux proportionality to OH● yield and relatively high (>80%) quantum yield, respectively. The results suggest a relatively efficient photoconversion process. Finally, GO was employed as a photochemical OH● source to degrade a recalcitrant textile dye as proof of concept. This is the first direct experimental evidence to demonstrate OH● are liberated during photoexcitation of GO. This fundamental knowledge will be of significant interest to the chemistry community at large and can facilitate a deeper understanding of the stability of graphene oxides.

In Chapter 3, the effect of GO sheet aspect ratio and GO concentration on the self-assembled 3D graphene frameworks were investigated. The graphene frameworks with the largest sheet size exhibited the best electrochemical performance. The high capacitance and low τ_o are indicative of high ion accessible surface area and efficient ion diffusion. This was supported SSA and pore volume were measured using BET characterization. Two reasons were attributed to the improved SSA and pore volume of LGF. First, the amplitude of ripples in UL-GO sheets is larger as compared to small GO sheets maintain thermodynamic stability. The large ripples create porous channels for efficient ion diffusion and avoid complete restacking of the sheets following self-assembly. Second, the total number of intersheet contacts are limited by the energy requirement for sheet deformation. This reason combined with the fact that the number of sheets in GO dispersion decreases as the sheet size increases suggests that there are fewer number of intersheet contacts in LGF as compared GF. In a subsequent study, graphene frameworks were formed with varying concentration of UL-GO from 0.5 mg/mL to 4.0 mg/mL and varying concentration of GO from 2.0 mg/mL to 12 mg/mL. The best electrochemical performance was displayed by LGF synthesized from 1.5 mg/mL UL-GO dispersion. For GF, the best electrochemical performance was displayed by 3.5 mg/mL GO dispersion. Below the optimum concentration, there were not enough intersheet contacts for the efficient flow of electrons, which increased the charge-transfer resistance, and above optimum concentration, capacitance and RC time constant values deteriorated as the SSA and pore volume decreased due to increased packing density. Through this work, a deeper understanding of the structure-processing-property relationships between GO dispersions and 3D graphene frameworks were developed.

In Chapter 4, a microwave-assisted reaction between RGO, and hydroxyl radicals was explored. The reaction was utilized to generate a new graphene morphology with holes and wrinkles referred to oxidized RGO (ORGO). Microwave photolysis of H_2O_2 leading to the production of OH● was demonstrated for the first time. It was shown that OH● produced attack both defective sites and sp^2 hybridized carbon within RGO to chemically etch carbons to locally produce holes in the graphene sheet and to produce oxygen functionalities in case of partial oxidation. Holey graphene has potential application not just in the field of capacitive energy storage but also in batteries, catalysis, optoelectronics and separation processes. The holey graphene morphology can be tuned for the desired applications by controlling temperature, pressure in a microwave reactor. This new method of synthesis has many advantages like solution-based chemistry, low energy requirement, and inexpensive infrastructure.

5.2 Directions for Future Research

This research has advanced the understanding of the production of novel 3D graphene frameworks for electrochemical applications. However, there are many remaining challenges that need to be addressed for the development and commercialization of 3D graphene-based electrodes with outstanding electrochemical properties.

1. Further refinements in understanding of the GO reduction process and a better understanding of intermolecular interactions in GO/RGO dispersion.
2. More efficient methods to reduce restacking of RGO sheets.
3. Better understanding of how to improve ion diffusion inside RGO based electrodes.
4. Design of hierarchical 3D porous architectures as support for pseudocapacitors.

Moving from two to three-dimensional bulk materials has shown promising results in terms of increased energy storage performance. Self-assembly via chemical reduction is one of the cleaner ways to create 3D materials and they offer a great advantage of avoiding a binder material while fabricating the electrode. The binder decreases electrochemical performance by decreasing the specific capacitance and electronic conductivity. Further, understanding of fundamental relationships between the structure of 3D materials and the development of new synthetic methods for precise control of device architectures through computational studies will be a great step for the future. The results from this work will also influence research in the field of fuel cells and hydrogen storage materials.

Finally, synthesizing hybrid electrode materials with metal oxides (MO) nanoparticles on graphene-based frameworks will be the key to develop exceptional energy storage devices. The 3D graphene support will not only increase the electrical conductivity of the hybrid electrode but also provides a large surface area so that MO loadings can be maximized. For example - controlled electrochemical deposition of MnO_2 nanoparticles on 3D graphene frameworks can be conducted to build a hybrid material. The fundamental understanding of pseudocapacitance, charge transfer, and ion diffusion will be crucial to the development of next-generation electrode materials. New synthesis approaches are required which produced tailored functionalized nanoscale architecture. Development of cheaper and environmentally safe energy storage system with high energy and power density is one of the biggest challenges of our time. The work presented here was a small step towards a better understanding of graphene-based materials to fabricate superior electrochemical storage devices.

References

1. Bolotin, K. I.; Sikes, K. J.; Jiang, Z.; Klima, M.; Fudenberg, G.; Hone, J.; Kim, P.; Stormer, H. L., Ultrahigh Electron Mobility in Suspended Graphene. *Solid State Communications* **2008,** *146* (9-10), 351-355.

2. Zhu, Y.; Murali, S.; Cai, W.; Li, X.; Suk, J. W.; Potts, J. R.; Ruoff, R. S., Graphene and Graphene Oxide: Synthesis, Properties, and Applications. *Advanced Materials* **2010,** *22* (35), 3906-3924.

3. Xia, J.; Chen, F.; Li, J.; Tao, N., Measurement of the Quantum Capacitance of Graphene. *Nature Nanotechnology* **2009,** *4* (8), 505-509.

4. Cao, X.; Yin, Z.; Zhang, H., Three-Dimensional Graphene Materials: Preparation, Structures and Application in Supercapacitors. *Energy & Environmental Science* **2014,** *7* (6), 1850-1865.

5. Radich, J. G.; Kamat, P. V., Making Graphene Holey. Gold-Nanoparticle-Mediated Hydroxyl Radical Attack on Reduced Graphene Oxide. *ACS Nano* **2013,** *7* (6), 5546-5557.

6. May, J. W., Platinum Surface Leed Rings. *Surface Science* **1969,** *17*, 267-270.

7. Schedin, F.; Geim, A.; Morozov, S.; Hill, E.; Blake, P.; Katsnelson, M.; Novoselov, K., Detection of Individual Gas Molecules Adsorbed on Graphene. *Nature Materials* **2007,** *6* (9), 652.

8. Van Bommel, A.; Crombeen, J.; Van Tooren, A., Leed and Auger Electron Observations of the SiC (0001) Surface. *Surface Science* **1975,** *48* (2), 463-472.

9. Juang, Z.-Y.; Wu, C.-Y.; Lu, A.-Y.; Su, C.-Y.; Leou, K.-C.; Chen, F.-R.; Tsai, C.-H., Graphene Synthesis by Chemical Vapor Deposition and Transfer by a Roll-to-Roll Process. *Carbon* **2010,** *48* (11), 3169-3174.

10. Hummers Jr, W. S.; Offeman, R. E., Preparation of Graphitic Oxide. *Journal of the American Chemical Society* **1958,** *80* (6), 1339-1339.

11. Acik, M.; Lee, G.; Mattevi, C.; Pirkle, A.; Wallace, R. M.; Chhowalla, M.; Cho, K.; Chabal, Y., The Role of Oxygen During Thermal Reduction of Graphene Oxide Studied by Infrared Absorption Spectroscopy. *Journal of Physical Chemistry C* **2011,** *115* (40), 19761-19781.

12. Larciprete, R.; Fabris, S.; Sun, T.; Lacovig, P.; Baraldi, A.; Lizzit, S., Dual Path Mechanism in the Thermal Reduction of Graphene Oxide. *Journal of the American Chemical Society* **2011,** *133* (43), 17315-17321.

13. Stankovich, S.; Dikin, D. A.; Piner, R. D.; Kohlhaas, K. A.; Kleinhammes, A.; Jia, Y.; Wu, Y.; Nguyen, S. T.; Ruoff, R. S., Synthesis of Graphene-Based Nanosheets via Chemical Reduction of Exfoliated Graphite Oxide. *Carbon* **2007,** *45* (7), 1558-1565.

14. Gomez-Navarro, C.; Weitz, R. T.; Bittner, A. M.; Scolari, M.; Mews, A.; Burghard, M.; Kern, K., Electronic Transport Properties of Individual Chemically Reduced Graphene Oxide Sheets. *Nano Letters* **2007,** *7* (11), 3499-3503.

15. Shao, Y. Y.; Wang, J.; Engelhard, M.; Wang, C. M.; Lin, Y. H., Facile and Controllable Electrochemical Reduction of Graphene Oxide and Its Applications. *Journal of Materials Chemistry* **2009,** *20* (4), 743-748.

16. Guo, H. L.; Wang, X. F.; Qian, Q. Y.; Wang, F. B.; Xia, X. H., A Green Approach to the Synthesis of Graphene Nanosheets. *ACS Nano* **2009,** *3* (9), 2653-2659.

17. Lightcap, I. V.; Kosel, T. H.; Kamat, P. V., Anchoring Semiconductor and Metal Nanoparticles on a Two-Dimensional Catalyst Mat. Storing and Shuttling Electrons with Reduced Graphene Oxide. *Nano Letters* **2010,** *10* (2), 577-583.

18. Williams, G.; Seger, B.; Kamat, P. V., TiO_2-Graphene Nanocomposites. UV-Assisted Photocatalytic Reduction of Graphene Oxide. *ACS Nano* **2008,** *2* (7), 1487-1491.

19. Erickson, K.; Erni, R.; Lee, Z.; Alem, N.; Gannett, W.; Zettl, A., Determination of the Local Chemical Structure of Graphene Oxide and Reduced Graphene Oxide. *Advanced Materials* **2010,** *22* (40), 4467-4472.

20. Lerf, A.; He, H.; Forster, M.; Klinowski, J., Structure of Graphite Oxide Revisited. *The Journal of Physical Chemistry B* **1998,** *102* (23), 4477-4482.

21. Li, D.; Müller, M. B.; Gilje, S.; Kaner, R. B.; Wallace, G. G., Processable Aqueous Dispersions of Graphene Nanosheets. *Nature Nanotechnology* **2008,** *3* (2), 101-105.

22. Fernández-Merino, M.; Guardia, L.; Paredes, J.; Villar-Rodil, S.; Solís-Fernández, P.; Martínez-Alonso, A.; Tascón, J., Vitamin C Is an Ideal Substitute for Hydrazine in the Reduction of Graphene Oxide Suspensions. *The Journal of Physical Chemistry C* **2010,** *114* (14), 6426-6432.

23. Han, S.; Wu, D.; Li, S.; Zhang, F.; Feng, X., Porous Graphene Materials for Advanced Electrochemical Energy Storage and Conversion Devices. *Advanced Materials* **2014,** *26* (6), 849-64.

24. Zhang, L. L.; Zhou, R.; Zhao, X., Graphene-Based Materials as Supercapacitor Electrodes. *Journal of Materials Chemistry* **2010,** *20* (29), 5983-5992.

25. Jiang, H.; Lee, P. S.; Li, C., 3d Carbon Based Nanostructures for Advanced Supercapacitors. *Energy & Environmental Science* **2013,** *6* (1), 41-53.

26. Simon, P.; Gogotsi, Y., Materials for Electrochemical Capacitors. *Nature Materials* **2008,** *7* (11), 845-854.

27. Wang, G.; Zhang, L.; Zhang, J., A Review of Electrode Materials for Electrochemical Supercapacitors. *Chemical Society Reviews* **2012,** *41* (2), 797-828.

28. Wang, Y.; Shi, Z.; Huang, Y.; Ma, Y.; Wang, C.; Chen, M.; Chen, Y., Supercapacitor Devices Based on Graphene Materials. *The Journal of Physical Chemistry C* **2009,** *113* (30), 13103-13107.

29. Wang, Z.-L.; Xu, D.; Wang, H.-G.; Wu, Z.; Zhang, X.-B., In Situ Fabrication of Porous Graphene Electrodes for High-Performance Energy Storage. *ACS Nano* **2013,** *7* (3), 2422-2430.

30. Jiang, Z. J.; Jiang, Z., Fabrication of Nitrogen-Doped Holey Graphene Hollow Microspheres and Their Use as an Active Electrode Material for Lithium Ion Batteries. *ACS Applied Materials & Interfaces* **2014,** *6* (21), 19082-91.

31. El-Kady, M. F.; Strong, V.; Dubin, S.; Kaner, R. B., Laser Scribing of High-Performance and Flexible Graphene-Based Electrochemical Capacitors. *Science* **2012,** *335* (6074), 1326-1330.

32. Liu, C.; Yu, Z.; Neff, D.; Zhamu, A.; Jang, B. Z., Graphene-Based Supercapacitor with an Ultrahigh Energy Density. *Nano Letters* **2010,** *10* (12), 4863-4868.

33. Capuano, L., International Energy Outlook 2018 (Ieo2018). *US Energy Information Administration (EIA): Washington, DC, USA* **2018,** *2018*, 21.

34. Ragone, D. V. *Review of Battery Systems for Electrically Powered Vehicles*; 0148-7191; SAE Technical Paper: **1968**.

35. Conway, B. E., Transition from "Supercapacitor" to "Battery" Behavior in Electrochemical Energy Storage. *Journal of the Electrochemical Society* **1991,** *138* (6), 1539-1548.

36. Goodenough, J. B.; Abruna, H.; Buchanan, M., *Basic Research Needs for Electrical Energy Storage*, Report of the Basic Energy Sciences Workshop for Electrical Energy Storage, **2007.**

37. Miller, J. R.; Simon, P., Electrochemical Capacitors for Energy Management. *Science Magazine* **2008,** *321* (5889), 651-652.

38. Long, J. W.; Bélanger, D.; Brousse, T.; Sugimoto, W.; Sassin, M. B.; Crosnier, O., Asymmetric Electrochemical Capacitors—Stretching the Limits of Aqueous Electrolytes. *MRS Bulletin* **2011,** *36* (07), 513-522.

39. Zhao, S.; Wu, F.; Yang, L.; Gao, L.; Burke, A. F., A Measurement Method for Determination of Dc Internal Resistance of Batteries and Supercapacitors. *Electrochemistry Communications* **2010,** *12* (2), 242-245.

40. Pandolfo, A.; Hollenkamp, A., Carbon Properties and Their Role in Supercapacitors. *Journal of Power Sources* **2006,** *157* (1), 11-27.

41. Naoi, K.; Simon, P., New Materials and New Configurations for Advanced Electrochemical Capacitors. *Journal of The Electrochemical Society* **2008,** *17* (1), 34-37.

42. Simon, P.; Burke, A., Nanostructured Carbons: Double-Layer Capacitance and More. *The Electrochemical Society Interface* **2008,** *17* (1), 38.

43. Dubal, D. P.; Ayyad, O.; Ruiz, V.; Gomez-Romero, P., Hybrid Energy Storage: The Merging of Battery and Supercapacitor Chemistries. *Chemical Society Reviews* **2015,** *44* (7), 1777-1790.

44. Kim, T.; Jung, G.; Yoo, S.; Suh, K. S.; Ruoff, R. S., Activated Graphene-Based Carbons as Supercapacitor Electrodes with Macro-and Mesopores. *ACS Nano* **2013,** *7* (8), 6899-6905.

45. Han, X.; Funk, M. R.; Shen, F.; Chen, Y.-C.; Li, Y.; Campbell, C. J.; Dai, J.; Yang, X.; Kim, J.-W.; Liao, Y., Scalable Holey Graphene Synthesis and Dense Electrode Fabrication toward High-Performance Ultracapacitors. *ACS Nano* **2014,** *8* (8), 8255-8265.

46. Lin, Y.; Han, X.; Campbell, C. J.; Kim, J.-W.; Zhao, B.; Luo, W.; Dai, J.; Hu, L.; Connell, J. W., Holey Graphene Nanomanufacturing: Structure, Composition, and Electrochemical Properties. *Advanced Functional Materials* **2015,** *25* (19), 2920-2927.

47. Peng, Y.-Y.; Liu, Y.-M.; Chang, J.-K.; Wu, C.-H.; Ger, M.-D.; Pu, N.-W.; Chang, C.-L., A Facile Approach to Produce Holey Graphene and Its Application in Supercapacitors. *Carbon* **2015,** *81*, 347-356.

48. Lin, Y.; Watson, K. A.; Kim, J.-W.; Baggett, D. W.; Working, D. C.; Connell, J. W., Bulk Preparation of Holey Graphene via Controlled Catalytic Oxidation. *Nanoscale* **2013,** *5* (17), 7814-7824.

49. Zhao, X.; Hayner, C. M.; Kung, M. C.; Kung, H. H., Flexible Holey Graphene Paper Electrodes with Enhanced Rate Capability for Energy Storage Applications. *ACS Nano* **2011,** *5* (11), 8739-8749.

50. Fan, Z.; Zhao, Q.; Li, T.; Yan, J.; Ren, Y.; Feng, J.; Wei, T., Easy Synthesis of Porous Graphene Nanosheets and Their Use in Supercapacitors. *Carbon* **2012,** *50* (4), 1699-1703.

51. Jhajharia, S. K.; Selvaraj, K., Non-Templated Ambient Nanoperforation of Graphene: A Novel Scalable Process and Its Exploitation for Energy and Environmental Applications. *Nanoscale* **2015,** *7* (46), 19705-13.

52. Bai, J.; Zhong, X.; Jiang, S.; Huang, Y.; Duan, X., Graphene Nanomesh. *Nature Nanotechnology* **2010,** *5* (3), 190-194.

53. Akhavan, O., Graphene Nanomesh by ZnO Nanorod Photocatalysts. *ACS Nano* **2010,** *4* (7), 4174-4180.

54. Zeng, Z.; Huang, X.; Yin, Z.; Li, H.; Chen, Y.; Li, H.; Zhang, Q.; Ma, J.; Boey, F.; Zhang, H., Fabrication of Graphene Nanomesh by Using an Anodic Aluminum Oxide Membrane as a Template. *Advanced Materials* **2012,** *24* (30), 4138-4142.

55. Wang, M.; Fu, L.; Gan, L.; Zhang, C.; Rümmeli, M.; Bachmatiuk, A.; Huang, K.; Fang, Y.; Liu, Z., Cvd Growth of Large Area Smooth-Edged Graphene Nanomesh by Nanosphere Lithography. *Scientific Reports* **2013,** *3*, 1238.

56. Xu, Y.; Lin, Z.; Zhong, X.; Huang, X.; Weiss, N. O.; Huang, Y.; Duan, X., Holey Graphene Frameworks for Highly Efficient Capacitive Energy Storage. *Nature Communications* **2014,** *5*, 4554.

57. Sheng, K.-x.; Xu, Y.-x.; Chun, L.; Shi, G.-q., High-Performance Self-Assembled Graphene Hydrogels Prepared by Chemical Reduction of Graphene Oxide. *New Carbon Materials* **2011,** *26* (1), 9-15.

58. Yang, X.; Cheng, C.; Wang, Y.; Qiu, L.; Li, D., Liquid-Mediated Dense Integration of Graphene Materials for Compact Capacitive Energy Storage. *Science* **2013,** *341* (6145), 534-537.

59. Wang, G.; Sun, X.; Lu, F.; Sun, H.; Yu, M.; Jiang, W.; Liu, C.; Lian, J., Flexible Pillared Graphene- Paper Electrodes for High- Performance Electrochemical Supercapacitors. *Small* **2012,** *8* (3), 452-459.

60. Yu, D.; Goh, K.; Wang, H.; Wei, L.; Jiang, W.; Zhang, Q.; Dai, L.; Chen, Y., Scalable Synthesis of Hierarchically Structured Carbon Nanotube-Graphene Fibres for Capacitive Energy Storage. *Nature Nanotechnology* **2014,** *9* (7), 555-562.

61. Kou, L.; Huang, T.; Zheng, B.; Han, Y.; Zhao, X.; Gopalsamy, K.; Sun, H.; Gao, C., Coaxial Wet-Spun Yarn Supercapacitors for High-Energy Density and Safe Wearable Electronics. *Nature Communications* **2014,** *5*.

62. Hao, P.; Zhao, Z.; Leng, Y.; Tian, J.; Sang, Y.; Boughton, R. I.; Wong, C.; Liu, H.; Yang, B., Graphene-Based Nitrogen Self-Doped Hierarchical Porous Carbon Aerogels Derived from Chitosan for High Performance Supercapacitors. *Nano Energy* **2015,** *15*, 9-23.

63. Chen, S.; Zhu, J.; Wu, X.; Han, Q.; Wang, X., Graphene Oxide− MnO_2 Nanocomposites for Supercapacitors. *ACS Nano* **2010,** *4* (5), 2822-2830.

64. Yan, J.; Fan, Z.; Wei, T.; Qian, W.; Zhang, M.; Wei, F., Fast and Reversible Surface Redox Reaction of Graphene–MnO_2 Composites as Supercapacitor Electrodes. *Carbon* **2010,** *48* (13), 3825-3833.

65. Lee, H.; Kang, J.; Cho, M. S.; Choi, J.-B.; Lee, Y., Mno 2/Graphene Composite Electrodes for Supercapacitors: The Effect of Graphene Intercalation on Capacitance. *Journal of Materials Chemistry* **2011,** *21* (45), 18215-18219.

66. Yu, G.; Hu, L.; Vosgueritchian, M.; Wang, H.; Xie, X.; McDonough, J. R.; Cui, X.; Cui, Y.; Bao, Z., Solution-Processed Graphene/MnO_2 Nanostructured Textiles for High-Performance Electrochemical Capacitors. *Nano Letters* **2011,** *11* (7), 2905-2911.

67. Li, X. S.; Cai, W. W.; An, J. H.; Kim, S.; Nah, J.; Yang, D. X.; Piner, R.; Velamakanni, A.; Jung, I.; Tutuc, E.; Banerjee, S. K.; Colombo, L.; Ruoff, R. S., Large-Area Synthesis of High-Quality and Uniform Graphene Films on Copper Foils. *Science* **2009,** *324* (5932), 1312-1314.

68. Zeller, P.; Danhardt, S.; Gsell, S.; Schreck, M.; Wintterlin, J., Scalable Synthesis of Graphene on Single Crystal Ir (111) Films. *Surface Science* **2012,** *606* (19-20), 1475-1480.

69. Yan, Z.; Lin, J.; Peng, Z. W.; Sun, Z. Z.; Zhu, Y.; Li, L.; Xiang, C. S.; Samuel, E. L.; Kittrell, C.; Tour, J. M., Toward the Synthesis of Wafer-Scale Single-Crystal Graphene on Copper Foils. *ACS Nano* **2012,** *6* (10), 9110-9117.

70. Wang, H.; Wang, G. Z.; Bao, P. F.; Yang, S. L.; Zhu, W.; Xie, X.; Zhang, W. J., Controllable Synthesis of Submillimeter Single-Crystal Monolayer Graphene Domains

on Copper Foils by Suppressing Nucleation. *Journal of the American Chemical Society* **2012,** *134* (44), 18476-18476.

71. Hamilton, C. E.; Lomeda, J. R.; Sun, Z. Z.; Tour, J. M.; Barron, A. R., High-Yield Organic Dispersions of Unfunctionalized Graphene. *Nano Letters* **2009,** *9* (10), 3460-3462.

72. Oh, S. Y.; Kim, S. H.; Chi, Y. S.; Kang, T. J., Fabrication of Oxide-Free Graphene Suspension and Transparent Thin Films Using Amide Solvent and Thermal Treatment. *Applied Surface Science* **2012,** *258* (22), 8837-8844.

73. Chen, N.; Liu, Y. T.; Xie, X. M.; Ye, X. Y.; Feng, X.; Chen, Y. F.; Wang, Y. H., High-Concentration Aliphatic and Aromatic Dispersions of Single- and Few-Layer Graphene Noncovalently Modified by Block Copolymer Crystallization. *Carbon* **2012,** *50* (12), 4760-4764.

74. Skaltsas, T.; Karousis, N.; Yan, H. J.; Wang, C. R.; Pispas, S.; Tagmatarchis, N., Graphene Exfoliation in Organic Solvents and Switching Solubility in Aqueous Media with the Aid of Amphiphilic Block Copolymers. *Journal of Materials Chemistry* **2012,** *22* (40), 21507-21512.

75. Hummers, W. S.; Offeman, R. E., Preparation of Graphitic Oxide. *Journal of the American Chemical Society* **1958,** *80* (6), 1339-1339.

76. Kim, J.; Cote, L. J.; Kim, F.; Yuan, W.; Shull, K. R.; Huang, J. X., Graphene Oxide Sheets at Interfaces. *Journal of the American Chemical Society* **2010,** *132* (23), 8180-8186.

77. Paredes, J. I.; Villar-Rodil, S.; Martinez-Alonso, A.; Tascon, J. M. D., Graphene Oxide Dispersions in Organic Solvents. *Langmuir* **2008,** *24* (19), 10560-10564.

78. Dreyer, D. R.; Park, S.; Bielawski, C. W.; Ruoff, R. S., The Chemistry of Graphene Oxide. *Chemical Society Reviews* **2010,** *39* (1), 228-240.

79. De Jesus, L. R.; Dennis, R. V.; Depner, S. W.; Jaye, C.; Fischer, D. A.; Banerjee, S., Inside and Outside: X-Ray Absorption Spectroscopy Mapping of Chemical Domains in Graphene Oxide. *The Journal of Physical Chemistry Letters* **2013,** *4* (18), 3144-3151.

80. Gilje, S.; Han, S.; Wang, M.; Wang, K. L.; Kaner, R. B., A Chemical Route to Graphene for Device Applications. *Nano Letters* **2007,** *7* (11), 3394-3398.

81. Kulkarni, D. D.; Kim, S.; Chyasnavichyus, M.; Hu, K.; Fedorov, A. G.; Tsukruk, V. V., Chemical Reduction of Individual Graphene Oxide Sheets as Revealed by Electrostatic Force Microscopy. *Journal of the American Chemical Society* **2014,** *136* (18), 6546-6549.

82. Ramesha, G. K.; Sampath, S., Electrochemical Reduction of Oriented Graphene Oxide Films: An in Situ Raman Spectroelectrochemical Study. *Journal of Physical Chemistry C* **2009,** *113* (19), 7985-7989.

83. Yu, H. W.; He, J. J.; Sun, L.; Tanaka, S.; Fugetsu, B., Influence of the Electrochemical Reduction Process on the Performance of Graphene-Based Capacitors. *Carbon* **2013,** *51*, 94-101.

84. Yang, J.; Gunasekaran, S., Electrochemically Reduced Graphene Oxide Sheets for Use in High Performance Supercapacitors. *Carbon* **2013,** *51*, 36-44.

85. Ding, Y. H.; Zhang, P.; Zhuo, Q.; Ren, H. M.; Yang, Z. M.; Jiang, Y., A Green Approach to the Synthesis of Reduced Graphene Oxide Nanosheets under UV Irradiation. *Nanotechnology* **2011,** *22* (21).

86. Shul'ga, Y. M.; Vasilets, V. N.; Baskakov, S. A.; Muradyan, V. E.; Skryleva, E. A.; Parkhomenko, Y. N., Photoreduction of Graphite Oxide Nanosheets with Vacuum Ultraviolet Radiation. *High Energy Chemistry* **2012,** *46* (2), 117-121.

87. Guardia, L.; Villar-Rodil, S.; Paredes, J. I.; Rozada, R.; Martinez-Alonso, A.; Tascon, J. M. D., UV Light Exposure of Aqueous Graphene Oxide Suspensions to Promote Their Direct Reduction, Formation of Graphene-Metal Nanoparticle Hybrids and Dye Degradation. *Carbon* **2012,** *50* (3), 1014-1024.

88. Kim, S. R.; Parvez, M. K.; Chhowalla, M., UV-Reduction of Graphene Oxide and Its Application as an Interfacial Layer to Reduce the Back-Transport Reactions in Dye-Sensitized Solar Cells. *Chemical Physics Letters* **2009,** *483* (1-3), 124-127.

89. McDonald, M. P.; Eltom, A.; Vietmeyer, F.; Thapa, J.; Morozov, Y. V.; Sokolov, D. A.; Hodak, J. H.; Vinodgopal, K.; Kamat, P. V.; Kuno, M., Direct Observation of Spatially Heterogeneous Single-Layer Graphene Oxide Reduction Kinetics. *Nano Letters* **2013,** *13* (12), 5777-5784.

90. Mathkar, A.; Tozier, D.; Cox, P.; Ong, P.; Galande, C.; Balakrishnan, K.; Leela Mohana Reddy, A.; Ajayan, P. M., Controlled, Stepwise Reduction and Band Gap Manipulation of Graphene Oxide. *The Journal of Physical Chemistry Letters* **2012,** *3* (8), 986-991.

91. Kozawa, D.; Miyauchi, Y.; Mouri, S.; Matsuda, K., Exploring the Origin of Blue and Ultraviolet Fluorescence in Graphene Oxide. *The Journal of Physical Chemistry Letters* **2013,** *4* (12), 2035-2040.

92. Chowdhury, I.; Duch, M. C.; Mansukhani, N. D.; Hersam, M. C.; Bouchard, D., Colloidal Properties and Stability of Graphene Oxide Nanomaterials in the Aquatic Environment. *Environmental Science & Technology* **2013,** *47* (12), 6288-6296.

93. Krishnamoorthy, K.; Mohan, R.; Kim, S.-J., Graphene Oxide as a Photocatalytic Material. *Applied Physics Letters* **2011,** *98* (24), 244101.

94. Hsu, H.-C.; Shown, I.; Wei, H.-Y.; Chang, Y.-C.; Du, H.-Y.; Lin, Y.-G.; Tseng, C.-A.; Wang, C.-H.; Chen, L.-C.; Lin, Y.-C.; Chen, K.-H., Graphene Oxide as a Promising Photocatalyst for CO_2 to Methanol Conversion. *Nanoscale* **2013,** *5* (1), 262-268.

95. Yeh, T.-F.; Cihlář, J.; Chang, C.-Y.; Cheng, C.; Teng, H., Roles of Graphene Oxide in Photocatalytic Water Splitting. *Materials Today* **2013,** *16* (3), 78-84.

96. Xu, S. C.; Irle, S.; Musaev, D. G.; Lin, M. C., Quantum Chemical Study of the Dissociative Adsorption of OH and H_2O on Pristine and Defective Graphite (0001) Surfaces: Reaction Mechanisms and Kinetics. *The Journal of Physical Chemistry C* **2007,** *111* (3), 1355-1365.

97. Gao, X.; Jang, J.; Nagase, S., Hydrazine and Thermal Reduction of Graphene Oxide: Reaction Mechanisms, Product Structures, and Reaction Design. *The Journal of Physical Chemistry C* **2010,** *114* (2), 832-842.

98. Pei, S.; Cheng, H.-M., The Reduction of Graphene Oxide. *Carbon* **2012,** *50* (9), 3210-3228.

99. Shang, J.; Ma, L.; Li, J.; Ai, W.; Yu, T.; Gurzadyan, G. G., The Origin of Fluorescence from Graphene Oxide. *Scientific Reports* **2012,** *2*, 792.

100. Jeon, S.-J.; Kwak, S.-Y.; Yim, D.; Ju, J.-M.; Kim, J.-H., Chemically-Modulated Photoluminescence of Graphene Oxide for Selective Detection of Neurotransmitter by "Turn-on" Response. *Journal of the American Chemical Society* **2014,** *136* (31), 10842-10845.

101. Bhattachraya, S.; Maiti, R.; Das, A. C.; Saha, S.; Mondal, S.; Ray, S. K.; Bhaktha, S. N. B.; Datta, P. K., Efficient Control of Ultrafast Optical Nonlinearity of Reduced Graphene Oxide by Infrared Reduction. *Journal of Applied Physics* **2016,** *120* (1), 013101.

102. Liaros, N.; Couris, S.; Koudoumas, E.; Loukakos, P. A., Ultrafast Processes in Graphene Oxide During Femtosecond Laser Excitation. *The Journal of Physical Chemistry C* **2016,** *120* (7), 4104-4111.

103. Zhang, Q.; Zheng, H.; Geng, Z.; Jiang, S.; Ge, J.; Fan, K.; Duan, S.; Chen, Y.; Wang, X.; Luo, Y., The Realistic Domain Structure of as-Synthesized Graphene Oxide from Ultrafast Spectroscopy. *Journal of the American Chemical Society* **2013,** *135* (33), 12468-12474.

104. Milosavljevic, B. H.; LaVerne, J. A., Pulse Radiolysis of Aqueous Thiocyanate Solution. *Journal of Physical Chemistry A* **2005,** *109* (1), 165-168.

105. Behar, D.; Bevan, P. L. T.; Scholes, G., Pulse Radiolysis of Aqueous Thiocyanate Solutions. Nature of the Intermediate Transient Species. *Journal of Physical Chemistry* **1972,** *76*, 1537-1542.

106. Xu, Y.; Sheng, K.; Li, C.; Shi, G., Self-Assembled Graphene Hydrogel via a One-Step Hydrothermal Process. *ACS Nano* **2010,** *4* (7), 4324-4330.

107. Yan, J.; Liu, J.; Fan, Z.; Wei, T.; Zhang, L., High-Performance Supercapacitor Electrodes Based on Highly Corrugated Graphene Sheets. *Carbon* **2012,** *50* (6), 2179-2188.

108. Kim, J.-E.; Oh, J.-H.; Kotal, M.; Koratkar, N.; Oh, I.-K., Self-Assembly and Morphological Control of Three-Dimensional Macroporous Architectures Built of Two-Dimensional Materials. *Nano Today* **2017,** *14*, 100-123.

109. Wu, Y.; Yang, B.; Zong, B.; Sun, H.; Shen, Z.; Feng, Y., Carbon Nanowalls and Related Materials. *Journal of Materials Chemistry* **2004,** *14* (4), 469-477.

110. Xia, X.; Zhang, Y.; Chao, D.; Guan, C.; Zhang, Y.; Li, L.; Ge, X.; Bacho, I. M.; Tu, J.; Fan, H. J., Solution Synthesis of Metal Oxides for Electrochemical Energy Storage Applications. *Nanoscale* **2014,** *6* (10), 5008-5048.

111. Choi, B. G.; Yang, M.; Hong, W. H.; Choi, J. W.; Huh, Y. S., 3d Macroporous Graphene Frameworks for Supercapacitors with High Energy and Power Densities. *ACS Nano* **2012,** *6* (5), 4020-4028.

112. Chen, Z.; Ren, W.; Gao, L.; Liu, B.; Pei, S.; Cheng, H.-M., Three-Dimensional Flexible and Conductive Interconnected Graphene Networks Grown by Chemical Vapour Deposition. *Nature Materials* **2011,** *10* (6), 424.

113. Zhou, M.; Lin, T.; Huang, F.; Zhong, Y.; Wang, Z.; Tang, Y.; Bi, H.; Wan, D.; Lin, J., Highly Conductive Porous Graphene/Ceramic Composites for Heat Transfer and Thermal Energy Storage. *Advanced Functional Materials* **2013,** *23* (18), 2263-2269.

114. Ning, G.; Fan, Z.; Wang, G.; Gao, J.; Qian, W.; Wei, F., Gram-Scale Synthesis of Nanomesh Graphene with High Surface Area and Its Application in Supercapacitor Electrodes. *Chemical Communications* **2011,** *47* (21), 5976-5978.

115. Xiao, X.; Beechem, T. E.; Brumbach, M. T.; Lambert, T. N.; Davis, D. J.; Michael, J. R.; Washburn, C. M.; Wang, J.; Brozik, S. M.; Wheeler, D. R., Lithographically Defined Three-Dimensional Graphene Structures. *ACS Nano* **2012,** *6* (4), 3573-3579.

116. Li, W.; Gao, S.; Wu, L.; Qiu, S.; Guo, Y.; Geng, X.; Chen, M.; Liao, S.; Zhu, C.; Gong, Y., High-Density Three-Dimension Graphene Macroscopic Objects for High-Capacity Removal of Heavy Metal Ions. *Scientific Reports* **2013,** *3*, 2125.

117. Tanaka, H.; Meunier, J.; Bonn, D., Nonergodic States of Charged Colloidal Suspensions: Repulsive and Attractive Glasses and Gels. *Physical Review E* **2004,** *69* (3), 031404.

118. Israelachvili, J. N., *Intermolecular and Surface Forces*. Academic press: **2011**.

119. Bai, H.; Li, C.; Wang, X.; Shi, G., A pH Sensitive Graphene Oxide Composite Hydrogel. *Chemical Communications* **2010,** *46* (14), 2376-2378.

120. Cong, H.; Ren, X.; Wang, P.; Yu, S., Macroscopic Multifunctional Graphene-Based Hydrogels and Aerogels by a Metal Ion Induced Self-Assembly Process. *ACS Nano* **2012,** 6 (3), 2693–2703.

121. Wu, Z.-S.; Yang, S.; Sun, Y.; Parvez, K.; Feng, X.; Müllen, K., 3d Nitrogen-Doped Graphene Aerogel-Supported Fe_3O_4 Nanoparticles as Efficient Electrocatalysts for the Oxygen Reduction Reaction. *Journal of the American Chemical Society* **2012,** *134* (22), 9082-9085.

122. Chang, Y.; Li, J.; Wang, B.; Luo, H.; He, H.; Song, Q.; Zhi, L., Synthesis of 3d Nitrogen-Doped Graphene/Fe 3 O 4 by a Metal Ion Induced Self-Assembly Process for High-Performance Li-Ion Batteries. *Journal of Materials Chemistry A* **2013,** *1* (46), 14658-14665.

123. Sun, S.; Wu, P., A One-Step Strategy for Thermal-and Ph-Responsive Graphene Oxide Interpenetrating Polymer Hydrogel Networks. *Journal of Materials Chemistry* **2011,** *21* (12), 4095-4097.

124. Sun, H.; Xu, Z.; Gao, C., Multifunctional, Ultra- Flyweight, Synergistically Assembled Carbon Aerogels. *Advanced Materials* **2013,** *25* (18), 2554-2560.

125. Yang, X.; Zhu, J.; Qiu, L.; Li, D., Bioinspired Effective Prevention of Restacking in Multilayered Graphene Films: Towards the Next Generation of High- Performance Supercapacitors. *Advanced Materials* **2011,** *23* (25), 2833-2838.

126. Zhang, X.; Sui, Z.; Xu, B.; Yue, S.; Luo, Y.; Zhan, W.; Liu, B., Mechanically Strong and Highly Conductive Graphene Aerogel and Its Use as Electrodes for Electrochemical Power Sources. *Journal of Materials Chemistry* **2011,** *21* (18), 6494-6497.

127. Xu, Y.; Chen, C.-Y.; Zhao, Z.; Lin, Z.; Lee, C.; Xu, X.; Wang, C.; Huang, Y.; Shakir, M. I.; Duan, X., Solution Processable Holey Graphene Oxide and Its Derived Macrostructures for High-Performance Supercapacitors. *Nano Letters* **2015,** *15* (7), 4605-4610.

128. Simon, P.; Gogotsi, Y., Capacitive Energy Storage in Nanostructured Carbon–Electrolyte Systems. *Accounts of Chemical Research* **2012,** *46* (5), 1094-1103.

129. Kim, J.; Cote, L. J.; Kim, F.; Yuan, W.; Shull, K. R.; Huang, J., Graphene Oxide Sheets at Interfaces. *Journal of the American Chemical Society* **2010,** *132* (23), 8180-8186.

130. Carlsson, J. M., Graphene: Buckle or Break. *Nature Materials* **2007,** *6* (11), 801.

131. Dan, B.; Behabtu, N.; Martinez, A.; Evans, J. S.; Kosynkin, D. V.; Tour, J. M.; Pasquali, M.; Smalyukh, I. I., Liquid Crystals of Aqueous, Giant Graphene Oxide Flakes. *Soft Matter* **2011,** *7* (23), 11154-11159.

132. Naficy, S.; Jalili, R.; Aboutalebi, S. H.; Gorkin III, R. A.; Konstantinov, K.; Innis, P. C.; Spinks, G. M.; Poulin, P.; Wallace, G. G., Graphene Oxide Dispersions: Tuning Rheology to Enable Fabrication. *Materials Horizons* **2014,** *1* (3), 326-331.

133. Aboutalebi, S. H.; Gudarzi, M. M.; Zheng, Q. B.; Kim, J. K., Spontaneous Formation of Liquid Crystals in Ultralarge Graphene Oxide Dispersions. *Advanced Functional Materials* **2011,** *21* (15), 2978-2988.

134. Jalili, R.; Aboutalebi, S. H.; Esrafilzadeh, D.; Konstantinov, K.; Razal, J. M.; Moulton, S. E.; Wallace, G. G., Formation and Processability of Liquid Crystalline Dispersions of Graphene Oxide. *Materials Horizons* **2014,** *1* (1), 87-91.

135. Yousefi, N.; Gudarzi, M. M.; Zheng, Q.; Aboutalebi, S. H.; Sharif, F.; Kim, J.-K., Self-Alignment and High Electrical Conductivity of Ultralarge Graphene Oxide–Polyurethane Nanocomposites. *Journal of Materials Chemistry* **2012,** *22* (25), 12709-12717.

136. Lin, X.; Shen, X.; Zheng, Q.; Yousefi, N.; Ye, L.; Mai, Y.-W.; Kim, J.-K., Fabrication of Highly-Aligned, Conductive, and Strong Graphene Papers Using Ultralarge Graphene Oxide Sheets. *ACS Nano* **2012,** *6* (12), 10708-10719.

137. Aboutalebi, S. H.; Chidembo, A. T.; Salari, M.; Konstantinov, K.; Wexler, D.; Liu, H. K.; Dou, S. X., Comparison of Go, Go/MWCNTs Composite and MWCNTs as Potential Electrode Materials for Supercapacitors. *Energy & Environmental Science* **2011,** *4* (5), 1855-1865.

138. https://asbury.com/resources/education/science-of-graphite/expandable-flake-graphite/.

139. Wei, T.; Fan, Z.; Luo, G.; Zheng, C.; Xie, D., A Rapid and Efficient Method to Prepare Exfoliated Graphite by Microwave Irradiation. *Carbon* **2009,** *47* (1), 337-339.

140. Pan, S.; Aksay, I. A., Factors Controlling the Size of Graphene Oxide Sheets Produced Via the Graphite Oxide Route. *ACS Nano* **2011,** *5* (5), 4073-4083.

141. Chua, C. K.; Pumera, M., Chemical Reduction of Graphene Oxide: A Synthetic Chemistry Viewpoint. *Chemical Society Reviews* **2014,** *43* (1), 291-312.

142. Portet, C.; Taberna, P.; Simon, P.; Laberty-Robert, C., Modification of Al Current Collector Surface by Sol–Gel Deposit for Carbon–Carbon Supercapacitor Applications. *Electrochimica Acta* **2004,** *49* (6), 905-912.

143. Lindström, H.; Södergren, S.; Solbrand, A.; Rensmo, H.; Hjelm, J.; Hagfeldt, A.; Lindquist, S.E., Li^+ Ion Insertion in Tio_2 (Anatase). 2. Voltammetry on Nanoporous Films. *The Journal of Physical Chemistry B* **1997,** *101* (39), 7717-7722.

144. Taberna, P.; Simon, P.; Fauvarque, J.-F., Electrochemical Characteristics and Impedance Spectroscopy Studies of Carbon-Carbon Supercapacitors. *Journal of the Electrochemical Society* **2003,** *150* (3), A292-A300.

145. Li, J.; Kim, J.-K., Percolation Threshold of Conducting Polymer Composites Containing 3d Randomly Distributed Graphite Nanoplatelets. *Composites Science and Technology* **2007,** *67* (10), 2114-2120.

146. Li, J.; Ma, P. C.; Chow, W. S.; To, C. K.; Tang, B. Z.; Kim, J. K., Correlations between Percolation Threshold, Dispersion State, and Aspect Ratio of Carbon Nanotubes. *Advanced Functional Materials* **2007,** *17* (16), 3207-3215.

147. Thommes, M.; Kaneko, K.; Neimark, A. V.; Olivier, J. P.; Rodriguez-Reinoso, F.; Rouquerol, J.; Sing, K. S., Physisorption of Gases, with Special Reference to the Evaluation of Surface Area and Pore Size Distribution (Iupac Technical Report). *Pure and Applied Chemistry* **2015,** *87* (9-10), 1051-1069.

148. Cote, L. J.; Kim, J.; Zhang, Z.; Sun, C.; Huang, J., Tunable Assembly of Graphene Oxide Surfactant Sheets: Wrinkles, Overlaps and Impacts on Thin Film Properties. *Soft Matter* **2010,** *6* (24), 6096-6101.

149. Meyer, J. C.; Geim, A. K.; Katsnelson, M. I.; Novoselov, K. S.; Booth, T. J.; Roth, S., The Structure of Suspended Graphene Sheets. *Nature* **2007,** *446* (7131), 60.

150. Shen, X.; Lin, X.; Yousefi, N.; Jia, J.; Kim, J.-K., Wrinkling in Graphene Sheets and Graphene Oxide Papers. *Carbon* **2014,** *66*, 84-92.

151. Deng, S.; Berry, V., Wrinkled, Rippled and Crumpled Graphene: An Overview of Formation Mechanism, Electronic Properties, and Applications. *Materials Today* **2016,** *19* (4), 197-212.

152. Landau, L. D., On the Theory of Phase Transitions. *Ukrainian Journal of Physics* **1937,** *11*, 19-32.

153. Peierls, R., Bemerkungen Über Umwandlungstemperaturen. *Helvetica Physica Acta* **1934,** *7* (81-83), 158.

154. Mermin, N. D.; Wagner, H., Absence of Ferromagnetism or Antiferromagnetism in One-or Two-Dimensional Isotropic Heisenberg Models. *Physical Review Letters* **1966,** *17* (22), 1133.

155. Mermin, N. D., Crystalline Order in Two Dimensions. *Physical Review* **1968,** *176* (1), 250.

156. Nelson, D.; Peliti, L., Fluctuations in Membranes with Crystalline and Hexatic Order. *Journal de Physique* **1987,** *48* (7), 1085-1092.

157. Le Doussal, P.; Radzihovsky, L., Self-Consistent Theory of Polymerized Membranes. *Physical Review Letters* **1992,** *69* (8), 1209.

158. Nelson, D. R.; Piran, T.; Weinberg, S., *Statistical Mechanics of Membranes and Surfaces*. World Scientific: 2004.

159. Novoselov, K.; Jiang, D.; Schedin, F.; Booth, T.; Khotkevich, V.; Morozov, S.; Geim, A., Two-Dimensional Atomic Crystals. *Proceedings of the National Academy of Sciences* **2005,** *102* (30), 10451-10453.

160. Novoselov, K. S.; Geim, A. K.; Morozov, S. V.; Jiang, D.; Zhang, Y.; Dubonos, S. V.; Grigorieva, I. V.; Firsov, A. A., Electric Field Effect in Atomically Thin Carbon Films. *Science* **2004,** *306* (5696), 666-669.

161. Ferrari, A. C.; Meyer, J. C.; Scardaci, V.; Casiraghi, C.; Lazzeri, M.; Mauri, F.; Piscanec, S.; Jiang, D.; Novoselov, K. S.; Roth, S.; Geim, A. K., Raman Spectrum of Graphene and Graphene Layers. *Physical Review Letters* **2006,** *97* (18), 187401.

162. Fasolino, A.; Los, J.; Katsnelson, M. I., Intrinsic Ripples in Graphene. *Nature Materials* **2007,** *6* (11), 858.

163. Seung, H.; Nelson, D. R., Defects in Flexible Membranes with Crystalline Order. *Physical Review A* **1988,** *38* (2), 1005.

164. Meng, L.; Su, Y.; Geng, D.; Yu, G.; Liu, Y.; Dou, R.-F.; Nie, J.-C.; He, L., Hierarchy of Graphene Wrinkles Induced by Thermal Strain Engineering. *Applied Physics Letters* **2013,** *103* (25), 251610.

165. Ma, X.; Zachariah, M. R.; Zangmeister, C. D., Crumpled Nanopaper from Graphene Oxide. *Nano Letters* **2011,** *12* (1), 486-489.

166. Matan, K.; Williams, R. B.; Witten, T. A.; Nagel, S. R., Crumpling a Thin Sheet. *Physical Review Letters* **2002,** *88* (7), 076101.

167. Tallinen, T.; Åström, J.; Timonen, J., The Effect of Plasticity in Crumpling of Thin Sheets. *Nature Materials* **2009,** *8* (1), 25.

168. Luo, J.; Jang, H. D.; Sun, T.; Xiao, L.; He, Z.; Katsoulidis, A. P.; Kanatzidis, M. G.; Gibson, J. M.; Huang, J., Compression and Aggregation-Resistant Particles of Crumpled Soft Sheets. *ACS Nano* **2011,** *5* (11), 8943-8949.

169. Stauffer, D.; Aharony, A., *Introduction to Percolation Theory*. Taylor & Francis: **2014**.

170. Chen, S.; Duan, J.; Jaroniec, M.; Qiao, S. Z., Hierarchically Porous Graphene-Based Hybrid Electrodes with Excellent Electrochemical Performance. *Journal of Materials Chemistry A* **2013,** *1* (33), 9409.

171. Zhao, X.; Zhang, L.; Murali, S.; Stoller, M. D.; Zhang, Q.; Zhu, Y.; Ruoff, R. S., Incorporation of Manganese Dioxide within Ultraporous Activated Graphene for High-Performance Electrochemical Capacitors. *ACS Nano* **2012,** *6* (6), 5404-5412.

172. Morozov, S. V.; Novoselov, K. S.; Katsnelson, M. I.; Schedin, F.; Elias, D. C.; Jaszczak, J. A.; Geim, A. K., Giant Intrinsic Carrier Mobilities in Graphene and Its Bilayer. *Physical Review Letters* **2008,** *100* (1), 016602.

173. Chen, J.; Han, Y.; Kong, X.; Deng, X.; Park, H. J.; Guo, Y.; Jin, S.; Qi, Z.; Lee, Z.; Qiao, Z.; Ruoff, R. S.; Ji, H., The Origin of Improved Electrical Double-Layer Capacitance by Inclusion of Topological Defects and Dopants in Graphene for Supercapacitors. *Angewandte Chemie International Edition* **2016,** *55* (44), 13822-13827.

174. Ji, H.; Zhao, X.; Qiao, Z.; Jung, J.; Zhu, Y.; Lu, Y.; Zhang, L. L.; MacDonald, A. H.; Ruoff, R. S., Capacitance of Carbon-Based Electrical Double-Layer Capacitors. *Nature Communications* **2014,** *5*, 3317.

175. Szabó, T.; Berkesi, O.; Forgó, P.; Josepovits, K.; Sanakis, Y.; Petridis, D.; Dékány, I., Evolution of Surface Functional Groups in a Series of Progressively Oxidized Graphite Oxides. *Chemistry of Materials* **2006,** *18* (11), 2740-2749.

176. Glaze, W. H.; Kang, J.-W.; Chapin, D. H., The Chemistry of Water Treatment Processes Involving Ozone, Hydrogen Peroxide and Ultraviolet Radiation. **1987**.

177. Eskicioglu, C.; Prorot, A.; Marin, J.; Droste, R. L.; Kennedy, K. J., Synergetic Pretreatment of Sewage Sludge by Microwave Irradiation in Presence of H_2O_2 for Enhanced Anaerobic Digestion. *Water Research* **2008,** *42* (18), 4674-4682.

178. Parsons, S., *Advanced Oxidation Processes for Water and Wastewater Treatment*. IWA Publishing: **2004**.

179. Wong, W. T.; Chan, W. I.; Liao, P. H.; Lo, K. V., A Hydrogen Peroxide/Microwave Advanced Oxidation Process for Sewage Sludge Treatment. *Journal of Environmental Science and Health Part A* **2006,** *41* (11), 2623-2633.

180. Wang, Y.; Wei, Y.; Liu, J., Effect of H 2 O 2 Dosing Strategy on Sludge Pretreatment by Microwave- H_2O_2 Advanced Oxidation Process. *Journal of Hazardous Materials* **2009,** *169* (1), 680-684.

181. Ishibashi, K.-I.; Fujishima, A.; Watanabe, T.; Hashimoto, K., Detection of Active Oxidative Species in TiO_2 Photocatalysis Using the Fluorescence Technique. *Electrochemistry Communications* **2000,** *2* (3), 207-210.

182. Ishibashi, K.-i.; Fujishima, A.; Watanabe, T.; Hashimoto, K., Quantum Yields of Active Oxidative Species Formed on TiO_2 Photocatalyst. *Journal of Photochemistry and Photobiology A: Chemistry* **2000,** *134* (1), 139-142.

183. Hirakawa, T.; Nosaka, Y., Properties of O_2 and OH Formed in TiO_2 Aqueous Suspensions by Photocatalytic Reaction and the Influence of H_2O_2 and Some Ions. *Langmuir* **2002,** *18* (8), 3247-3254.

184. Saito, R.; Hofmann, M.; Dresselhaus, G.; Jorio, A.; Dresselhaus, M., Raman Spectroscopy of Graphene and Carbon Nanotubes. *Advances in Physics* **2011,** *60* (3), 413-550.

185. Graves, P.; Gardiner, D., Practical Raman Spectroscopy. *Springer* **1989**.

186. Wu, J.-B.; Lin, M.-L.; Cong, X.; Liu, H.-N.; Tan, P.-H., Raman Spectroscopy of Graphene-Based Materials and Its Applications in Related Devices. *Chemical Society Reviews* **2018,** *47* (5), 1822-1873.

187. Lucchese, M. M.; Stavale, F.; Ferreira, E. M.; Vilani, C.; Moutinho, M.; Capaz, R. B.; Achete, C.; Jorio, A., Quantifying Ion-Induced Defects and Raman Relaxation Length in Graphene. *Carbon* **2010,** *48* (5), 1592-1597.

188. Childres, I.; Jauregui, L. A.; Park, W.; Cao, H.; Chen, Y. P., Raman Spectroscopy of Graphene and Related Materials. *New Developments in Photon and Materials Research* **2013,** *1*.

189. Ferrari, A. C.; Basko, D. M., Raman Spectroscopy as a Versatile Tool for Studying the Properties of Graphene. *Nature Nanotechnology* **2013,** *8* (4), 235.

190. Kudin, K. N.; Ozbas, B.; Schniepp, H. C.; Prud'Homme, R. K.; Aksay, I. A.; Car, R., Raman Spectra of Graphite Oxide and Functionalized Graphene Sheets. *Nano Letters* **2008,** *8* (1), 36-41.

191. Stankovich, S.; Piner, R. D.; Nguyen, S. T.; Ruoff, R. S., Synthesis and Exfoliation of Isocyanate-Treated Graphene Oxide Nanoplatelets. *Carbon* **2006,** *44* (15), 3342-3347.

192. Zhang, J.; Yang, H.; Shen, G.; Cheng, P.; Zhang, J.; Guo, S., Reduction of Graphene Oxide via L-Ascorbic Acid. *Chemical Communications* **2010,** *46* (7), 1112-1114.

193. Kotchey, G. P.; Allen, B. L.; Vedala, H.; Yanamala, N.; Kapralov, A. A.; Tyurina, Y. Y.; Klein-Seetharaman, J.; Kagan, V. E.; Star, A., The Enzymatic Oxidation of Graphene Oxide. *ACS Nano* **2011,** *5* (3), 2098-2108.

194. Shin, H. J.; Kim, K. K.; Benayad, A.; Yoon, S. M.; Park, H. K.; Jung, I. S.; Jin, M. H.; Jeong, H. K.; Kim, J. M.; Choi, J. Y., Efficient Reduction of Graphite Oxide by Sodium Borohydride and Its Effect on Electrical Conductance. *Advanced Functional Materials* **2009,** *19* (12), 1987-1992.

195. Rao, C. e. N. e. R.; Sood, A. e. K.; Subrahmanyam, K. e. S.; Govindaraj, A., Graphene: The New Two- Dimensional Nanomaterial. *Angewandte Chemie International Edition* **2009,** *48* (42), 7752-7777.

196. Luo, D.; Zhang, G.; Liu, J.; Sun, X., Evaluation Criteria for Reduced Graphene Oxide. *The Journal of Physical Chemistry C* **2011,** *115* (23), 11327-11335.

197. Yang, D.; Velamakanni, A.; Bozoklu, G.; Park, S.; Stoller, M.; Piner, R. D.; Stankovich, S.; Jung, I.; Field, D. A.; Ventrice Jr, C. A., Chemical Analysis of Graphene Oxide Films after Heat and Chemical Treatments by X-Ray Photoelectron and Micro-Raman Spectroscopy. *Carbon* **2009,** *47* (1), 145-152.

198. Subrahmanyam, K.; Vivekchand, S.; Govindaraj, A.; Rao, C., A Study of Graphenes Prepared by Different Methods: Characterization, Properties and Solubilization. *Journal of Materials Chemistry* **2008,** *18* (13), 1517-1523.

199. Kumar, P. V.; Bernardi, M.; Grossman, J. C., The Impact of Functionalization on the Stability, Work Function, and Photoluminescence of Reduced Graphene Oxide. *ACS Nano* **2013,** *7* (2), 1638-1645.